

AIRGAP-LESS ELECTRIC MOTOR

by

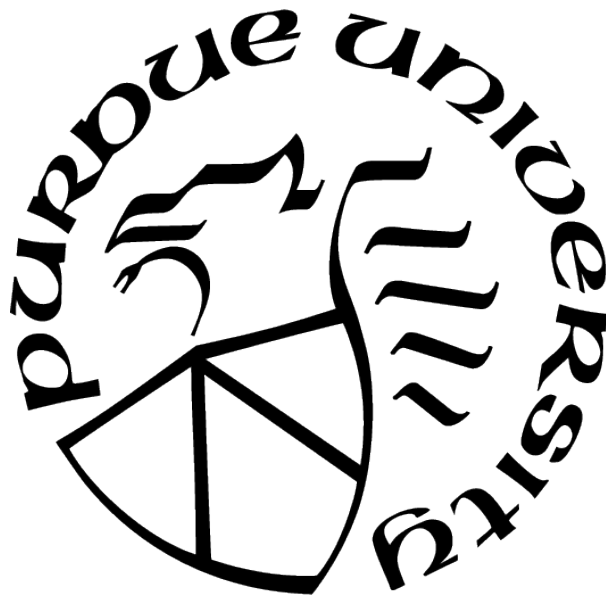
Maryam Alibeik

A Dissertation

Submitted to the Faculty of Purdue University

In Partial Fulfillment of the Requirements for the degree of

Doctor of Philosophy



School of Electrical and Computer Engineering

Indianapolis, Indiana

August 2021

**THE PURDUE UNIVERSITY GRADUATE SCHOOL
STATEMENT OF COMMITTEE APPROVAL**

Dr. Euzeli dos Santos, Chair

Department of Electrical and Computer Engineering

Dr. Brian King

Department of Electrical and Computer Engineering

Dr. Linxi Li

Department of Electrical and Computer Engineering

Dr. Steven Rovnyak

Department of Electrical and Computer Engineering

Approved by:

Dr. Brian King

To the best father that anyone could ask for.
I wish you were here to see your dream come true.

ACKNOWLEDGMENTS

First, I have to say that I am grateful for having the opportunity to continue my education to this point. I want to say thank you to the best parents anyone could have asked for who were always behind my back and supported me. I want to specially thank my biggest motivator, my dad who always encouraged me to continue studying and become a strong independent woman. I hope I was able to achieve this goal and made him proud even that he is not with us anymore. I want to express my gratitude to my sister, Nazanin and my brother, Alireza who are my second parents. They never let me feel alone after my parents left us. I know that I always can rely on them and they have my back. They supported me through my education and specially my PhD. They never let me decide emotionally to go back to Iran and take care of my dad. They both sacrificed so many activities and times that they could spend with their families just to make me certain that I should never quit my education to help them with my dad. They did everything in their power to just make me smile and be happy and only move towards my goal without any distraction. My sister, who is no less than a mother to me, was and is always there for me through everything, bad and good. My brother who always, no matter what the situation is, makes me laugh and supports me in every step of my life. I hope that I am making them proud with my achievements to show them how grateful I am for what they did. I have to thank my caring, and loving partner Sepehr who has always had my back since the day that I met him. He supported me through my Master's and now I am finalizing my PhD. He spent so many hours and days to just make sure that I am doing everything in my power. He always encourage me and motivates me to do more than what is needed. He always encouraged me to put all my power in and move toward my goals. There were times that regardless of his busy schedule, he spent several hours just to talk to me and make sure than I am doing my best and am not satisfied with the minimum and always continue as far as I can. His guidance is always appreciated and I am so grateful to have him in my life. I can not thank my supervisor, Dr. Santos enough for what he has done for me. He gave me so many opportunities since the day that I started working with him (July 2012). I can say I grew so much and became way stronger by having these opportunities. I want to thank him for all the challenges that he

gave me and taught me to be comfortable being uncomfortable. The deadlines that he gave me were always yesterday and he encouraged me not to waste any time and try to achieve as much as I can. I learned a lot from him on how to be successful and how to go towards my goals. I am and will be always grateful for everything he has done for me. It is an honor to say that I have worked in his lab and under his supervision for 9 years. I want to express my greatest gratitude to the ECE department who are my second family and never let me feel as I am away from my family. Dr. King who always guided me through all aspects of my education. Despite his busy schedule, he always made time for me if I needed any advice or had any questions. He was always patient with me even if I was overwhelmed. He did the biggest favor for me and gave me the opportunity to teach several undergraduate ECE courses during my PhD. I am so grateful for these opportunities, which led to a job offer in a public university. It was also a big honor to co teach two classes with Dr. King and be his Teaching Assistant. I learned a lot from him and will always be grateful. Also, Dr. King always did this favor for me and made sure that I have funding during my PhD and I am always grateful. It is an honor that I have Dr. King as one of my committee members. I want to thank someone who was the biggest support since I started my bachelors at IUPUI. Mrs. Sherrie Tucker, who I cannot say and count how much she supported me during my education. Sherrie was always there for me even if she was not in school. I always had this peace of mind that Sherrie is here so I do not have to worry. Her mental support was priceless and I am so grateful to have her in my life. She always made sure that everything is in the right path. Honestly, during my 12 years at IUPUI I never missed a deadline and that was all because of her. I bothered her so much and always went to her when I doubt something or wanted to double check and confirm. I have to say sorry to her for so many times that I forgot to clock out during my hourly jobs and she had to correct them. Sherrie always did everything that she could to make sure that I am OK in all aspects of my life. I also want to thank my committee members, Dr. Lingxi Li and Dr. Rovnyak for their great support. I want to also thank Dr. Maher Rizkalla for always being there and guided me since I started my Bachelor's at IUPUI. Jane and Jeff are two of my favorites in ECE department who always did all in their power to help you. Last but not least I want to thank my lab mates, Omar Nezamuddin, and Rishikesh Bagwe. Omar has been my lab mate since 2014.

We had worked on some projects together which was a pleasure for me. Honestly, I learned a lot from Omar and Rishikesh and had a great journey in the power electronics lab. They always made sure that the lab environment is friendly and warm which helped me to never get tired of being in school and I can say that I enjoyed all the times that I spent in the lab with them and enjoyed working with them. There were also times that I was sad, worried, or stressed about work and they were always there to support. I am always grateful. I also want to thank all my friends and family who always supported me.

PREFACE

This dissertation is based on proposing a new electric machine in which the airgap reaches the minimum value possible in order to maximize the electromagnetic torque, which is called airgap-less electric motor. This machine which is already developed in the laboratory has a torque density (torque per motor volume) which is comparable to hydraulic motors. It is worth mentioning that the efficiency of this motor will have higher efficiency than hydraulic machines due to a large number of energy conversion stages.

This dissertation is ultimately based on a journal paper, and two published conference papers for the author Maryam Alibeik.

TABLE OF CONTENTS

LIST OF TABLES	10
LIST OF FIGURES	11
ABBREVIATIONS	15
ABSTRACT	16
1 INTRODUCTION	17
1.1 Machines with Constant Airgap	21
1.1.1 Induction Machines	22
1.1.2 Synchronous Machines	24
1.2 Machines with Variable Airgap	26
1.2.1 Synchronous Machines	27
1.2.2 Permanent Magnet Machines	28
1.2.3 Interior Permanent Magnet Synchronous Machines	29
1.2.4 Synchronous Reluctance Machine	29
1.2.5 Permanent Magnet Flux Switching Machines	30
1.2.6 Permanent Magnet Vernier Machines	31
1.3 Machines with Eccentric Airgap	32
1.4 Scientific Outcomes	33
2 AIRGAP-LESS ELECTRIC MACHINE WITH AN INTERNAL ROTOR	36
2.1 Machine With Three Poles and Three Phases	37
2.1.1 Machine Modeling	41
2.1.2 Experimental Setup	46
2.2 Airgap-less Electric Machine with Six Bipoles and Six Phases	50
2.2.1 Machine Modeling	52
2.2.2 Magnetic Circuit	54
2.2.3 Inductance, Energy and Torque	55
2.2.4 Mechanical Position and Speed	58
2.2.5 Simulation and Experimental Results	60
3 AIRGAP-LESS ELECTRIC MACHINE WITH AN EXTERNAL ROTOR	63

3.1	Airgap-less Machine Operating Principle	63
3.2	Three Bipole Machine	64
3.2.1	Conception and Operation	64
3.2.2	Airgap Modeling	66
3.2.3	Magnetic Circuit	70
3.2.4	Inductances, Energy, and Torque	71
3.2.5	Mechanical Analysis	77
	Position and Speed	77
	Static Force Vector Analysis	79
	Tribology Phenomena	80
	Wear Rate Proportional Factor	81
3.3	Four Bipole Machine and Generalization	82
3.4	Finite-Element Analysis	84
3.5	Simulation and Experimental Results	86
3.6	Comparison and Conclusion	93
4	MODELING AND SIMULATION OF AN AIRGAP-LESS ELECTRIC MACHINE IN C++ USING RUNGE KUTTA INTEGRATION METHOD	97
4.1	Inductance, Energy, and Torque Modeling using Runge-Kutta Integration Method	97
4.2	Mechanical Analysis	100
4.3	Simulation and Experimental Results	102
5	SUMMARY AND FUTURE WORKS	108
	REFERENCES	110
	VITA	119

LIST OF TABLES

2.1	Parameters used in the simulation	61
3.1	Lubrication types with respect to lambda ratio	80
3.2	Parameters used in the simulation	91
4.1	Parameters used in the simulation	103

LIST OF FIGURES

1.1	Flowchart showing the electric machines classifications	20
1.2	Machine with constant airgap.	22
1.3	(a) Squirrel cage induction machine, and (b) wound rotor induction machine. . .	23
1.4	Magnetically Geared Induction Machine	24
1.5	Synchronous Machine with Constant Airgap	25
1.6	(a) switched reluctance machine with variable gap, (b) variable gap vs. position.	26
1.7	Synchronous Machine with Variable Airgap	27
1.8	Triple PM excited Magnetic Gear	28
1.9	Flux switching permanent magnet	30
1.10	Permanent Magnet Vernier Machine	31
1.11	(a) switched reluctance machine with a rolling rotor, and (b) eccentric gap vs. position	33
1.12	Electric machine Diagram	34
2.1	C-core magnetic device (relay).	37
2.2	3D views of the proposed concept.	38
2.3	(a) Location where the winding is placed for MMF creation. (b) Profile of stator current for continuous generation. (c) Sequence of shots showing a continuous rotor movement..	39
2.4	Hydraulic machine.	40
2.5	(a) Combined rotor translational and rotational movements. (b) Gear box. . . .	41
2.6	Geometry approach used for air gap derivation.	42
2.7	Magnetic equivalent circuit of the machine shown in Fig. 2.2 when only one pole is supplied with current.	43
2.8	Developed diagram of the proposed electric machine.	44
2.9	Photos of the proposed electric machine with its drive system.	47
2.10	Machine drive system.	48
2.11	Experimental results: currents in poles 1 and 2.	48
2.12	3D views of the proposed 3 bipole machine.	50
2.13	(a) Bipole configuration. (b) machine drive system.	51
2.14	Sequence of shots showing a continuous rotor movement.	51

2.15	Geometric approach used for airgap derivation.	52
2.16	Points of interest for airgap derivation.	53
2.17	(a) Equivalent circuit of the magnetic device. (b) Equivalent circuit used for mesh analysis.	54
2.18	Equivalent circuits used to calculate self-inductance	56
2.19	Equivalent circuits used to calculate mutual-inductance	57
2.20	Voltage applied to the machine poles: (a) no overlap among poles, and (b) overlap among poles.	58
2.21	(a) Initial position of the rotor. (b) Position of the rotor after δ electrical degrees from stator point of view.	59
2.22	(a) Position of the rotor after an electrical cycle. (b) Geometrical approach to find angle δ	59
2.23	Simulation results (3 pole machine): (a) voltage, (b) current, and (c) torque.	61
2.24	Six pole machine: (a) stator and (b) rotor.	62
2.25	(a) Experimental setup. (b) Phase voltage of a single bipole (green), current of the same phase voltage (purple), and an adjacent current (red).	62
3.1	Three-dimensional views of the proposed three-bipole machine. (a) Stator, (b) rotor, (c) stator–rotor in perspective, and (d) stator–rotor top view.	65
3.2	(a) Bipole configuration. (b) machine drive system.	66
3.3	Sequence of shots showing a continuous rotor movement.	67
3.4	Hydraulic machine.	67
3.5	Geometric approach used for airgap derivation.	68
3.6	Points of interest for airgap derivation.	69
3.7	(a) Equivalent circuit of the magnetic device. (b) Equivalent circuit used for mesh analysis.	72
3.8	Equivalent circuits used to calculate self-inductance.	73
3.9	Equivalent circuits used to calculate mutual-inductance.	75
3.10	Voltage applied to the machine poles: (a) no overlap among poles, and (b) overlap among poles.	76
3.11	(a) Initial position of the rotor. (b) Position of the rotor after δ electrical degrees from stator point of view.	78
3.12	Static force vector analysis.	79
3.13	Asperities of two surfaces in contact.	80

3.14	3D views of the proposed 4 bipole machine. (a) stator-rotor in perspective, and (b) stator-rotor top-view.	83
3.15	(a) Four key points for saturation analysis. (b) Flux density versus rotor angle for the key points.	85
3.16	(a) Simulation results (3 bipole machine): (a) voltage, (b) current, (c) torque.	86
3.17	Simulation results (4 bipole machine): (a) voltage, (b) current, (c) torque.	87
3.18	Simulation results (9 bipole machine): (a) voltage, (b) current, and (c) torque.	88
3.19	Nine bipole machine: (a) rotor and (b) stator.	89
3.20	(a) experimental setup, (b) torque measurement setup.	89
3.21	Signals showing change of: (a) input voltage (top waveform) and DC link current (bottom waveform), (b) direction, and (c) frequency.	90
3.22	Torque vs. power for different operating frequencies: (a) 5 Hz and (b) 10 Hz.	92
3.23	Vibration signals for: (a) airgap-less machine and (b) induction machine.	93
3.24	Fast Fourier Transform of airgap-less machine operating at 10 Hz.	93
3.25	Mechanical speed versus electrical frequency: (top) simulation, and (bottom) experimental results.	94
3.26	(a) Torque density comparison. (b) Structure of the compared machines.	95
3.27	Torque Density Comparison Chart for Electric machines with PM	96
3.28	Torque Density Comparison Chart for Electric machines without PM	96
4.1	Differential equations for calculating the currents in each phase.	99
4.2	Calculation of RK coefficients for the current in phase 1.	100
4.3	(a) Initial position of the rotor. (b) Position of the rotor after θ_e electrical degrees from stator point of view.	101
4.4	Calculation mechanical speed using RK integration method.	102
4.5	Calculation of the position of the rotor using RK integration method.	103
4.6	Simulation results (9 bipole machine): (a) voltage, (b) current, (c) torque.	104
4.7	Simulation results (9 bipole machine): (a) mechanical speed using T_e and (b) mechanical speed using ω_e	105
4.8	Comparison between theoretical and experimental mechanical frequency.	106
4.9	Comparison between mechanical speeds obtained using Euler and Runge-kutta integration method.	106
4.10	Nine bipole machine: (a) rotor and (b) stator.	107

5.1 (a) torque density comparison. (b) structure of the compared motors (in scale). 108

ABBREVIATIONS

HEV	Hybrid Electric Vehicle
PM	Permanent Magnet
PMSM	Permanent Magnet Synchronous Machine
IPMSM	Interior Permanent Magnet Synchronous Machine
SRM	Synchronous Reluctance Machine
FSPM	Flux Switching Permanent Magnet Machine
MEPT	Maximum Efficiency Point Tracker
AUV	Autonomous Underwater Vehicles

ABSTRACT

This dissertation focuses mainly on the airgap-less electric machine. An extensive literature review has been presented along with a systematic study that included analytical modeling, simulation with both steady-state and transient analysis, prototype building, and experimental validation. In this type of device, the rotor is allowed to touch the stator at a contact point, which maximizes the internal flux and therefore the electromagnetic torque. A higher torque density motor is proposed in this dissertation due to a reduced reluctance caused by zero airgap situation. A comparison with other high torque density electric machines demonstrates the advantages of the proposed machine. Switched reluctance motor for hybrid vehicle, integrated magnetic gear, induction machines, are some examples of the machines with lower torque density than the airgap-less electric machine. This machine will maximize the generated torque allowing these type of machines to be competitive in applications where hydraulic motors are prevalent, i.e., low-speed and high-torque requirements. Hydraulic motor systems face two major problems with their braking system and with low efficiency due to a large number of energy conversion stages (i.e., motor-pump, hydraulic connections and the hydraulic motor itself). The proposed electric motor, unlike hydraulic motors, converts electrical energy directly to mechanical energy with no extra braking system necessary and with higher efficiency. The evolution of the airgap-less electric machine from three poles to 9 bi-poles is discussed in this dissertation. The modeling of this machine with a minimum number of poles is discussed before a generalization is presented. The simulation and analysis of the airgap-less electric motor has been done using Euler integration method as well as Runge Kutta 4th order integration method due to its higher precision. A proof-of-concept electric machine with nine magnetic bipoles is built to validate the theoretical assumptions.

1. INTRODUCTION

Now a days climate change and its impacts on earth has been one of the main issues that concerns every human being [1]. Infrastructures, such as buildings and industrial facilities have been affected by the climate change [2]–[8]. It is also believed that the big percentage of increased temperature is due to the greenhouse gas concentration [9]. Based on an article from NASA, CO_2 is one of the most important greenhouse gases, which can be released through the human activities such as burning fossil fuels [10]. Scientists have been trying for a long time to reduce the radiation of CO_2 worldwide[9]. The energy consumption is one of the main factors that results into the emission of CO_2 . Recognizing the biggest consumers of energy can help optimizing the energy consumption. In [11], it has been stated that electric machines consume 70% of electrical energy globally. For example, induction machines are consuming the major part of the energy worldwide [12]. One option for optimizing the consumption of energy through electric machines is to increase the electric machine's efficiency [1].

There has been a survey done in [13] which has focused mainly on the efficiency improvements of induction machines. Thermal management is one of the typical methods used for increasing the efficiency of electrical machines. A predictive thermal management system is presented in [14] for electric machines in more electric aircrafts. In this method, the system monitors the efficiency at real-time temperature and adjust the cooling according to this efficiency. This study claims that this method help the system to maintain its high efficiency status. This method has been implemented using a PMSM machine and the results show that the power consumption of the cooling system reduced by 30% and the total system's loss reduced by 9%. The [15] also focuses on the efficiency of the propulsion motor for aircraft. In this study, a new iron less stator axial flux permanent magnet machine is proposed which uses oil immersed forced cooling system, which has a high power density and efficiency and a good candidate for use in aircraft. The prototype of this unit was developed and tested. The results showed that the efficiency could reach 97.4% when the current density is about $10A/mm^2$. Other articles present different methods for increasing the efficiency of electric machines and reducing their losses consequently. In [12], it has been shown the result of

reducing temperature on increasing the efficiency by forced cooling of the coils of an induction machine. This study claims that reducing the coil temperature by $10^{\circ}C$ has an effect of 0.5% efficiency increase. In the same article, it has also been shown that the internal cooling has more effect on the efficiency than the external cooling. The use of unidirectional fan, reformation of fan blade and fan cover shape, and water or oil cooling are some examples of the cooling methods used in this paper.

In [16], a maximum efficiency point tracker (MEPT) has been proposed to improve the efficiency of an electric propeller for autonomous underwater vehicles (AUVs). The analysis of this method has shown that the electric propeller was able to maintain the efficiency regardless of the variable water flow. Reducing the power consumption in electric appliances and electric vehicles will save the energy significantly. For example in machines, which operate in variable speed, reducing the power consumption is very important. In [17], a pole changing permanent magnet (PM) machine has been proposed which will change the number of poles whenever the speed changes. It is worth mentioning that in this machine, the winding connections will not change when the number of poles are changing and this contributes in improving the efficiency. Based on the analysis in this study the induced voltage changed from 79% to 100% while the iron losses reduced by 36% compare to the conventional PM machine. In [18] a switched flux PM memory machine has been proposed which contains a stator with changeable magnetized permanent magnets. The idea of this proposal is to improve the efficiency by weakening the PM flux linkage at high speed. In this situation, the iron loss will be reduced and the flux density in the lamination will decrease. The flux weakening has also been studied [19] in which it shows that by using the field excitation regulating without flux weakening the maximum power at high speed will not be constant. However the constant maximum power at high speed can be obtained by employing the flux weakening armature current control. There are studies in the literature such as [20] in which the efficiency of an induction machine is compared to the efficiency of synchronous reluctance machine. In this paper it has been shown that the performance of both machines are similar and therefore the cheaper machine, i.e. SRM is a better option. In addition, it has been shown that since the dominant power losses is the copper loss in these machines, the overall efficiency depends on the speed in which these machines are operated. Another

way to increase the efficiency of electric machines is using better magnetic materials. As [21] states, conventional soft laminations can be replaced by new materials such as high silicon non-oriented steel and partially cubic textured steel can increase the efficiency by 1.5 – 3%. Magnetic materials such as NdFeB, which is a part of the rare earth magnets, allow a very strong magnetic field in a very small volume [22] and a high level of performance. Nevertheless these magnets have two main disadvantages that are being expensive and the extraction and refinement of rare earth oxides is a potentially environmentally damaging process such as poisoning the farms and villages. According to [22] the effect of rare earth magnets can be reduced by either reducing the amount of rare earth magnet used in the electric machine, or by substituting them completely. There have been other researches done on the topic of rare earth magnet free machines [23]–[25]. Another example which presents a material simulation model for improving the accuracy of machine design is [26]. In this study, the impact of magnetic materials under various dependencies such as mechanical stress, and cut edge effect on electrical machines is presented. These impacts have been shown by Finite Element simulation. The concept of energy efficiency has been studied in the literature for hybrid electric vehicles (HEV) [27]–[31]. For example in [32], a multi-island generic algorithm has been used for returning and characterizing the optimal design for PMSM for a defined driving cycle. There has been a new approach proposed by [33] in which the efficiency of the permanent magnet hybrid brushless machine has been optimized by tuning the DC field current only. This paper presents that the machine achieves the lowest input power regardless of the amount of load and speed, [34] proposed a mathematical method to compute the field in an electric machine which is generated by fully magnetized superconductors. Superconductors and the use of them in electric machines will increase the power density and the efficiency of the machine. While this paper analyzed the magnetic field using three different methods of Biot-Savart (BS), Fourier Transform Method (FT), and Fast Fourier Transform Method (FFT), it concluded that using the FFT method will give a fast and accurate result than other two methods. Electric machines can be categorized based on their torque and torque density (torque per machine volume). Achieving high-torque density has always been one of the targets while designing electric machines [35]–[40], which has inspired new designs as presented in the technical literature [41]. One of

the most important applications for high torque electric machines is the use of high torque density electric machines in an electric vehicle. In other applications such as industrial and commercial applications, hydraulic machines are selected over electrical machines due to their compact size [42], [43]. For example, although the high torque generated by vernier permanent magnet machines and machines with partitioned rotor are one of the highest among electric machines, they still do not generate torque density that is comparable to hydraulic machines. Other examples of non-conventional designs of electric machines and control strategies proposed by industry and academia include: 1) a dual rotor structure along with a dual excitation [44], 2) an outer rotor hybrid excitation [45], 3) new control strategies proposed in order to enhance the mechanical torque [46], and 4) injection of third harmonic current [47].

This introduction presented a unique classification of electric machines considering their gap characteristics as well as a discussion on high torque electric machines. The existence of the gap in electric machines is unavoidable. Gap is the physical space consisting of air or fluids (such as oils or ferrofluids) which will separate the rotor and the stator of an electric machine. This physical space will allow the rotor to move freely inside or outside of the stator. Although the presence of a gap is fundamental in creating the rotational movements, designers often try to minimize this space to maximize the internal flux and consequently the electromagnetic torque. Fig. 1.1 shows the classification of electric machines based on their gap structure.

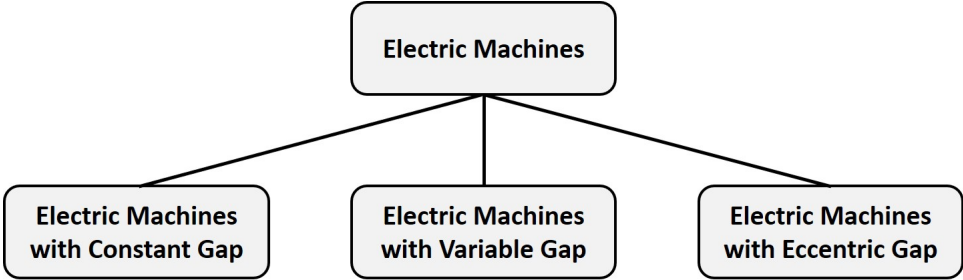


Figure 1.1. Flowchart showing the electric machines classifications

The gap plays an important role in defining other parameters of electric machines. For example, the reluctance of the gap in an electric machine is proportional to the length of the

gap which is shown in (1.1). On the other hand, the flux of an electric machine is inversely proportional to the reluctance as shown in (1.2), therefore less reluctance will result into more flux.

$$\mathcal{R} = \frac{g}{\mu_0 A} \quad (1.1)$$

$$\phi = \frac{Ni}{\mathcal{R}} \quad (1.2)$$

Although the least amount of gap is always desirable, in theory it will result into a very large flux, but the length of the gap will never reach zero due to the roughness of the material, as well as the flux will be limited by the saturation of the magnetic material. Reducing the gap has some negative effects such as cost, tight tolerances associated with reliability, heat and dynamic performance which requires enough clearances.

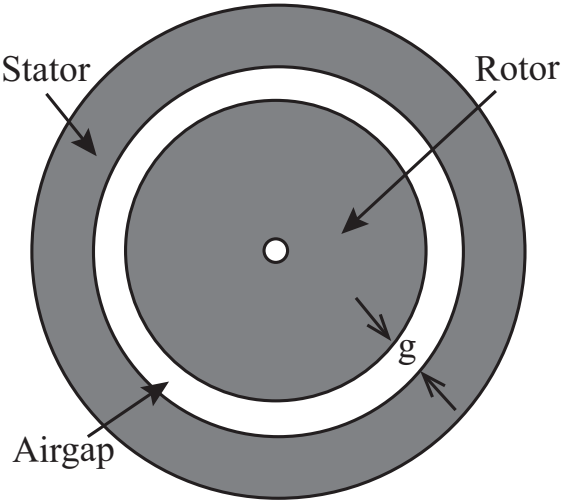
The gap space between stator and rotor can also be filled with ferrofluids instead of air [48] as the air may cause some limitations in the performance due to the very low permeability. Ferrofluids are liquids made of nano-scale ferromagnetic or ferrimagnetic material. These material have high permeability and consequently will improve the magnetic performance of the machine.

Here I will present the electric machines' classifications according to the structure of their airgap, i.e. 1) constant airgap, 2) variable airgap, and 3) eccentric airgap. In electric machines, the physical geometry of the rotor and stator defines the characteristics of the airgap. In a typical electric machine, the rotor with either constant or variable airgap will only have the rotational movement. While in machines with eccentric gap, the rotor will have both rotational and translational movements. Both typical and eccentric gap machines will be presented in this introduction.

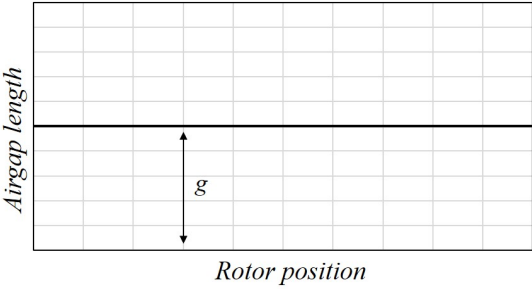
1.1 Machines with Constant Airgap

Machines with constant airgap will have the same airgap length during one complete cycle of the rotor either inside or outside of the stator. Fig. 1.2(a) shows an electric machine

along with its airgap variation as a function of the position of the rotor, as shown in Fig. 1.2(b). Now I will review some popular electric machines with constant airgap.



(a) An induction machine with a constant airgap.



(b) constant gap vs. position.

Figure 1.2. Machine with constant airgap.

1.1.1 Induction Machines

Fig. 1.3(a) shows an induction machine with a squirrel cage rotor where the voltage is induced in the rotor windings that will produce the rotor current and magnetic field. Another type of induction machines is the wound rotor induction machine where the rotor has a three phase winding inside as shown in Fig. 1.3(b). Both machines in Fig. 1.3 are identical in terms of electrical characteristics. However, wound rotor induction machines are in disuse due to maintenance issues.

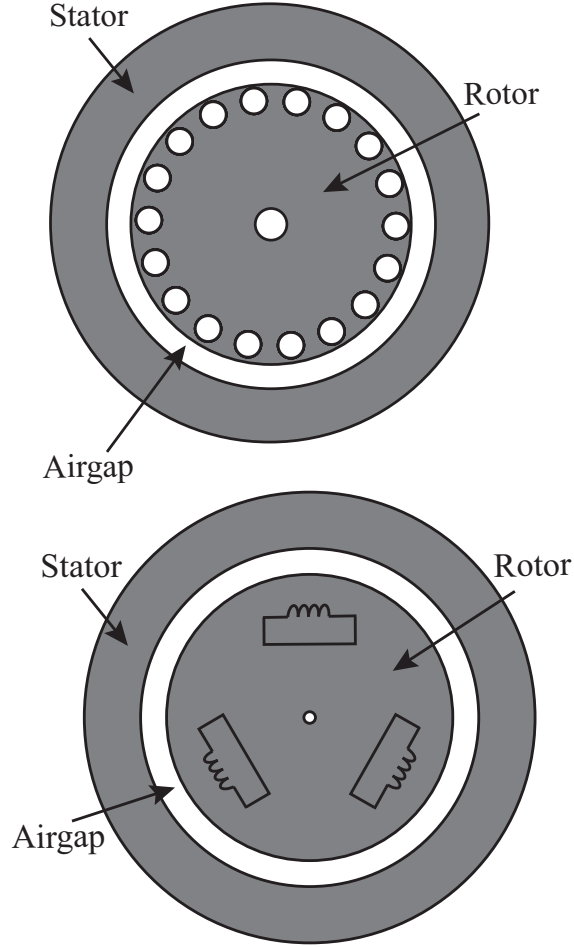


Figure 1.3. (a) Squirrel cage induction machine, and (b) wound rotor induction machine.

The torque in induction machines can be calculated using (1.3). Equation (1.3) is derived assuming there is no saturation and using the reference frame theory.

$$T_e = X_M(i_{qs}i_{dr} - i_{ds}i_{qr}) \quad (1.3)$$

An induction machine with an integrated magnetic gear is also an example of a machine with constant airgap [49]. Magnetic gears will transmit torque with no contact at all. Magnetic gearing effect is used in [50] to propose a magnetically geared induction machine. This machine is as shown in Fig. 1.4.

This machine consists of four different armatures from which two are stationary and two are rotating. The innermost armature is the stator of the induction machine. This stator

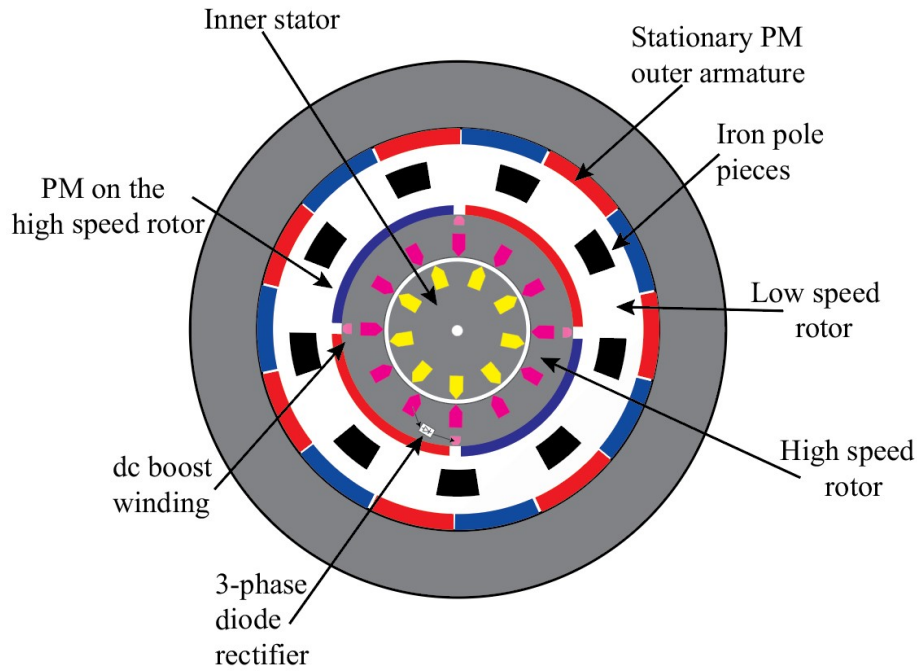


Figure 1.4. Magnetically Geared Induction Machine

will be excited by a balanced three-phase voltage which will result in creating the magnetic field. This magnetic field will produce an electromagnetic torque in the high speed rotor. High speed rotor consists of magnetic gears which are mounted on its outer surface. These magnetic gears will then transmit the torque to the low-speed rotor. As shown in Fig. 1.4, the diode rectifier links the machines rotor with dc boost windings to guarantee a 15% increase in the torque. Integrating the magnetic gear in induction machines has been done in other studies such as [49], [51]–[53].

1.1.2 Synchronous Machines

Another type of electric machines with constant airgap is synchronous machine. It is worth mentioning that synchronous machines fit in both categories, constant airgap and variable airgap. Synchronous machines are also called constant-speed machines since they run at a precise synchronous speed [54]. They have higher torque density among other electric

machines [55]. These machines can be employed in low-speed and high-speed applications. Fig. 1.5 shows a two-pole three phase synchronous machine with a constant gap.

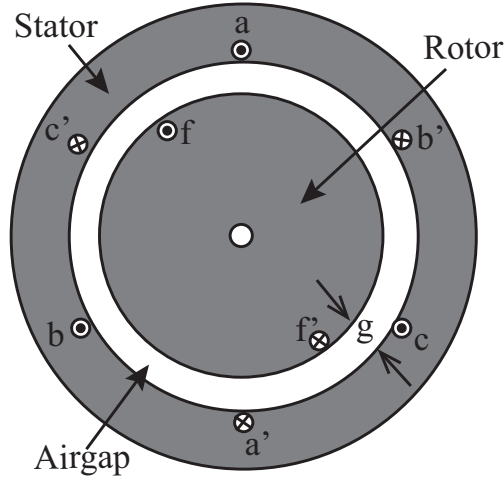


Figure 1.5. Synchronous Machine with Constant Airgap

The torque equation in synchronous machines is as shown in (1.4).

$$T_e = \left(\frac{3}{2}\right)\left(\frac{P}{2}\right)(\lambda_{ds}i_{qs} - \lambda_{qs}i_{ds}) \quad (1.4)$$

Eqn. (1.4) has been obtained using (1.5) in which K_s^r is as shown in (1.6) which is called the transformation matrix.

$$T_e = \left(\frac{P}{2}\right)[(K_s^r)^{-1}i_{qd0s}^r]^T \left\{ \frac{1}{2} \frac{\partial}{(\partial\theta)_r} [L_s](K_s^r)^{-1}i_{qd0s}^r + \frac{\partial}{\partial\theta_r} [L_{sr}]i_{qdr}^r \right\} \quad (1.5)$$

$$K_s^r = \begin{bmatrix} \cos(\theta_r - \theta) & -\sin(\theta_r - \theta) & 0 \\ \sin(\theta_r - \theta) & \cos(\theta_r - \theta) & 0 \\ 0 & 0 & 1 \end{bmatrix} \quad (1.6)$$

Note that in all equations shown above, L is representing the inductance, which is directly dependent on the reluctance and consequently proportional to the airgap.

1.2 Machines with Variable Airgap

Machines with variable airgap will have different airgap lengths during one complete cycle of the rotor. These machines normally have salient stator, rotor, or both. Fig. 1.6 shows a switched reluctance machine with variable airgap which has been studied in [56]–[58]. As it is shown in Fig. 1.6(b), the gap in this machine is changing between the minimum and maximum while the rotor is changing position.

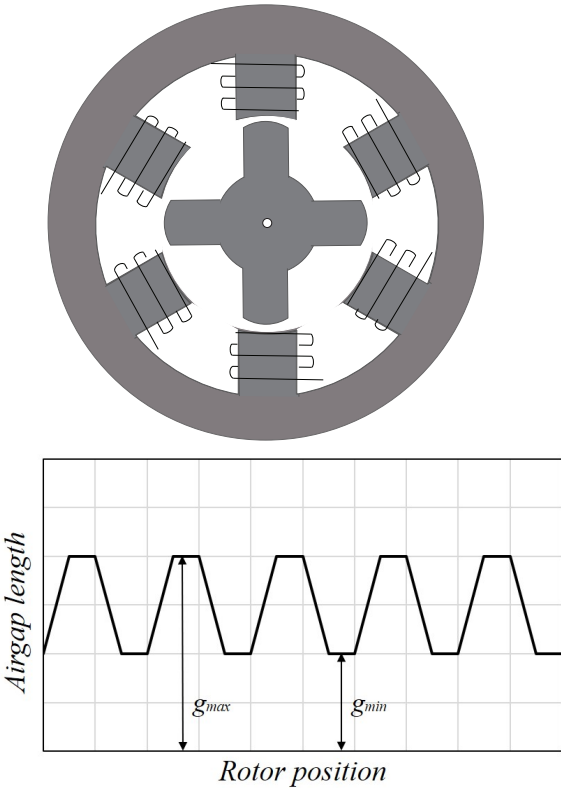


Figure 1.6. (a) switched reluctance machine with variable gap, (b) variable gap vs. position.

As it is shown in Fig. 1.6(b), when the tooth of the rotor is aligned with the tooth of the stator, there will be a smaller airgap than when these teeth are unaligned. In this case,

the gap is defined as variable gap. There exist studies in literature on electric machines with variable gaps [59], [60]. Below are several examples of high torque electric machines with variable airgaps.

1.2.1 Synchronous Machines

As mentioned in the constant airgap section, synchronous machines fit into variable airgap group as well as constant airgap group. In the case that the rotor, stator, or both are salient, the airgap will be variable in these machines. Fig. 1.7 shows a simple synchronous machine with a salient rotor.

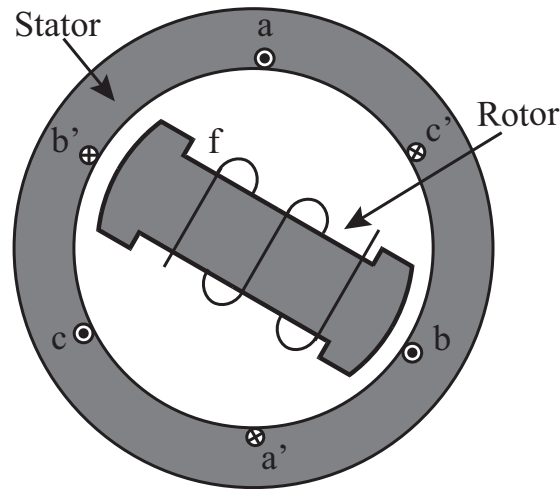


Figure 1.7. Synchronous Machine with Variable Airgap

In [61] the number of slot/pole combinations are studied to find the best combinations for low-speed high-torque applications of synchronous machines. Synchronous machines operate either as a machine or a generator. In synchronous generators the rotor winding is excited by dc voltage and will induce voltage to the stator. This magnetic field in the rotor winding will rotate the rotor with a constant speed inside the stator. In synchronous machines in turn, the AC power source will power up the stator, which will generate a magnetic field. This magnetic field inside the stator rotates the rotor. Synchronous machines along with induction machines are the most widely used type of AC machines.

1.2.2 Permanent Magnet Machines

Permanent magnet AC machines are the same type of machines as synchronous machines with the difference that the field windings in the synchronous machines are now replaced with permanent magnets [62]. Permanent magnet machines have advantages such as fast dynamic performance and high torque or torque per machine volume (torque density), and ease of control relative to alternative machines. [63]-[64]. Interior Permanent Magnet Synchronous Machines (IPMSM) are desirable for electric vehicle (EV) applications due to their high power and torque density. In [65] the shape of the rotor slots, which contain the magnet bars, has been optimized to reduce the cogging torque and increase the torque. PM machines conventionally are classified into two different types, i.e. permanent magnet material on the rotor and permanent magnet material on the stator. In [66] it has been proposed a permanent magnet machine with pm materials on both rotor and the stator. This paper claimed that having the dual excitation would result into a higher torque per volume. Using an extra set of permanent magnets on the ferromagnetic segments of the stator in a magnetic gear has been studied in [53]. This study presents that by adding an extra set of permanent magnets on the stationary part, the torque density will increase by 20 %. Fig. 1.8 shows this high torque density triple permanent magnet excited magnetic gear.

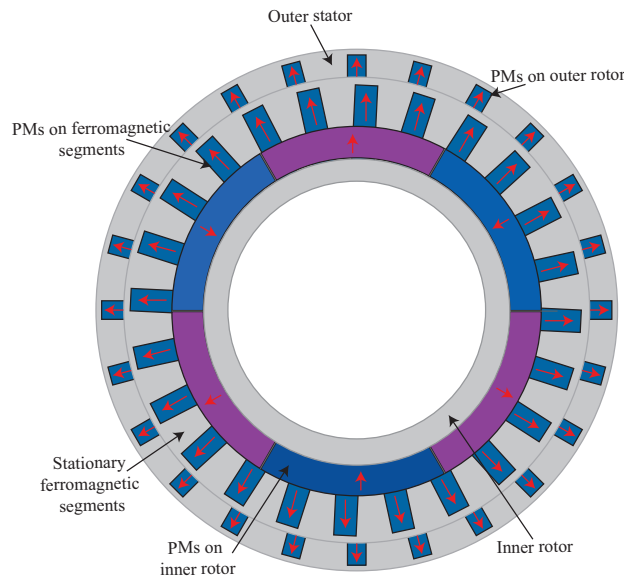


Figure 1.8. Triple PM excited Magnetic Gear

One of the possibilities to get a higher torque is to maximize the radius of the rotor. An outer rotor claw pole stator has been proposed in [67] in which the torque density is higher than the conventional machines due to the radius of the rotor and also the claw pole structure of the stator. However, there are also drawbacks for these designs such as higher stator leakage when the flux is traveling from one pole to the other pole. [68] proposed a new magnetic-planetary-gear permanent magnet brushless machine for HEVs, which can achieve mixing flexibility as well as power split. It also shows that a small size and light weight as well as reliability can be obtained in this machine by incorporating the concept of no-contact mechanisms of magnetic gear. It is evident that by reaching a smaller size in a machine the torque density will be higher.

1.2.3 Interior Permanent Magnet Synchronous Machines

Interior permanent magnet synchronous machines are among the most popular electric machines used in electric vehicles [23]. These machines contain rare-earth magnetic material which is costly and at the same time have negative impacts on earth. Therefore, one of the high demand in electric vehicle (EV) industry is to decrease the amount of rare earth magnetic material or electric machines that are rare earth free machines. In [23] it has been proposed a switched reluctance machine, which does not contain any rare earth material and also is competitive with IPMSM in terms of torque density and efficiency. Although switched reluctance machines (SRMs) are low cost and simple in design, they have lower torque density compared to other AC machines. This means that this machine produces low torque with respect to its volume. In [56] it has been proposed to employ low cost magnets on the SRM in order to increase its torque density and efficiency. It is worth mentioning that a none-rare earth magnet has been used in this research. The low cost magnets are located in stator yoke to avoid losing the capability of wide speed operation.

1.2.4 Synchronous Reluctance Machine

A comparison study between permanent magnet synchronous machine and synchronous reluctance machine has been done in [69]. In this study, it is evident that in the low power

machines use of permanent magnets does not change the dimensions of the machine. Also, in cases that weight and size does not matter the synchronous reluctance machine can be more desirable than the permanent magnet synchronous machine due to its reliability and low cost. In this paper, it was also mentioned that in machines with high power having rare earth magnets is more effective.

1.2.5 Permanent Magnet Flux Switching Machines

Recently the permanent magnet flux switching machines has gained interest in the past decades [70]-[71]. Although these machines have been proposed in different applications such as wind generation and aerospace, they are known to have high torque ripples because of the salient stator and rotor. Flux switching permanent magnet machines have stator being equipped by both magnets and armature windings. In this case, the rotor will have a robust and simple structure which will make the FSPM machines suitable for high-speed applications [72]. Fig. 1.9 shows the machine that has been studied in [72].

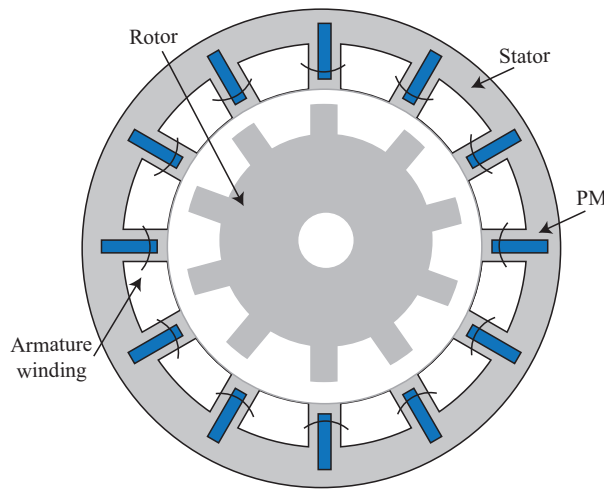


Figure 1.9. Flux switching permanent magnet

In [73] a 36/34 pole nine phase permanent magnet flux switching machine has been presented which will generate higher levels of torque density with lower torque ripples. Changing the rotor configuration to a partitioned rotor in flux switching PM machines, the stator flux leakage will decrease as well as the utilization of the PM magnets, which becomes efficient

[74]. Due to the high price of rare earth magnetic material, one of the main goals in developing permanent magnet machines is to reduce the magnets volume, which has been the main purpose in [75].

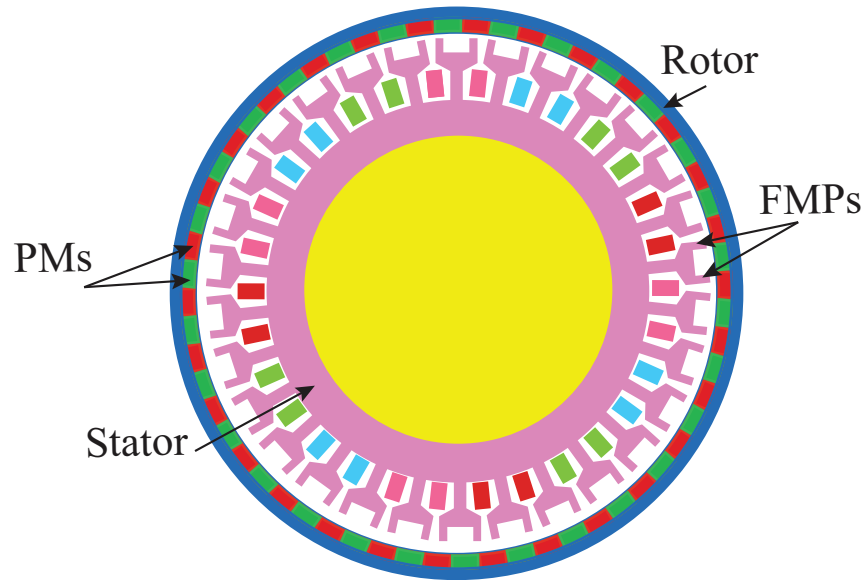


Figure 1.10. Permanent Magnet Vernier Machine

1.2.6 Permanent Magnet Vernier Machines

One type of permanent magnet electric machines that has gained attention in the literature recently is permanent magnet vernier machine. These machines are normally used in low-speed, high torque applications. [76]–[79]. Vernier machines are one type of permanent magnet machines with the difference in number of stator and rotor poles. It has been claimed in [80] that this type of machine will generate high torque density in compare to regular PM machines due to their special operation principle that is the magnetic gear effect. Fig. 1.10 shows a typical permanent magnet vernier machine.

One of the disadvantages of permanent magnet vernier machines is their higher cost due to the permanent magnets used in stator and rotor poles. Due to this fact there are studies presented in the literature, which have focused on decreasing the cost of the permanent magnet vernier machine. In [59] a permanent magnet vernier machine has been proposed

which adopts surface-mounted uni-polar rare-earth PM in rotor, which in turn will reduce the amount of PM used in the machine by half and also reduces the flux leakage.

1.3 Machines with Eccentric Airgap

Machines with eccentric airgaps can reach the airgap of almost zero at the point of contact between the stator and the rotor. In these machines, the rotor will have both the rotational and the transnational movement at the same time. While having these movements, when the rotor touches the stator, the airgap will be almost equal to zero. Although, due to the roughness of the material the airgap will never be absolute zero but it has a very small length. It is worth mentioning that even in the simulation of the machines with eccentric gap, it is not possible to have an airgap of zero as it will result into an infinite force, as shown in (1.7).

$$f = \frac{ki^2N}{g^2} \quad (1.7)$$

Fig. 1.11(a) shows an electric machine with eccentric gap that has been studied in [81]. As it is evident in Fig. 1.11(b) the airgap will reach almost zero at the points of contact between the stator and the rotor. Reaching the minimal airgap in these machines lead to a higher force and consequently a higher electromagnetic torque. These machines are called rolling rotor electric machines in the literature. An airgapless electric machine with both external and internal rotor has been studied by the authors in [82]-[83]. Another example of rolling rotor machines is rolling rotor switched reluctance machine that has been modeled and simulated in [81]. The difference between the modeling and simulation of the rolling rotor machines in [81] and [82] is the method of excitation of the stator poles as well as the type of the rotor. In [81], internal rotor has been used while in [82] external rotor has been used. Airgap-less Electric machine is an eccentric gap type of machine which is discussed in the third chapter of this dissertation.

One of the main advantages and characteristics of electric machines is their ability to produce high torque. Although due to their size, they cannot be used in many applications.

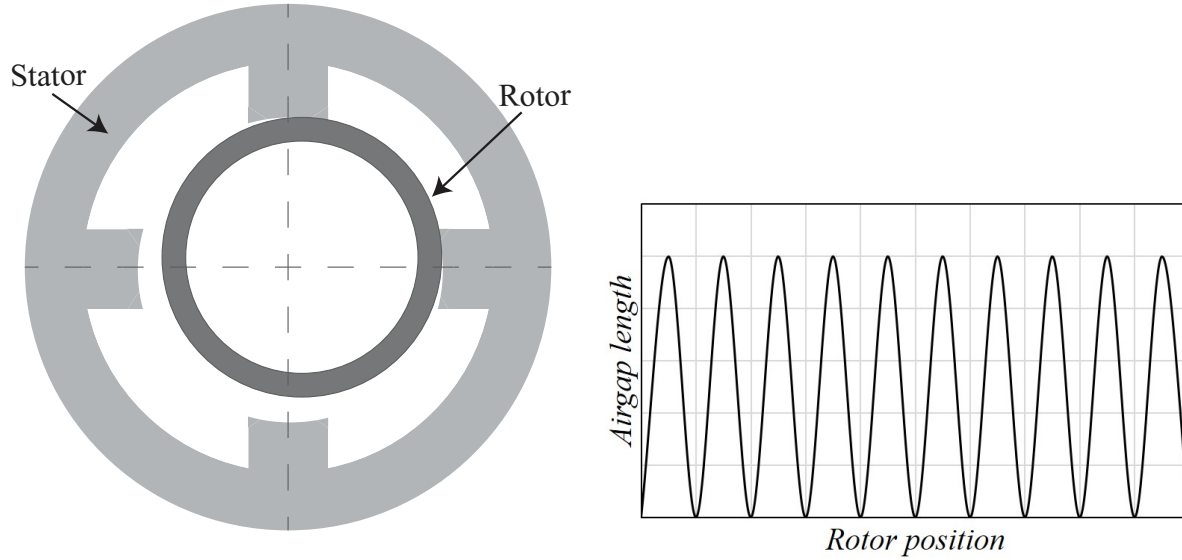


Figure 1.11. (a) switched reluctance machine with a rolling rotor, and (b) eccentric gap vs. position

In this case, the torque density will be the main subject of interest, i.e. torque per machine volume. In addition, the high torque density and high efficiency are the two main requirements for electric machines as saving energy has been one of the main focuses in the world [84]. The cross-sectional area of a basic electric machine is as shown in Fig. 1.12. Based on the type of the machine, the stator can have different numbers/types of poles as well as the rotor. In conventional electric machines, the rotor will be connected to a shaft inside the electric machine and will only have the rotational movement.

1.4 Scientific Outcomes

This dissertation is mainly focused on the research and development of airgap-less electric machines with internal and external rotors. The first outcome of this dissertation was a paper published in the 2017 IEEE International Electric Machines and Drives (IEMDC) conference. In this conference, the design, operation, control, and system integration of electrical machines

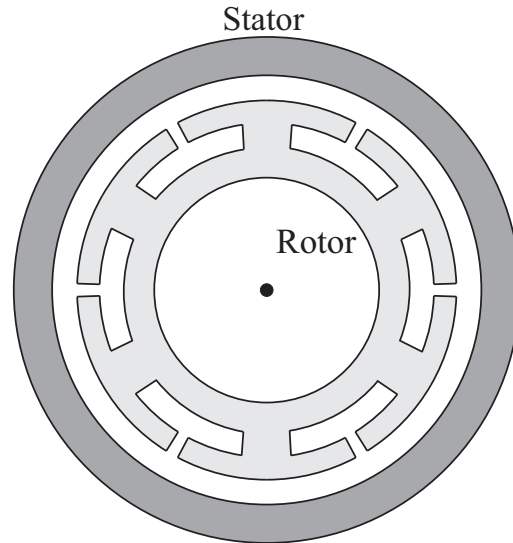


Figure 1.12. Electric machine Diagram

and the power electronic drives that implement their applications are addressed. The paper that was published in this conference (Airgap-less electric motor: A solution for high-torque low-speed applications) presented the proposed airgap-less electric machine with an external rotor that is described in detail in chapter III of this dissertation. The second outcome of this dissertation was a paper published in 2017 IEEE Energy Conversion Congress and Exposition (ECCE). This conference brings professionals together to discuss the latest advances in energy conversion technologies. The paper published in this conference (Internal rotor airgap-less electric motors) presented the airgap-less electric machine with an internal rotor and six phases that is presented in the second chapter of this dissertation. The third outcome of this research was a journal paper published in 2018 IEEE Transactions on Industrial Electronics. This transaction enfold the applications of electronics, controls, and computational intelligence for the improvement of industrial and manufacturing systems. This transaction is among the high impact factor transactions in IEEE with the impact factor of 7.515. The journal paper published in this transaction presented the airgap-less electric machine along with the experimental results that were obtained through the development of this machine. Apart from airgap-less electric machine, there has been a research on a solar microinverter which will be described briefly in this section but is not included in this dissertation. This project was primarily on a grid-tie inverter for solar applications which was funded by NSF-

I-Corps program and it is worth mentioning that it acted as a part of the PhD tuition and stipend. I-corps program is a course provided by NSF in which it gives academic people the opportunity to commercialize their product which has been developed in the school laboratory. During this program, which is around 6 months, there are weekly reports and meetings with I-Corps instructors. At this time, groups will have the opportunity to present their research and developed product to the other participants and get some feedback from them. After every presentation, there will be some suggestions from the instructors as well as other groups. But the most important part of this course is that it is teaching academic people to get out of the academia environment, go to industry and talk to real customers. One of the main assignments of this program was interviewing as much customers as possible and decide whether the developed product needs a pivot or is good enough for commercializing. The project of grid-tie solar inverter was presented to more than hundred customers. The outcome of these interviews lead to a pivot in this project which was proposing a unique solar microinverter that was patented for it's shape. This solar microinverter is in the shape of a triangle and can be fixed at the back of the solar panel with only one screw and this will reduce the labor time (boots on the roofs) and costs of installing a solar panel. This program was an opportunity to learn and involve in the industry and business side of developing a product. There has also been a journal paper submitted for the simulation and analysis of the airgap-less electric motor using different integration methods to Multidisciplinary Digital Publishing Institute (MDPI) journal, which was not accepted. This scientific journal is an open access publisher.

In addition to the above publications in airgap-less electric machines, the mechanical and geometric approach for these machines with internal rotor has been done in [85]. In this study the author proposed that the rough geometric calculations proposed will result into the maximum electromagnetic torque along with the lowest possible ripple.

2. AIRGAP-LESS ELECTRIC MACHINE WITH AN INTERNAL ROTOR

This chapter presents the proposed airgap-less electric machine with an internal rotor. This chapter presents the main reasons that the eighteen teeth/nine-phase electric machine is studied mainly in this dissertation. Although electric machines have significant torque density (i.e., torque per machine volume), there are specific applications (e.g., cranes and winches) where electric machines are not considered a competitive technology as compared to hydraulic machines due to torque density limitations.

Hydraulic machines are commonly used in industrial and commercial applications for their compact size, high power-to-weight ratio, and reliability. In many cases, these characteristics make it preferable over electric machines, especially when high torque density is a critical requirement [86]-[87]. Although hydraulic systems are widely employed in industrial applications (e.g., cranes and winches), they face two major problems, i.e., (1) remarkably inefficient with efficiencies ranging from 6% to 40% and (2) present a complex braking system [88].

Achieving high-torque density has always been one of the targets while designing electric machines [35], which has inspired new designs as presented in the technical literature [41]. For example, the torque generated by switched reluctance machines and machines with partitioned rotor are one of the highest among electric machines. However, they still do not generate torque density that is comparable to hydraulic machines. Other examples of non-conventional designs of electric machines and control strategies proposed by industry and academia include: 1) a dual rotor structure along with a dual excitation [44], 2) an outer rotor hybrid excitation [45], 3) new control strategies proposed in order to enhance the mechanical torque [46], and 4) injection of third harmonic current [47].

Traditional electric machines are characterized by the presence of an airgap (either constant or variable), which allows the movable part (rotor) to spin freely. Although the airgap presence is fundamental in creating rotational movement, designers try to minimize its size to maximize internal flux and consequently torque.

This new family of machines is based on the principle behind magnetic devices that produce linear force, such as relays. Note that the expression for force in this type of device indicates that the attraction observed by the movable part is directly proportional to the current squared (i^2), number of turns (N), and inversely proportional to the airgap squared (g^2), i.e., $f = ki^2N/g^2$; where k is a function of the permeability of the material and its dimensions. Hence, the force is maximized if the gap is minimal (i.e., airgap-less), which happens when the movable part touches the fixed one. It is worth mentioning that even using the term airgap-less, g is not zero due to the roughness of the contact between both parts (movable and fixed). The proposed machines are therefore driven by the concept of airgap-less and maximum attraction force.

2.1 Machine With Three Poles and Three Phases

Traditional electric machines are characterized by a presence of an airgap (either constant or variable), which allows the movable part (rotor) to spin freely. Although the airgap presence is fundamental in creating rotational movement, designers try to minimize its size to maximize internal flux and consequently torque. This new family of machines is based on the principle behind magnetic devices that produce linear force, such as relays with C-core as shown in Fig. 2.1.

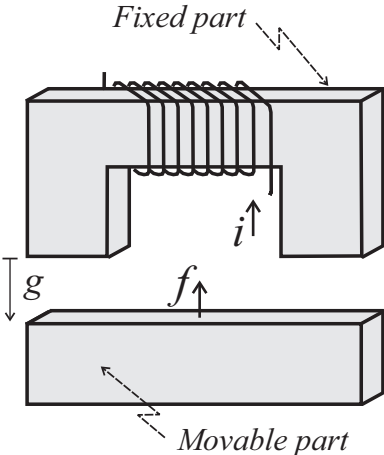


Figure 2.1. C-core magnetic device (relay).

Note that the expression of force in this type of device indicates that the attraction observed by the movable part is directly proportional to the current square (i^2), number of turns (N), and inversely proportional to the airgap square (g^2), i.e., fki^2N/g^2 ; where k is a function of the permeability of the material, and its dimensions. Therefore, the force is maximized if the gap is minimal (i.e., airgap-less), which happens when the movable part touches the fixed one. Notice that even using the term airgap-less, g is not zero due to the roughness of the contact between both parts (movable and fixed). The proposed machines therefore are driven by the concept of airgap-less and maximum linear force. The proposed machines use physical contact between the stator and rotor to maximize force and its rotational torque. Fig. 2.2 shows a 3D sketch of the proposed concept, which shows its stator and rotor pieces. Both stator and rotor are made of ferromagnetic material. While Fig. 2.2(a) shows each component of this machine as a single unit, Fig. 2.2(b) highlights each component separately, i.e., front and end caps along with the main stator body. The stator main part is comprised of three poles, as seen in Fig. 2.2(c), where a synchronized magnetic flux will be generated in order to guarantee continuous movement. Each stator pole will be wrapped by windings for magneto-motive-force (MMF) generation, as shown in Fig. 2.3(a).

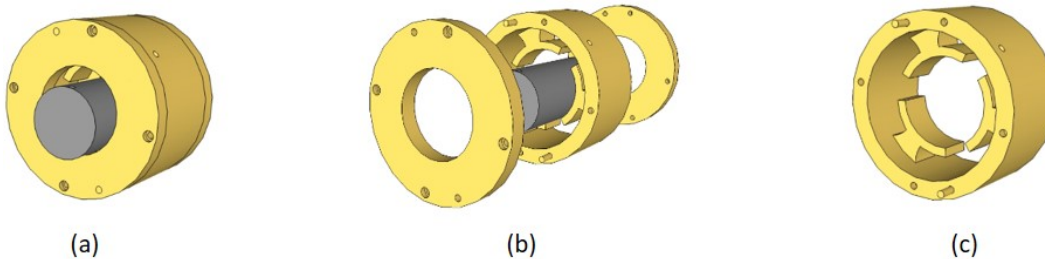


Figure 2.2. 3D views of the proposed concept.

Note that when the current i_1 is applied to the stator pole s_1 , its flux will attract the rotor. When i_1 reduces while i_2 increases, the rotor will roll over the stator towards s_2 . The profile of the currents presented in Fig. 2.3(b) will guarantee continuous movement of the rotor. Fig. 2.3(c), in turn, shows a sequence of snap shots that demonstrates how the proposed machine operates. From the left to the right, Fig. 2.3(c) shows a specific situation

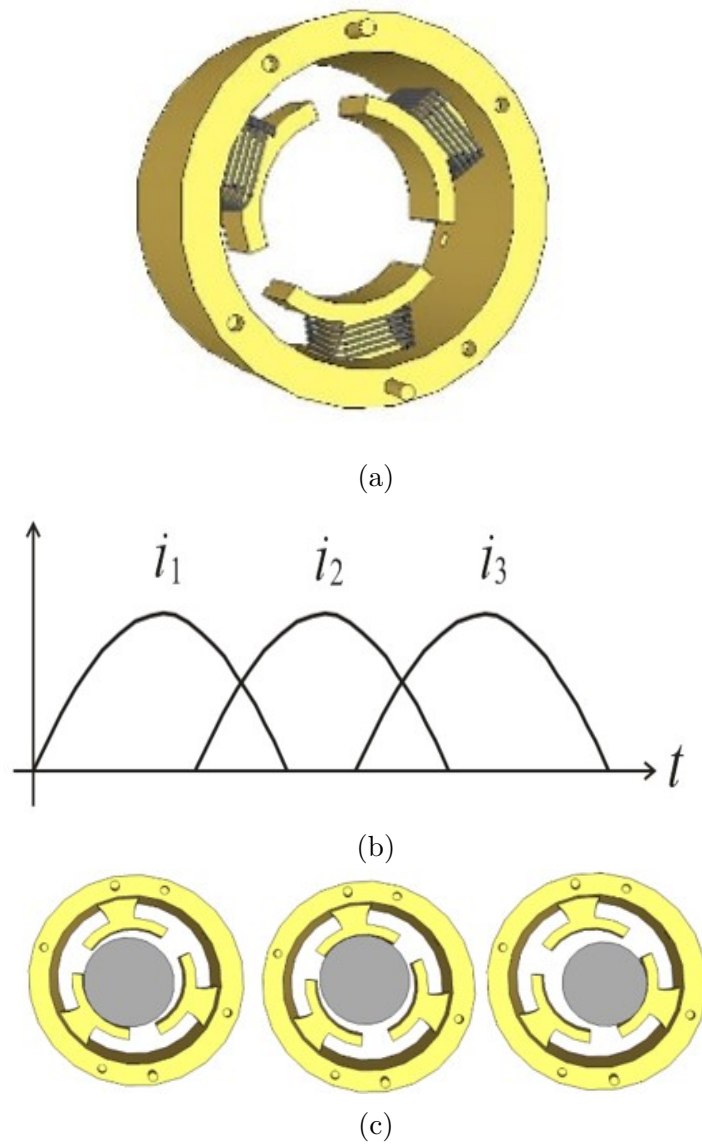


Figure 2.3. (a) Location where the winding is placed for MMF creation. (b) Profile of stator current for continuous generation. (c) Sequence of shots showing a continuous rotor movement..

where the rotor movement goes clock wise. It is noteworthy to mention, the rotation created by this machine is similar to the one created by hydraulic machines [89], as seen in Fig. 2.4. Both types of machines (i.e., the proposed airgap-less electric machine and the hydraulic machine) have a rigid body rotor with combined translational and rotational movements.

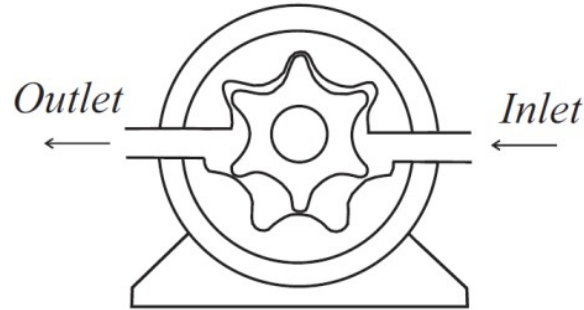


Figure 2.4. Hydraulic machine.

Fig. 2.5(a) presents the trajectory of the rotor center of the proposed machine and how the rotor movement can be obtained by a combination of rotational and translational movements. A mechanical gear can be used to convert this combined translational and rotational movement into rotational only movement if necessary for a specific application [see Fig. 2.5(b)]. This type of gear box is also used in hydraulic machines. As previously stated, although the presence of the airgap is necessary for creating rotational movement, designers try to minimize its size to maximize internal flux and consequently torque. However, the gap size in a traditional design should be big enough to guarantee that there is no physical contact between stator and rotor, which may cause damage to the machine and consequently cease its operation.

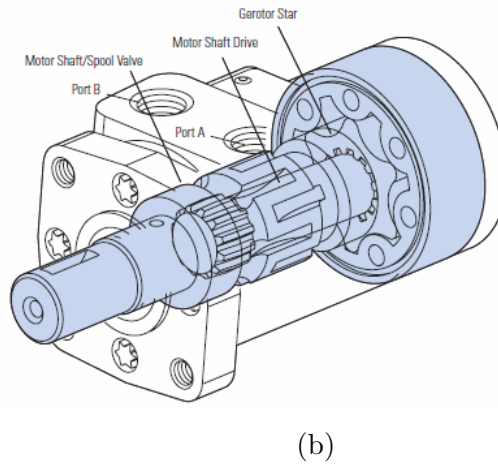
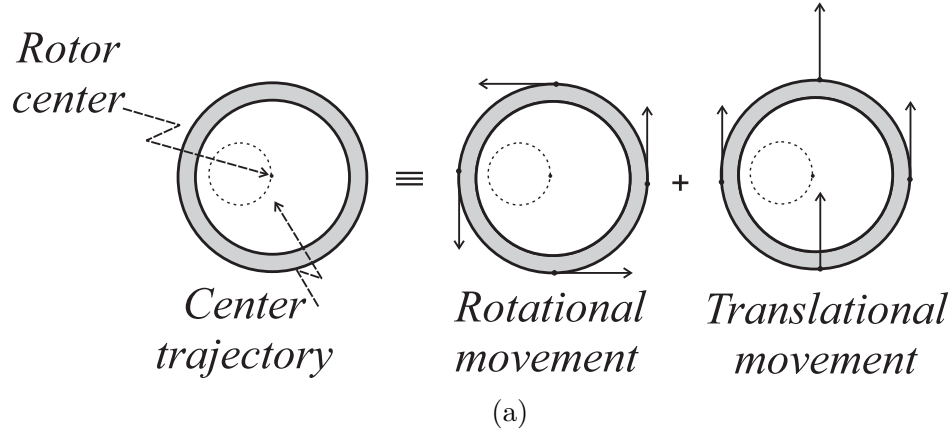


Figure 2.5. (a) Combined rotor translational and rotational movements. (b) Gear box.

2.1.1 Machine Modeling

As the rotor spins following the stator pole excitation, its center spans a circle as described in Fig. 2.5(a). Due to this movement, the gap between the stator and rotor changes as a function of the angular position of the rotor (θ). The flux travels in a path that is normal to both the stator and the rotor, and in this geometrical configuration is expected to fringe slightly. To simplify the initial derivation for an expression of the gap, only a path normal to the stator was considered, which is reasonable if the rotor radius is close to the stator radius. Notice from Fig. 2.6 that the air gap expression $[g(\theta)]$ can be written as a function of angular position θ . The expression for the gap can be therefore derived as shown below:

$$g(\theta) = r_2 - r_{21} \cos(\theta) - \sqrt{r_1^2 - r_{21}^2 \sin^2(\theta)} \quad (2.1)$$

where r_1 , r_2 , and r_{21} are the radius of the rotor, stator, and the difference between both radii (i.e., $r_{21} = r_2 - r_1$), respectively. The magnetic equivalent circuit of this machine, when only one pole is supplied with current can be modeled as shown in Fig. 2.7, in which \mathcal{R}_1 and \mathcal{R}_3 are the reluctances associated with the gaps at the front and back caps of this machine and \mathcal{R}_2 is the gap associated with the pole of the stator.

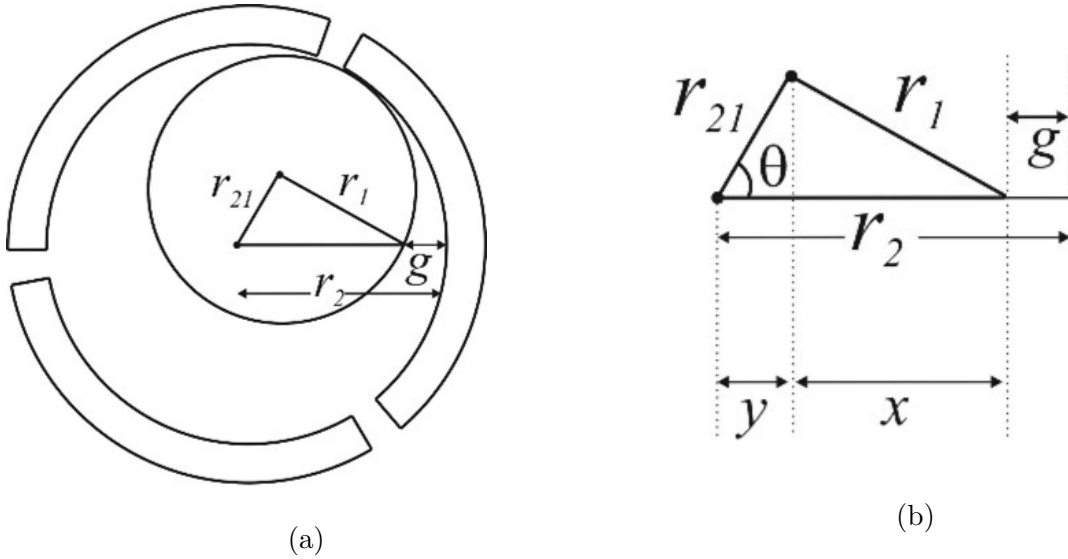


Figure 2.6. Geometry approach used for air gap derivation.

If the reluctance of the magnetic core is neglected and only the reluctance of the air gap is considered, the self-inductance of the device can be expressed as a function of the angle as well, which leads to:

$$L = N^2 / \mathcal{R}_T \quad (2.2)$$

in which N is the number of turns for the stator pole and \mathcal{R}_T is the total reluctance seen by the flux (ϕ) in the circuit shown in Fig. 2.7. This reluctance can be calculated as shown below:

$$\mathcal{R}_T = (\mathcal{R}_1 || \mathcal{R}_3) + \mathcal{R}_2 \quad (2.3)$$

where: $\mathcal{R}_1 = g / \mu_0 A_{g1}$, $\mathcal{R}_2 = g / \mu_0 A_{g2}$, and $\mathcal{R}_3 = g / \mu_0 A_{g3}$. Also, A_{g1} , A_{g3} , and A_{g2} are the areas associated with front cap, back cap, and the stator pole respectively. Fig. 2.8. shows

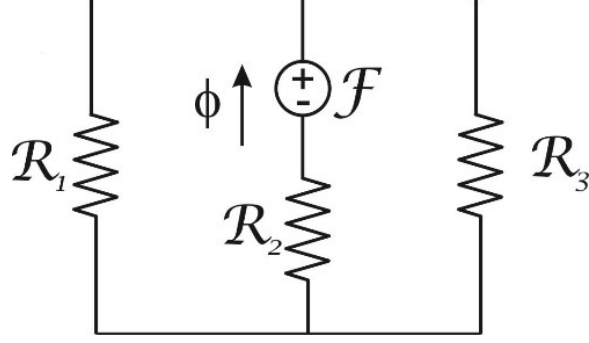


Figure 2.7. Magnetic equivalent circuit of the machine shown in Fig. 2.2 when only one pole is supplied with current.

the developed diagram of the proposed electric machine. In this figure is shown a sequence of shots as the rotor spins to highlight two different scenarios in terms of rotor positioning and stator current values. For instance, Fig. 2.8(a) shows a rotor position when the currents are in sector 1 as presented in Fig. 2.8(b). In this sector, the currents in poles 2 and 3 are zero ($i_2 = i_3 = 0$), which eliminates the mutual inductances with respect to pole 1. Therefore, the self-inductance L_{11} is defined using 2.2. Note that flux lines created at pole 1 go to the front-cap and back-cap completing a C-core as seen in Fig. 2.1. In sector 2 as shown in Fig. 2.8, current i_1 decreases while i_2 increases, which lead the rotor to rotate to the right [see Fig 2.8(c)]. During this interval of time, in addition to the flux lines presented in Fig. 2.8(a), there are also flux lines that cross both poles 1 and 2 through the rotor. As the rotor moves further right, the same flux behavior is observed for poles 2 and 3 in a cyclic way. As it is shown in 2.2, the inductance depends on the number of turns and the reluctance of the path. Reluctance of the gap is calculated in 2.3. The area of the front-cap (A_{g1}) is the same as the area of the back-cap (A_{g3}) and it is considered as A_g . Substituting 2.3 into 2.2, the self-inductances for each pole will be as shown below:

$$L_{11} = 2N_1^2 \mu_0 A_{g2} A_g / g(\theta) (A_{g2} + 2A_g) \quad (2.4)$$

$$L_{22} = 2N_2^2 \mu_0 A_{g2} A_g / g(\theta - 2\pi/3) (A_{g2} + 2A_g) \quad (2.5)$$

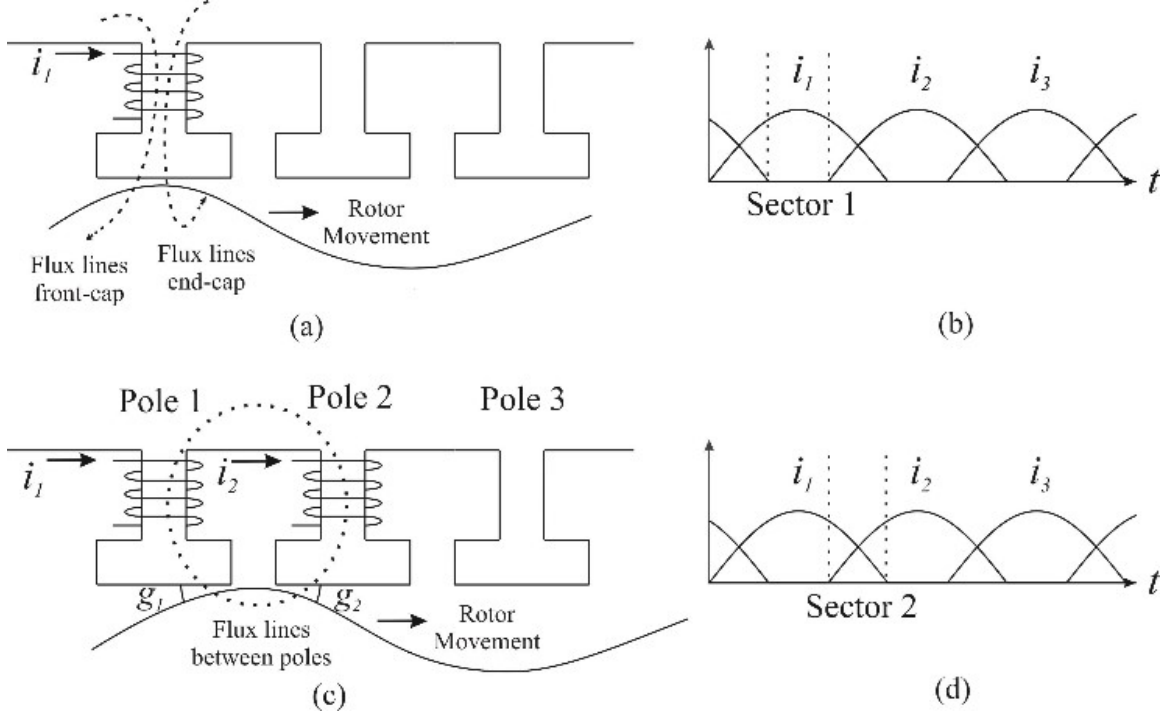


Figure 2.8. Developed diagram of the proposed electric machine.

$$L_{33} = 2N_3^2\mu_0A_{g2}A_g/g(\theta + 2\pi/3)(A_{g2} + 2A_g) \quad (2.6)$$

Assuming $r_1 \approx r_2$ in 2.1, this equation can be written as:

$$g(\theta) = r_{21} [1 - \cos(\theta)] \quad (2.7)$$

Substituting 2.7 into 2.4, 2.5, and 2.6, the self-inductances can be defined as:

$$L_{11} = 2N_1^2\mu_0A_{g2}A_g/r_{21}(1 - \cos(\theta))(A_{g2} + 2A_g) \quad (2.8)$$

$$L_{22} = 2N_2^2\mu_0A_{g2}A_g/r_{21}(1 - \cos(\theta - 2\pi/3))(A_{g2} + 2A_g) \quad (2.9)$$

$$L_{33} = 2N_3^2\mu_0A_{g2}A_g/r_{21}(1 - \cos(\theta + 2\pi/3))(A_{g2} + 2A_g) \quad (2.10)$$

Considering a case in which the rotor is touching a point between two poles is shown in Fig. 2.8(c). This region is also shown in Fig. 2.8(d) as sector 2, with respects to the currents in the machine. It is obvious that both currents i_1 and i_2 exist in this region so the rotor will be attracted to a point between poles 1 and 2. The same procedure happens when current i_2 and i_3 exist at the same time or currents i_1 and i_3 exist at the same time, in which the rotor will be attracted to a point in between poles 2 and 3 or poles 1 and 3 respectively. In this case, there will exist mutual inductances between poles. These mutual inductances can be calculated using 2.2:

$$L_{12} = 2N_1N_2\mu_0A_gA_{g2}/(g_1(\theta) + g_2(\theta))(2A_g + A_{g2}) \quad (2.11)$$

$$L_{13} = 2N_1N_3\mu_0A_gA_{g2}/(g_1(\theta) + g_3(\theta))(2A_g + A_{g2}) \quad (2.12)$$

$$L_{23} = 2N_2N_3\mu_0A_gA_{g2}/(g_2(\theta) + g_3(\theta))(2A_g + A_{g2}) \quad (2.13)$$

in which: $g_1(\theta) = r_{21}[1 - \cos(\theta)]$, $g_2(\theta) = r_{21}[1 - \cos(\theta - 2\pi/3)]$, and $g_3(\theta) = r_{21}[1 - \cos(\theta + 2\pi/3)]$.

Now that the self- and mutual-inductances have been calculated, the flux linkages will be as shown below. It is worth mentioning that in the equations shown below the mutual inductances L_{12} , L_{23} , and L_{13} are the same as L_{21} , L_{32} , and L_{31} .

$$\lambda_1 = L_{11}i_1 + L_{12}i_2 + L_{13}i_3 \quad (2.14)$$

$$\lambda_2 = L_{21}i_1 + L_{22}i_2 + L_{23}i_3 \quad (2.15)$$

$$\lambda_3 = L_{31}i_1 + L_{32}i_2 + L_{33}i_3 \quad (2.16)$$

Using the expressions for flux linkages, the co-energy can be calculated as shown below:

$$w_c = \int \sum_{j=1}^J \lambda_j di_j \quad (2.17)$$

Using 2.8 - 2.16 in 2.17, the co-energy will be:

$$w_c = \left(\frac{1}{2}\right) \left(L_{11}i_1^2 + L_{22}i_2^2 + L_{33}i_3^2\right) + 2L_{12}i_1i_2 + 2L_{13}i_1i_3 + 2L_{23}i_2i_3 \quad (2.18)$$

The torque can be calculated as:

$$T_e = \partial w_c / \partial \theta \quad (2.19)$$

Using expressions 2.18 and 2.19, the expression of the torque will be as shown below:

$$\begin{aligned} T_e = & -\frac{r_{21} \sin(\theta)k1}{(r_{21} - r_{21} \cos(\theta))^2} - \frac{r_{21} \sin\left(\theta - \frac{2\pi}{3}\right)k2}{\left(r_{21} - r_{21} \cos\left(\theta - \frac{2\pi}{3}\right)\right)^2} - \frac{r_{21} \sin\left(\theta + \frac{2\pi}{3}\right)k3}{\left(r_{21} - r_{21} \cos\left(\theta + \frac{2\pi}{3}\right)\right)^2} \\ & + \frac{4r_{21} \sin\left(\theta + \frac{2\pi}{3}\right)k4}{\left(2r_{21} - r_{21} \cos\left(\theta + \frac{2\pi}{3}\right)\right)^2} + \frac{4r_{21} \sin\left(\theta - \frac{2\pi}{3}\right)k5}{\left(2r_{21} - r_{21} \cos\left(\theta - \frac{2\pi}{3}\right)\right)^2} + \frac{4r_{21} \sin(\theta)k6}{\left(2r_{21} - r_{21} \cos(\theta)\right)^2} \end{aligned} \quad (2.20)$$

2.1.2 Experimental Setup

A proof-of-concept laboratory prototype was built to validate the theoretical assumptions. The material selected for this first prototype is low carbon steel 1020, which has magnetic flux density saturation around 2 Tesla. Both stator poles and rotor will be built with low carbon steel 1020. Fig. 2.9(a) shows a photo of the proposed machine in perspective and assembled as a single unit. Fig. 2.9(b), in turn, depicts such a machine with the front cap removed from the stator body. Details about the internal pole structure and stator winding are presented in Fig. 2.9(c). Finally, Fig. 2.9(d) shows an upper view of the proposed machine connected to the drive system, which is show schematically in Fig. 2.10.

Fig. 2.11 shows experimental results collected for the proposed airgap-less electric machine. The profile of the current was implemented with a PWM control strategy operating

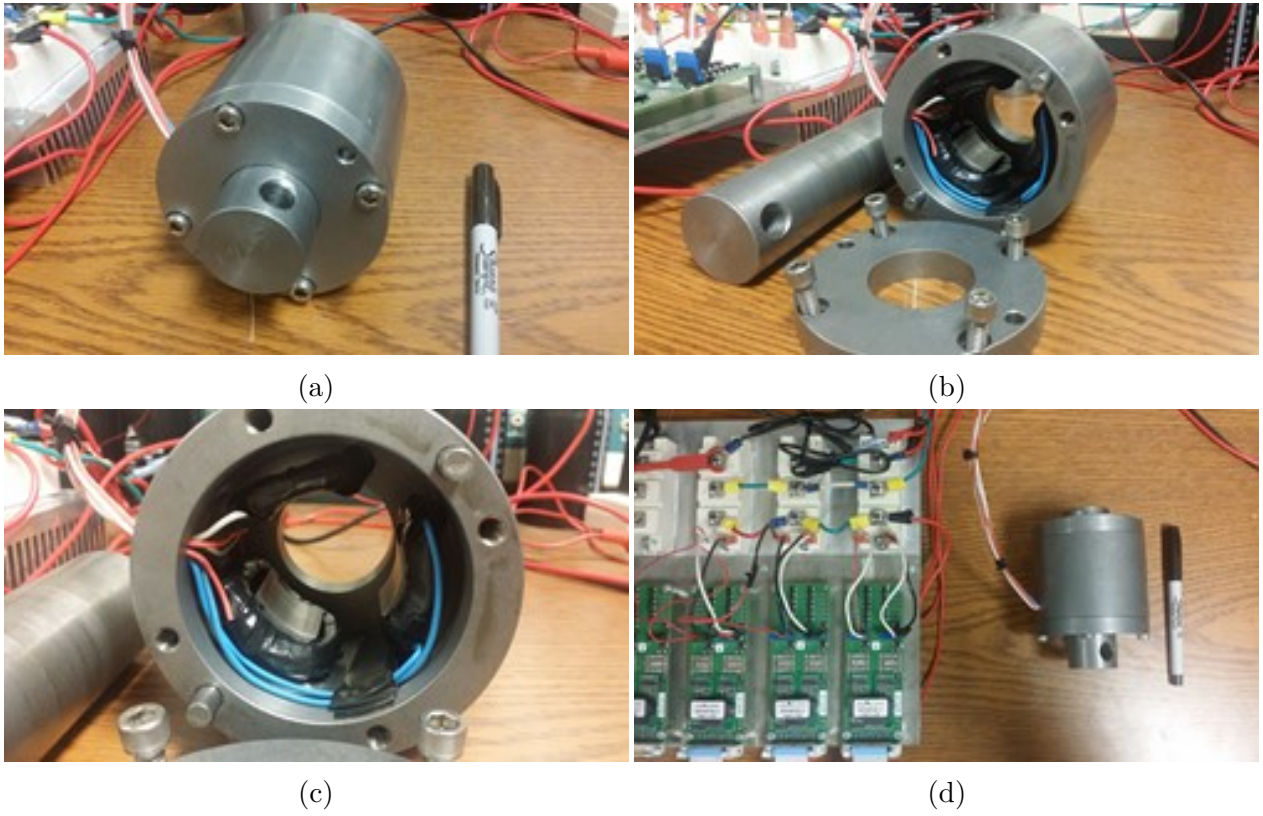


Figure 2.9. Photos of the proposed electric machine with its drive system.

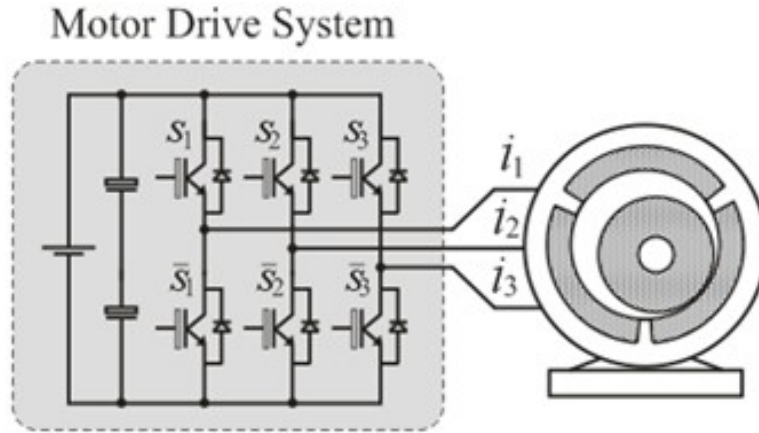


Figure 2.10. Machine drive system.

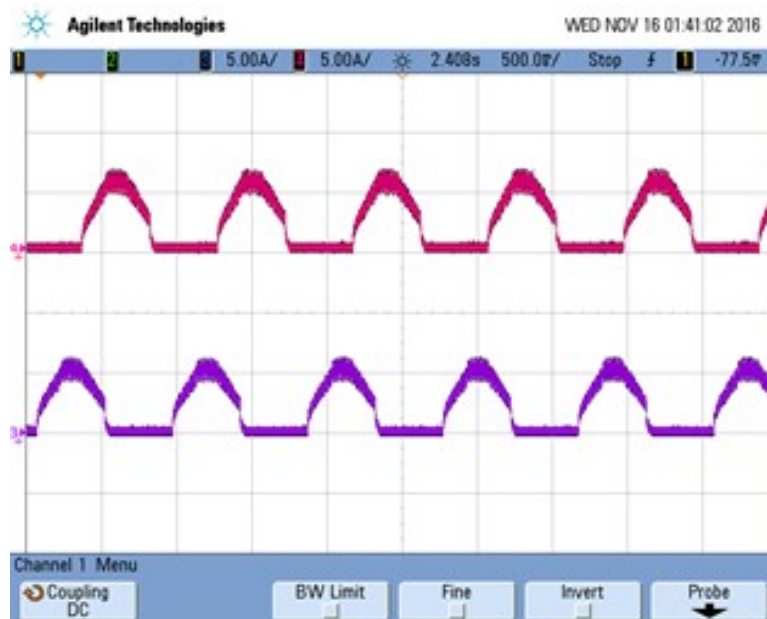


Figure 2.11. Experimental results: currents in poles 1 and 2.

in open loop. The top waveform presented in Fig. 2.11 is the current of pole 1, while the bottom one is the current of pole 2.

Although it was expected to have a smooth movement of the rotor inside the stator, movement was more like a stepper machine. For example when current is applied to pole 1, the rotor touches pole 1 until the point that current in pole 1 is zero. At this moment the current is already applied to pole 2 and as a result rotor (that is now released from pole 1) jumps and touches pole 2 and is not rolling smoothly. Based on this observation it

was decided to increase the number of poles in order to have smoother and more continuous movement. Next section presents a twelve pole six phase airgap-less electric machine with an internal rotor.

2.2 Airgap-less Electric Machine with Six Bipoles and Six Phases

As mentioned in the previous section, airgap-less electric machine uses physical contact between the stator and rotor to maximize force and rotational torque. Fig. 2.12 presents different views of a 3D sketch for the proposed machine. Fig. 2.12(a) shows the stator with six bipoles (twelve teeth), Fig. 2.12(b) presents the rotor. Fig. 2.12(c) and Fig. 2.12(d) highlight both the stator and rotor and how the rotor is allowed to touch the stator. The former shows a view in perspective while the latter depicts a top view.

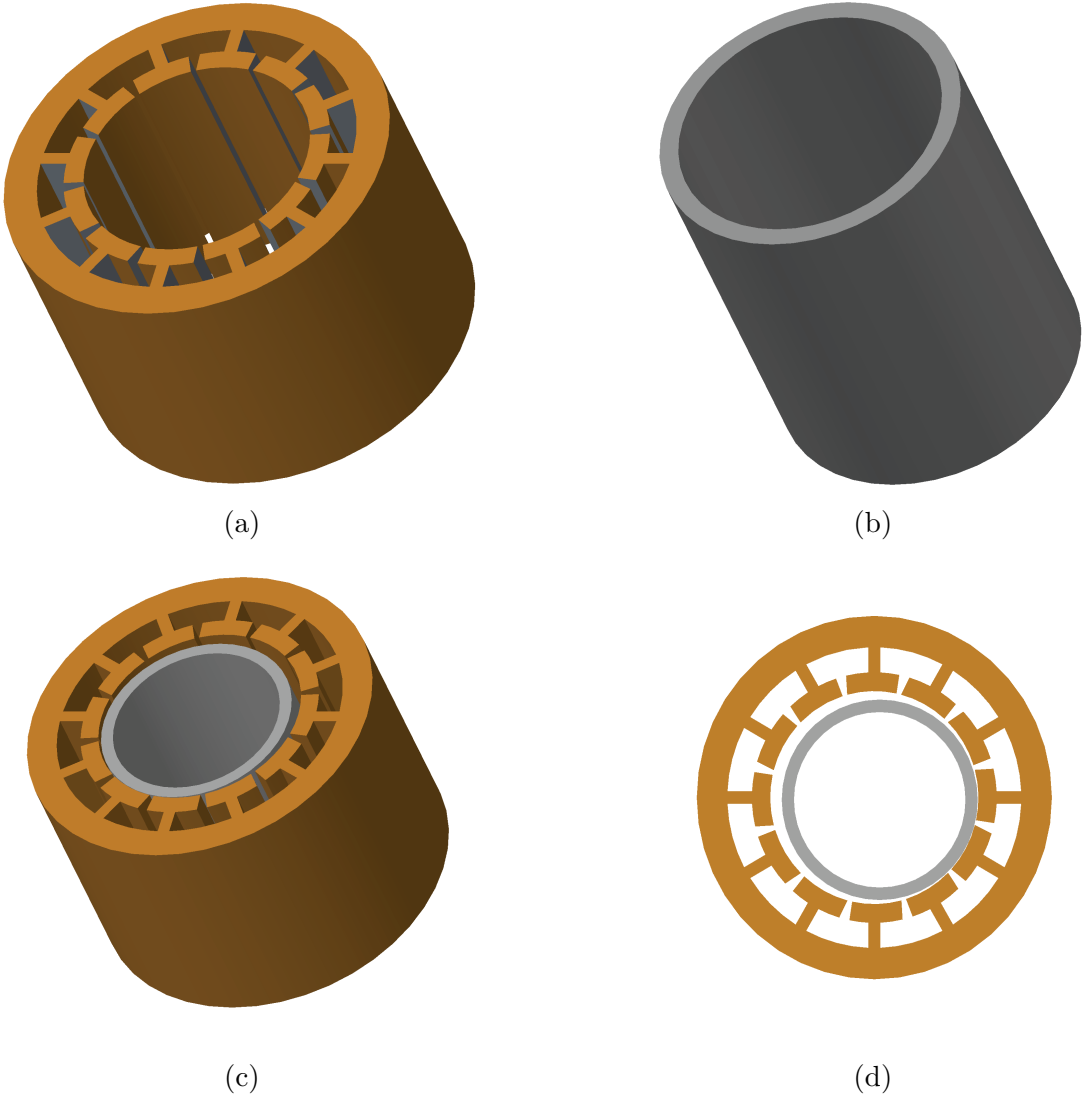


Figure 2.12. 3D views of the proposed 3 bipole machine.

This machine will be excited with a magnetic bipole configuration as shown in Fig. 2.13(a). Two teeth form a pair pole where one of the teeth is north while the other one is south emulating a C-core configuration. The continuous rotor movement is obtained by exciting these poles with a machine drive system as presented in Fig. 2.13(b). Fig. 2.14, in turn, shows a sequence of snap shots (top view) that demonstrate how the proposed machine operates, i.e., the rotor touches different positions of the stator as the excitation goes from bipole 1 to bipole 6 with a counter clock wise movement.

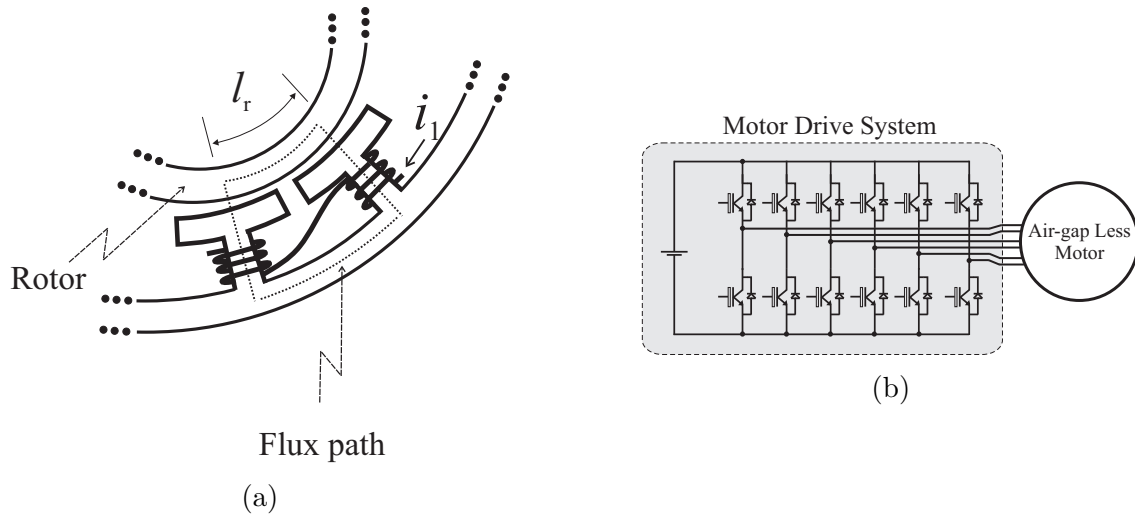


Figure 2.13. (a) Bipole configuration. (b) machine drive system.

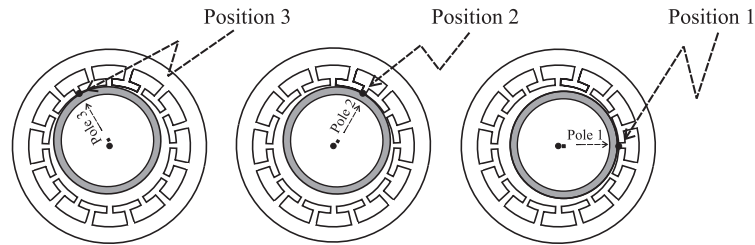


Figure 2.14. Sequence of shots showing a continuous rotor movement.

It is noteworthy to mention, the rotation created by this machine is similar to that of hydraulic machines, as seen in Fig. 2.4 in the previous section. Both types of machines (the proposed airgap-less electric machine and the hydraulic machine) have a rigid body rotor with a combined translational and rotational movements. A mechanical gear can be used to convert this combined translational and rotational movement into a rotational movement

only if necessary for a specific application. This type of gear box has been used in hydraulic machines and it is a firmly established technology which has also been shown in Fig. 2.5(b) in the preceding section.

2.2.1 Machine Modeling

As the rotor spins following the stator pole excitation, its center spans a circle. Due to this movement, the gap between the stator and rotor changes as a function of the angular position of the rotor (θ). θ is the angle of the touching point between rotor and stator, as shown in Fig. 2.15. Notice from this figure that r_2 (radius of the rotor) and r_1 (radius of the stator) were made large and small (respectively) to facilitate the visualization. Fig. 2.15(b) shows how the gap at position 1 (i.e., seen by the center of pole 1) can be written as a function of the angle θ .

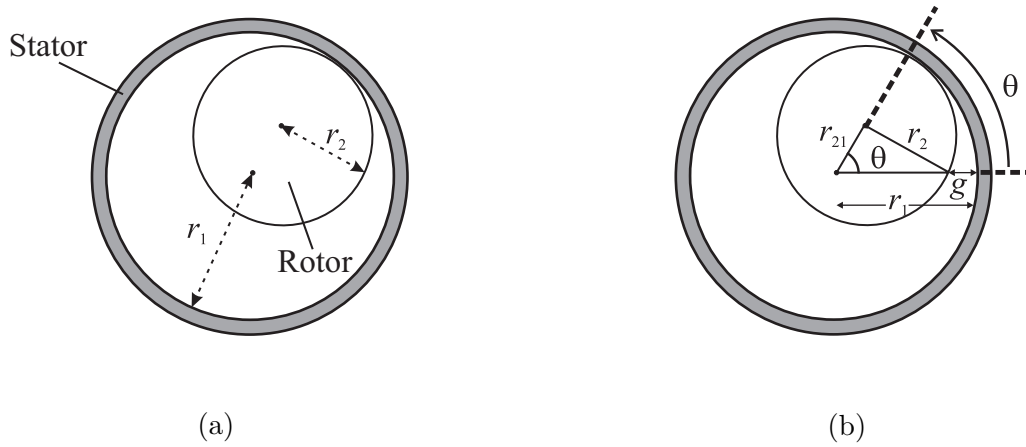


Figure 2.15. Geometric approach used for airgap derivation.

The expression of the gap can therefore be derived as shown below:

$$g(\theta) = r_2 - r_{21} \cos(\theta) - \sqrt{r_1^2 - r_{21}^2 \sin^2(\theta)} \quad (2.21)$$

where r_{21} is the difference between both radii (i.e., $r_{21} = r_2 - r_1$). In this design, the radius of the rotor and stator are close to each other, i.e. $r_1 \approx r_2$. Therefore, the gap expression can be simplified as done in (2.22).

$$g(\theta) = r_{21}[1 - \cos(\theta)] \quad (2.22)$$

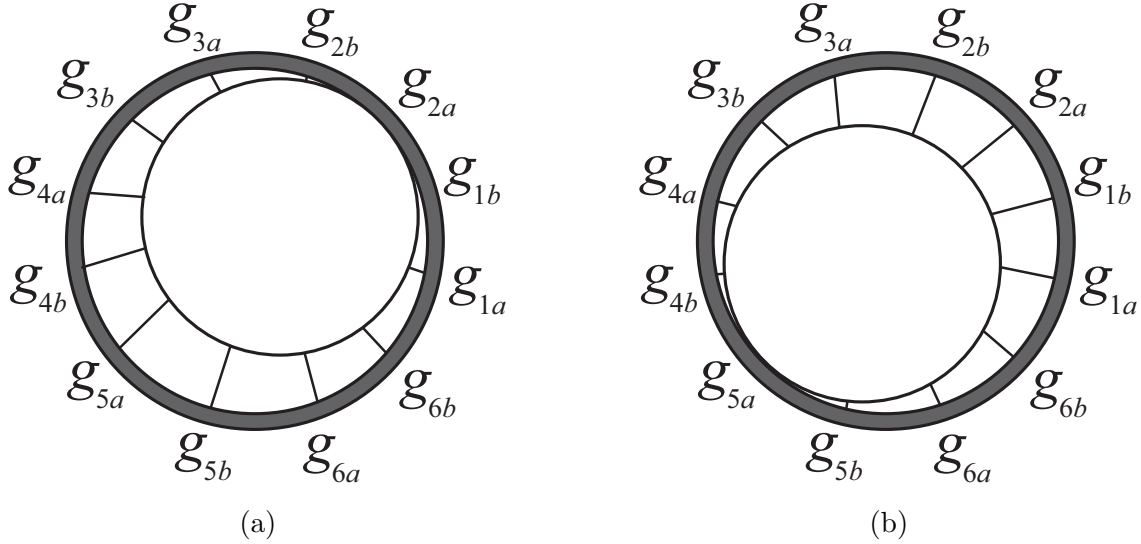


Figure 2.16. Points of interest for airgap derivation.

Fig. 2.16 shows the gaps for a single position, which are six points of interest in terms of gap measurements. The center of each tooth represents those points of interest as seen in Fig. 2.16 for two different rotor positions. Fig. 2.16(a) shows a position where $g_{2a} = 0$, while Fig. 2.16(b) shows a position where $g_{5a} = 0$. In both cases presented in Fig. 2.16 all the other gaps are not zero.

The general equation for the gaps can be then defined as:

$$g_n(\theta) = r_{21}\left[1 - \cos\left(\theta - \frac{\pi(2i - 3)}{12}\right)\right] \quad (2.23)$$

where $n = 1a, 1b, 2a, \dots, 6b$, and i goes from 1 to 12 correspondingly.

2.2.2 Magnetic Circuit

The magnetic flux enters the stator and rotor in a path that is normal to them, and with this geometric configuration, it is expected to fringe slightly. To simplify the modeling, only a path normal to the stator was considered, which is reasonable if the radius of the rotor is close to the radius of the stator ($r_1 \approx r_2$).

Fig. 2.17(a) shows the equivalent circuit of the magnetic device shown in Fig. 2.13, where \mathcal{R}_s and \mathcal{R}_r are the reluctance of the stator and rotor, respectively; \mathcal{R}_n is the reluctance of the gap n (with $n = 1a, 1b, 2a, \dots, 6b$); and F_n is the magneto-motive-force created at tooth n . The reluctance are given by:

$$\mathcal{R}_r = l_r / (\mu_r A_r) \quad (2.24)$$

$$\mathcal{R}_s = l_s / (\mu_s A_s) \quad (2.25)$$

$$\mathcal{R}_n = g_n(\theta) / (\mu_0 A_s) \quad (2.26)$$

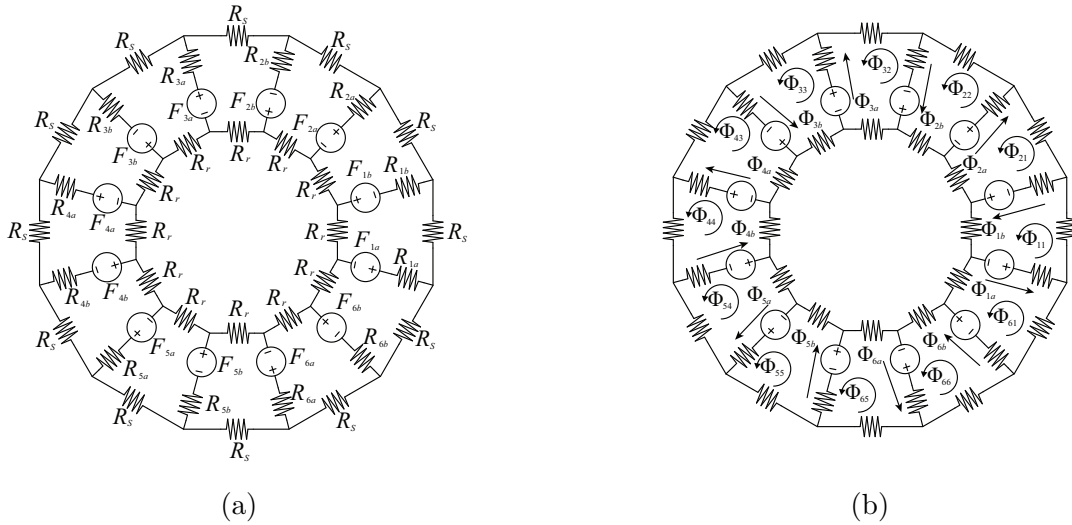


Figure 2.17. (a) Equivalent circuit of the magnetic device. (b) Equivalent circuit used for mesh analysis.

where μ_r is the permeability of the rotor, μ_s is the permeability of the stator, l_r is the length of the flux path in the rotor as shown in Fig. 2.13(a), A_r is the cross-sectional area of the rotor (as seen by the flux lines), A_s is the cross-sectional area of the stator (as seen by the flux lines), l_s is the length of the flux path in the stator, μ_0 is the permeability of air.

Fig. 2.17(b) shows the equivalent circuit of Fig. 2.17(a) with virtual fluxes $\phi_{11}, \phi_{21}, \phi_{22}, \phi_{32}, \phi_{33}, \phi_{43}, \phi_{44}, \phi_{54}, \phi_{55}, \phi_{65}, \phi_{66}$, and ϕ_{61} used for the mesh analysis, with:

$$\begin{pmatrix} \phi_{1a} \\ \phi_{1b} \\ \phi_{2a} \\ \phi_{2b} \\ \phi_{3a} \\ \phi_{3b} \\ \phi_{4a} \\ \phi_{4b} \\ \phi_{5a} \\ \phi_{5b} \\ \phi_{6a} \\ \phi_{6b} \end{pmatrix} = \begin{pmatrix} 1 & 0 & 0 & 0 & 0 & 0 & 0 & 0 & 0 & 0 & 0 & -1 \\ 1 & -1 & 0 & 0 & 0 & 0 & 0 & 0 & 0 & 0 & 0 & 0 \\ 0 & -1 & 1 & 0 & 0 & 0 & 0 & 0 & 0 & 0 & 0 & 0 \\ 0 & 0 & 1 & -1 & 0 & 0 & 0 & 0 & 0 & 0 & 0 & 0 \\ 0 & 0 & 0 & -1 & 1 & 0 & 0 & 0 & 0 & 0 & 0 & 0 \\ 0 & 0 & 0 & 0 & 1 & -1 & 0 & 0 & 0 & 0 & 0 & 0 \\ 0 & 0 & 0 & 0 & 0 & -1 & 1 & 0 & 0 & 0 & 0 & 0 \\ 0 & 0 & 0 & 0 & 0 & 0 & 1 & -1 & 0 & 0 & 0 & 0 \\ 0 & 0 & 0 & 0 & 0 & 0 & 0 & -1 & 1 & 0 & 0 & 0 \\ 0 & 0 & 0 & 0 & 0 & 0 & 0 & 0 & 1 & -1 & 0 & 0 \\ 0 & 0 & 0 & 0 & 0 & 0 & 0 & 0 & 0 & -1 & 1 & 0 \\ 0 & 0 & 0 & 0 & 0 & 0 & 0 & 0 & 0 & 0 & 1 & -1 \end{pmatrix} \begin{pmatrix} \phi_{11} \\ \phi_{21} \\ \phi_{22} \\ \phi_{32} \\ \phi_{33} \\ \phi_{43} \\ \phi_{44} \\ \phi_{54} \\ \phi_{55} \\ \phi_{65} \\ \phi_{66} \\ \phi_{61} \end{pmatrix}$$

The magneto-motive-force (MMF) for the first mesh can be described as:

$$F_{11} = \mathcal{R}_{11ab}\phi_{11} - \mathcal{R}_{1b}\phi_{21} - \mathcal{R}_{1a}\phi_{61} \quad (2.27)$$

where $\mathcal{R}_{11ab} = \mathcal{R}_{1a} + \mathcal{R}_{1b} + \mathcal{R}_s + \mathcal{R}_r$. The rest of the MMFs can be derived in a similar way.

2.2.3 Inductance, Energy and Torque

For simplification purposes, both self and mutual inductance can be derived assuming that the reluctance across magnetic cores are negligible with respect to the reluctance of the gaps. Therefore, Fig. 2.18(a) can be employed to calculate the self-inductance of the

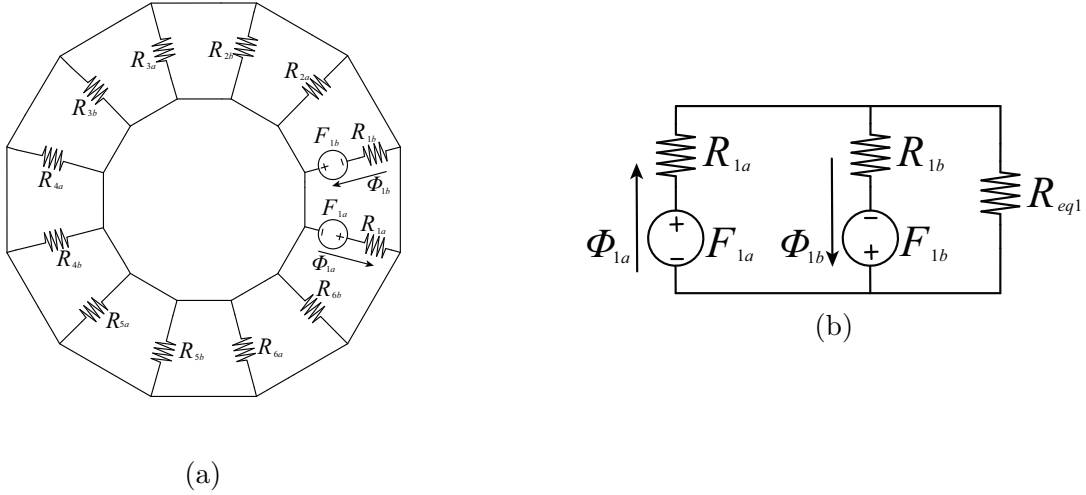


Figure 2.18. Equivalent circuits used to calculate self-inductance

winding at the tooth 1a. Fig. 2.18(b) is a simplification of Fig. 2.18(a) with $\mathcal{R}_{eq1} = \mathcal{R}_{2a} || \mathcal{R}_{2b} || \mathcal{R}_{3a} || \dots || \mathcal{R}_{6b}$. By definition $L_{1a,1a}$ is given by:

$$L_{1a,1a} = \frac{N\phi_{1a}}{i_1} = \frac{N^2}{\mathcal{R}_{1a} + \mathcal{R}_{1b} || (\mathcal{R}_{eq1})} \quad (2.28)$$

The flux linkage at tooth 1a due to a current flowing at tooth 1b constitutes a mutual flux, which happens to be the same as the self-inductance, i.e., $L_{1a,1b} = L_{1a,1a}$. All the others mutual inductance related to tooth 1a ($L_{1a,1b}$, $L_{1a,2a}$, $L_{1a,2b}$, ..., $L_{1a,6b}$) can be calculated similarly. For instance, the mutual inductance $L_{1a,2a}$ is calculated with the equivalent circuit shown in Fig. 2.19 with $\mathcal{R}_{eq2} = \mathcal{R}_{1b} || \mathcal{R}_{3a} || \mathcal{R}_{3b} || \dots || \mathcal{R}_{6b}$. In this case $L_{1a,2a}$ is the linkage flux at the tooth in 1a due to current i_2 .

The linkage fluxes are then given by:

$$\lambda_n = \sum_{j=1}^6 (L_{n,ja} + L_{n,jb}) i_j \quad (2.29)$$

where $n = 1a, 1b, 2a, \dots, 6b$.

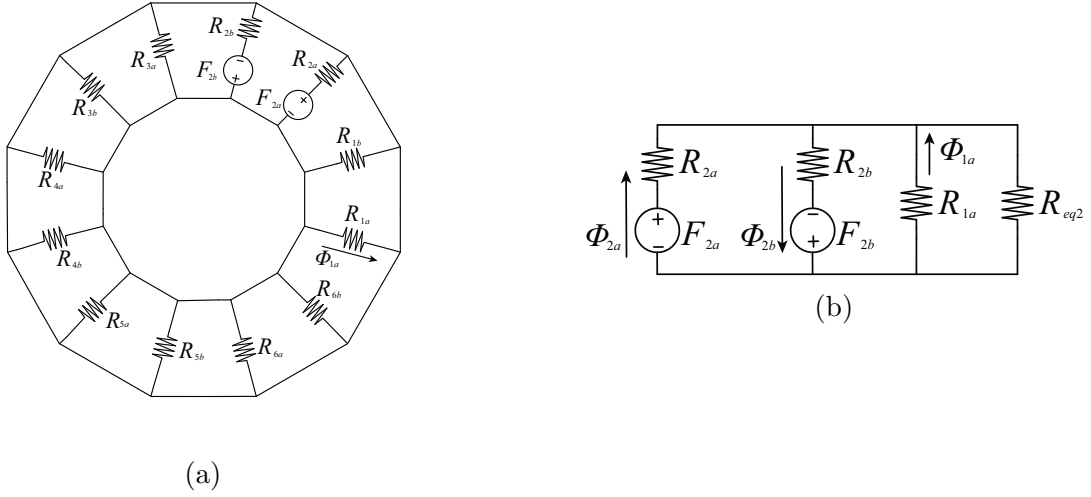


Figure 2.19. Equivalent circuits used to calculate mutual-inductance

Once the inductance are defined as mentioned, the voltage across each circuit is defined as:

$$v_j = \mathcal{R}_j i_j + \frac{d\lambda_{ja}}{dt} + \frac{d\lambda_{jb}}{dt} \quad (2.30)$$

with $j = 1, 2, \dots, 6$, and \mathcal{R}_j is the coil resistance of bipoles 1 through 6. Since the machine voltages are furnished by the drive system, the currents can be obtained from 2.30. Once the currents, fluxes, and inductance are defined, the derivative of energy can be employed to define torque.

There can be two types of voltages applied to the machine, with or without overlap of the phase voltages as shown in Fig. 2.20. The mutual inductance can be neglected when there is no overlap, as shown in Fig. 2.20(a). For further simplification, lets assume that the reluctance away from the touching point is considerably high compared to the ones close to the contact point. Therefore, the self-inductance can be simplified as following:

$$L_{ja,ja} = L_{jb,jb} = \frac{N^2}{\mathcal{R}_{ja} + \mathcal{R}_{jb}}$$

$$L_{ja,ja} = L_{jb,jb} = \frac{N^2 \mu_0 A_s}{r_{21} [2 - \frac{(\sqrt{3}+1)}{\sqrt{2}} \cos(\theta - \frac{\pi}{3}(j-1))]} \quad (2.31)$$

with $j = 1, 2, \dots, 6$.

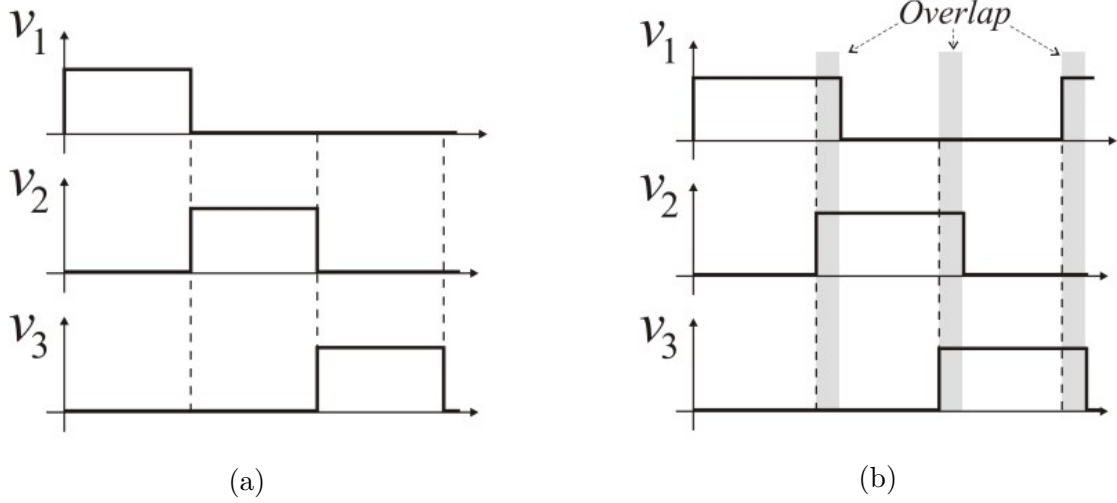


Figure 2.20. Voltage applied to the machine poles: (a) no overlap among poles, and (b) overlap among poles.

In this case the total energy and electromagnetic torque are given respectively by the following equations:

$$W_c = \sum_{j=1}^6 (L_{j a, j a} + L_{j b, j b}) i_j^2$$

$$T_e = \frac{dW_c}{d\theta} = \sum_{j=1}^6 \Delta T_j i_j^2 \quad (2.32)$$

where

$$\Delta T_j = \frac{-2\sqrt{2}N^2\mu_0 A_s(\sqrt{3} + 1) \sin(\theta - \frac{\pi}{3}(j - 1))}{r_{21}[2\sqrt{2} - (\sqrt{3} + 1) \cos(\theta - \frac{\pi}{3}(j - 1))]^2}$$

2.2.4 Mechanical Position and Speed

The physical dimensions of the stator and rotor (i.e., r_1 and r_2) will play an important role on how the mechanical speed (ω_m) is related to the electrical angular frequency (ω_e) defined by the inverter. To define how much the rotor spins in degrees when the stator excitation completes an entire cycle, consider that position 1 shown in Fig. 2.21(a) is the initial position of the rotor. After one complete electrical cycle, the rotor will be at position 2 shown in Fig. 2.21(b). From the stator point-of-view the rotor traveled an angle equal to δ .

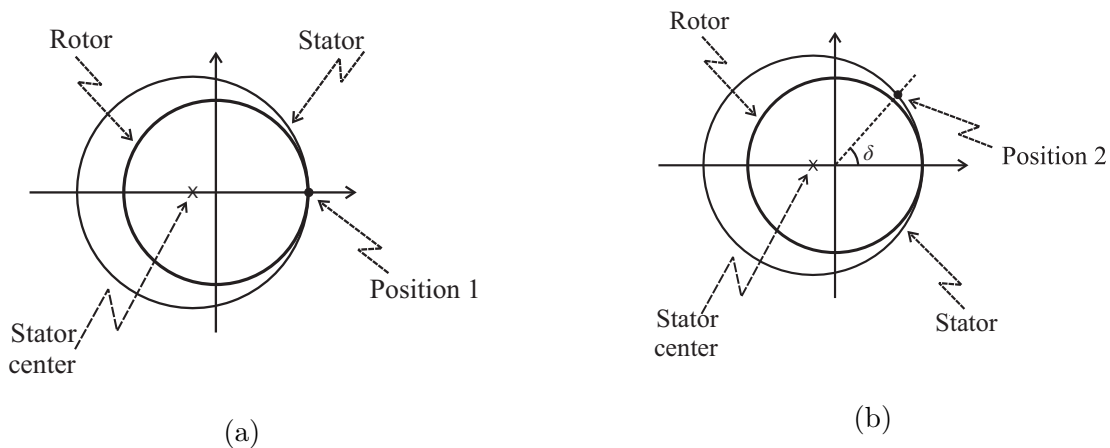


Figure 2.21. (a) Initial position of the rotor. (b) Position of the rotor after δ electrical degrees from stator point of view.

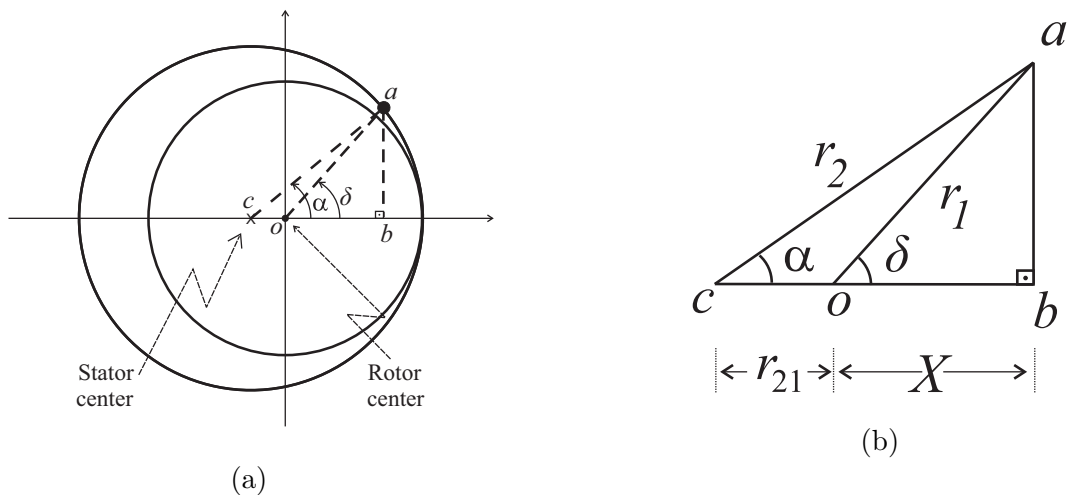


Figure 2.22. (a) Position of the rotor after an electrical cycle. (b) Geometrical approach to find angle δ .

In order to calculate this angle (δ), which can be defined as shown in Fig. 2.22(a), points c and o are defined as stator and rotor center, respectively.

In Fig. 2.22(a) the angle α can be defined as:

$$\alpha = 2\pi r_{21}/r_2 \quad (2.33)$$

To find angle δ , on the other hand, it is necessary to find the unknown X , which is the length ob . Therefore, the angle δ can be defined as:

$$\delta = \cos^{-1} \left[\frac{r_2 \cos\left(\frac{2\pi r_{21}}{r_2}\right) - r_{21}}{r_1} \right] \quad (2.34)$$

If the electrical frequency is defined as $f_e = 1/\tau_e$, the electrical speed is defined by $\omega_e = 2\pi f_e$. Note that it will take the same period of time for the rotor to travel δ radians, as it takes for one electrical cycle (τ_e), so the mechanical speed can be derived from:

$$\omega_m = \delta f_e \quad (2.35)$$

$$\omega_m = \frac{\delta}{2\pi} \omega_e \quad (2.36)$$

$$\omega_m = \cos^{-1} \left[\frac{r_2 \cos\left(\frac{2\pi r_{21}}{r_2}\right) - r_{21}}{r_1} \right] \frac{\omega_e}{2\pi} \quad (2.37)$$

The mechanical speed can be changed by either modifying the physical dimensions of the stator and rotor or by increasing the electrical frequency (ω_e). From (2.37) it is clear that ω_m increases if the radius of the rotor increases for a given stator radius.

2.2.5 Simulation and Experimental Results

MATLAB and C++ codes have been used to simulate the proposed machines with six bipoles. The parameters used in these codes are shown in Table I.

Figs. 2.23(a)-2.23(c) show simulation results for a machine with six bipoles. Those results were collected with the electrical frequency equal to 2 Hz. A proof-of-concept laboratory prototype with six magnetic bipoles was built to validate the theoretical assumptions, see Fig. 2.24. The stator in this prototype was obtained from Robbins & Myers' KP-L421BOT electric machine shown in Fig. 2.24(a), and the rotor is made of low silicon steel M4-011 which is shown in Fig. 2.24(b). The entire experimental setup for this prototype including the drive system is presented in Fig. 2.25(a). In this experimental setup, the inverter used

Table 2.1. Parameters used in the simulation

Parameter	Description	Value
B_m	Coefficient of friction	0.1
J_m	Moment of inertia	0.01 ($Kg.m^2$)
V_{dc}	DC link voltage	15 (V)
μ_0	Permeability of air	$4\pi \times 10^{-7} (H/m)$
μ_s	Relative Permeability of the stator	3000
μ_r	Relative Permeability of the rotor	1000
l_s	Length of the flux path in the stator	0.0869 (m)
l_r	Length of the flux path in the rotor	0.0283 (m)
A_s	Cross sectional area of the stator	$216 \times 10^{-6} (m^2)$
A_r	Cross sectional area of the rotor	$15 \times 10^{-5} (m^2)$
N	Number of turns in each tooth	160
r	Series resistance in each winding	3 (Ω)
R_s	Stator radius	0.04 (m)
R_r	Rotor radius	0.026 (m)
f_e	Electrical frequency	2 (Hz)

to generate the machine voltages is IRAMX20UP60A. This inverter is a 3-leg inverter, and since the proposed machine needs 6 voltages, two of these inverters have been used.

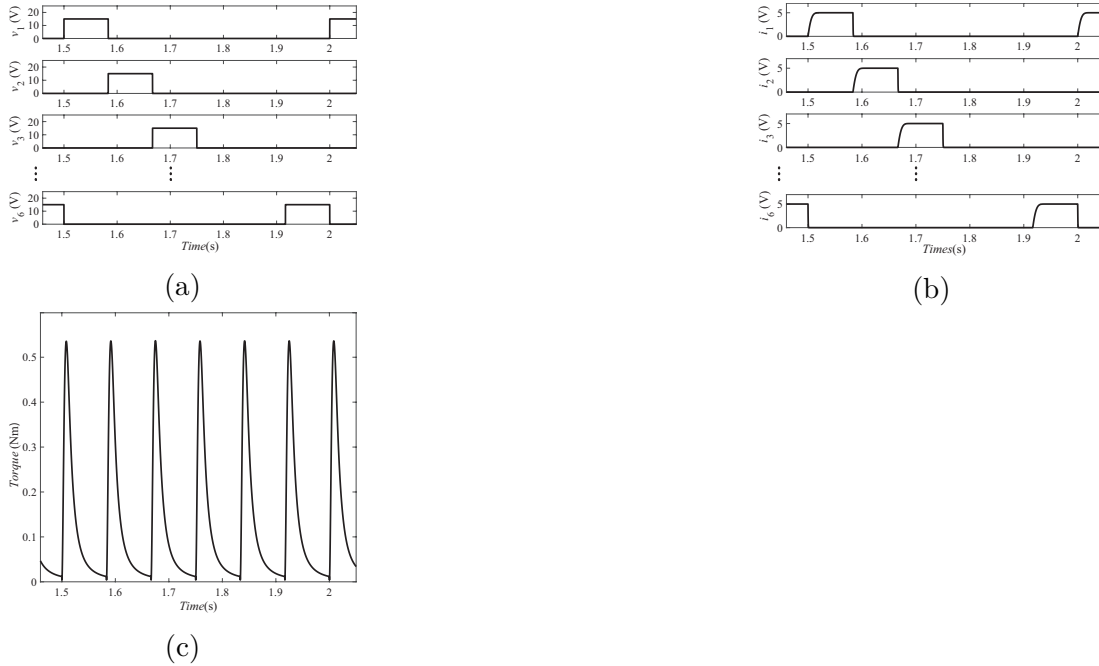


Figure 2.23. Simulation results (3 pole machine): (a) voltage, (b) current, and (c) torque.



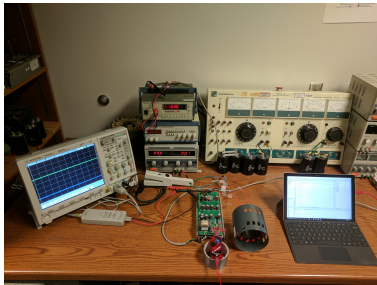
(a)



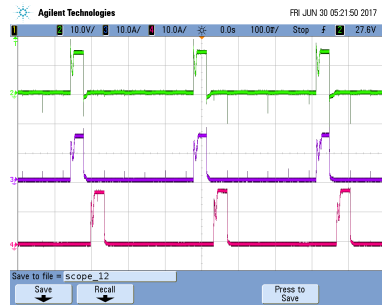
(b)

Figure 2.24. Six pole machine: (a) stator and (b) rotor.

A DC voltage of 15 V was supplied to the system through a power supply. Fig. 2.25(b) shows a phase voltage (green) with the same phase current (purple) along with an adjacent phase current (red). The proposed machine was running on an electrical frequency of 2 Hz.



(a)



(b)

Figure 2.25. (a) Experimental setup. (b) Phase voltage of a single bipole (green), current of the same phase voltage (purple), and an adjacent current (red).

3. AIRGAP-LESS ELECTRIC MACHINE WITH AN EXTERNAL ROTOR

As it has been studied in previous chapter, the more the number of poles in the airgap-less electric machine, the smoother the movement of the rotor. In this section the analysis and development of an airgap-less electric machine with eighteen teeth and nine phases has been studied. This machine has the highest torque among the previous versions of it that was presented in chapter 2 of this dissertation. Another difference that this machine has with its previous versions is that the rotor is external instead of internal and below is the reason for this selection. Electric machine designers have two options in terms of the position of the rotor and stator (internal or external). When the rotor is around the stator (external rotor), there will be larger area available for stator slots which will result in decreasing flux leakage and consequently decreasing the losses of the machine [90]. Other benefits of the external rotor include: (1) a more constant speed profile while the machine is operating under various load conditions [91]; (2) lighter in weight and less manufacturing complexity [92]-[93]; (3) desirable for in-wheel automotive applications due to their high-torque density, low rotating inertia and drive stiffness [94]-[95]. Furthermore, it has been shown that the torque is influenced by the split ratio (ratio of airgap diameter to the outer diameter) which can be increased by having an external rotor instead of the internal rotor [96]-[97].

3.1 Airgap-less Machine Operating Principle

As it has been presented below, this machine has eighteen teeth with nine phases with an external rotor. For simplicity of the analysis for the reader, I have presented mathematical analysis of the bipole configuration along with external rotor for three bipole machine and four bipole machine. The simulation of these machines are compared to those of the nine phase airgap-less electric machine. The complete analysis of the eighteen teeth nine phase airgap-less electric machine has been shown in the c code in appendix A.

3.2 Three Bipole Machine

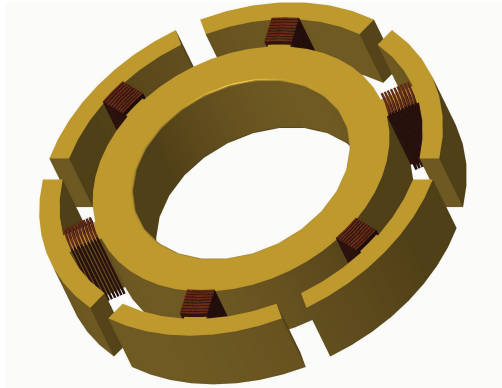
As mentioned before, the proposed family of machines use physical contact between the stator and rotor to maximize force and rotational torque. Since the rotor will roll over the stator surface, the minimum number of magnetic bipoles to implement the proposed airgap-less machine is three. Notice that with two bipoles, the machine will not be able to startup following a desirable direction.

3.2.1 Conception and Operation

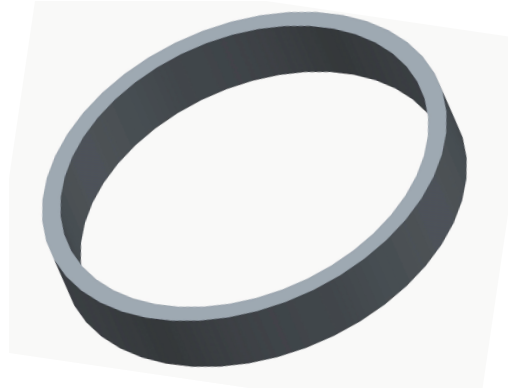
Fig. 3.1 presents different views of a 3D sketch of the proposed machine. Fig. 3.1(a) shows the stator with 3 bipoles (six teeth), Fig. 3.1(b) presents the rotor. Fig. 3.1(c) and Fig. 3.1(d) highlight both stator and rotor and how the rotor is allowed to touch the stator. The former shows a view in perspective while the latter depicts a top view.

This machine will be excited with a magnetic bipole configuration as shown in Fig. 3.2(a). Two teeth form a pole pair, where one of the teeth is north while the other one is south emulating a C-core configuration. The continuous rotor movement is obtained by exciting these poles with a machine drive system as presented in Fig. 3.2(b). Fig. 3.3, in turn, shows a sequence of snap shots (top view) that demonstrate how the proposed machine operates, i.e., the rotor touches different positions of the stator as the excitation goes from pole 1 to pole 3 in a counter-clockwise direction.

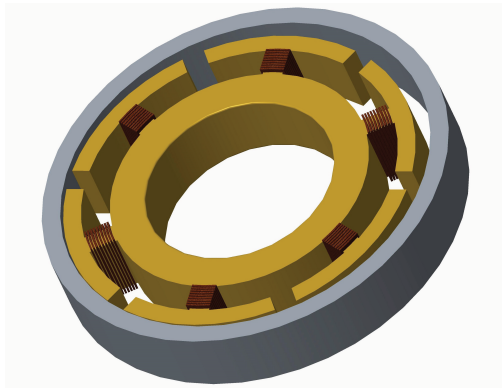
It is noteworthy to mention that the rotation created by this machine is similar to that of hydraulic machines [98], as seen in Fig. 3.4. Both types of machines (the proposed airgap-less electric machine and the hydraulic machine) have a rigid body rotor with combined translational and rotational movements. A mechanical gear can be used to convert this combined translational and rotational movement into a rotational movement only, if necessary for a specific application. This type of gear box has been used in hydraulic machines and it is a firmly established technology.



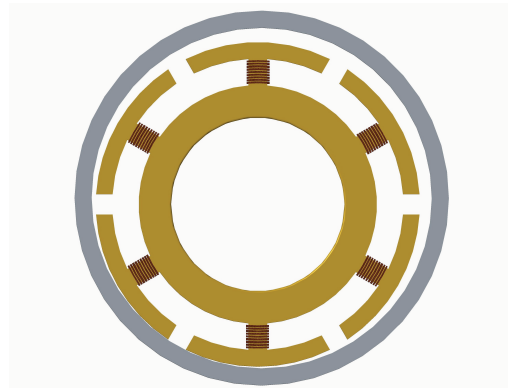
(a)



(b)



(c)



(d)

Figure 3.1. Three-dimensional views of the proposed three-bipole machine. (a) Stator, (b) rotor, (c) stator-rotor in perspective, and (d) stator-rotor top view.

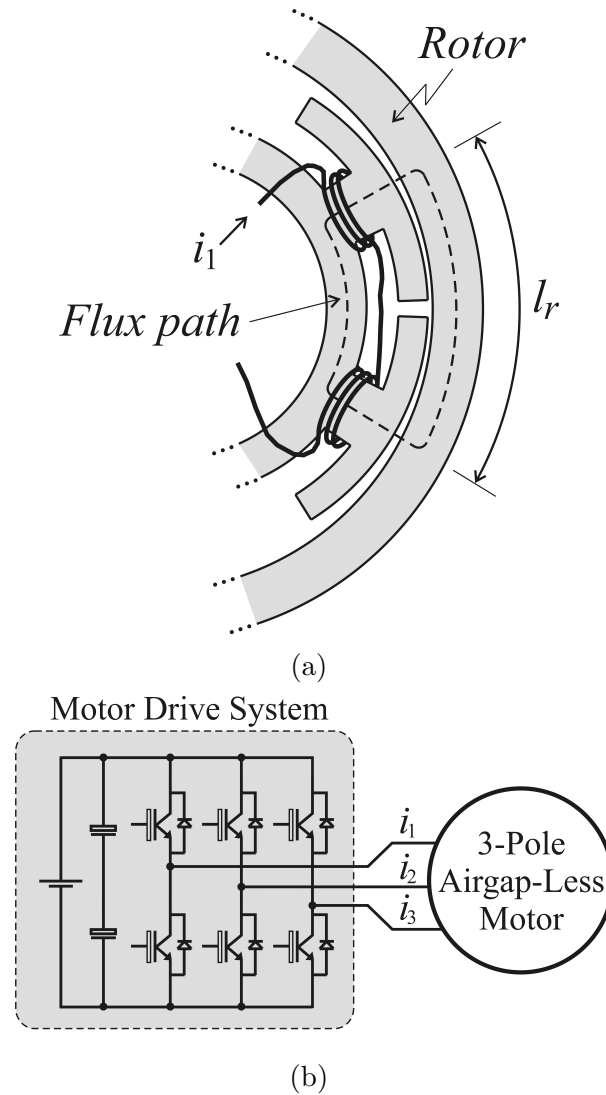


Figure 3.2. (a) Bipole configuration. (b) machine drive system.

3.2.2 Airgap Modeling

As the rotor spins following the stator pole excitation, its center spans a circle. Due to this movement, the gap between the stator and rotor changes as a function of the angular position of the rotor (θ). θ is the angle of the touching point between rotor and stator, as shown in Fig. 3.5. Notice from this figure that r_1 (radius of the stator) and r_2 (radius of the rotor) were made small and large (respectively) to facilitate the visualization.

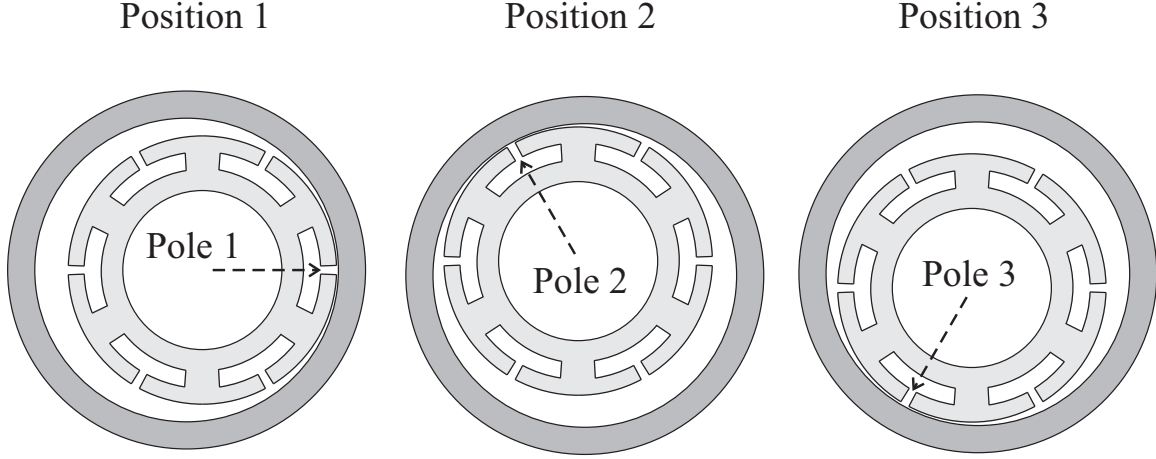


Figure 3.3. Sequence of shots showing a continuous rotor movement.

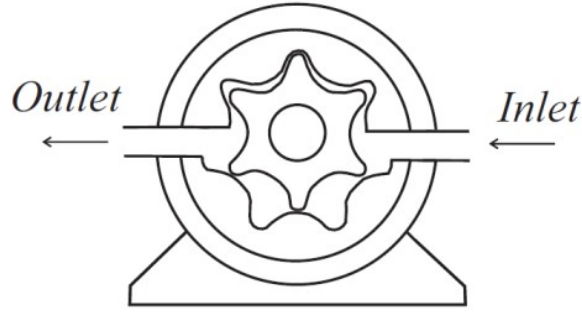


Figure 3.4. Hydraulic machine.

Fig. 3.5(b) shows how the gap at position 1 (i.e., seen by the center of the bipole 1) can be written as a function of the angle θ . The expression for the gap can therefore be derived as shown below:

$$g(\theta) = r_2 - r_{21}\cos(\theta) - \sqrt{r_1^2 - r_{21}^2\sin^2(\theta)} \quad (3.1)$$

where r_{21} is the difference between both radii (i.e., $r_{21} = r_2 - r_1$). In this design the radius of the rotor and stator are close to each other, i.e. $r_1 \approx r_2$. Therefore, the gap expression can be simplified as:

$$g(\theta) = r_{21}[1 - \cos(\theta)] \quad (3.2)$$

Although Fig. 3.6 shows the gap for a single position, there are six points of interest in terms of gap measurements. The center of each tooth represents those points of interest as seen in

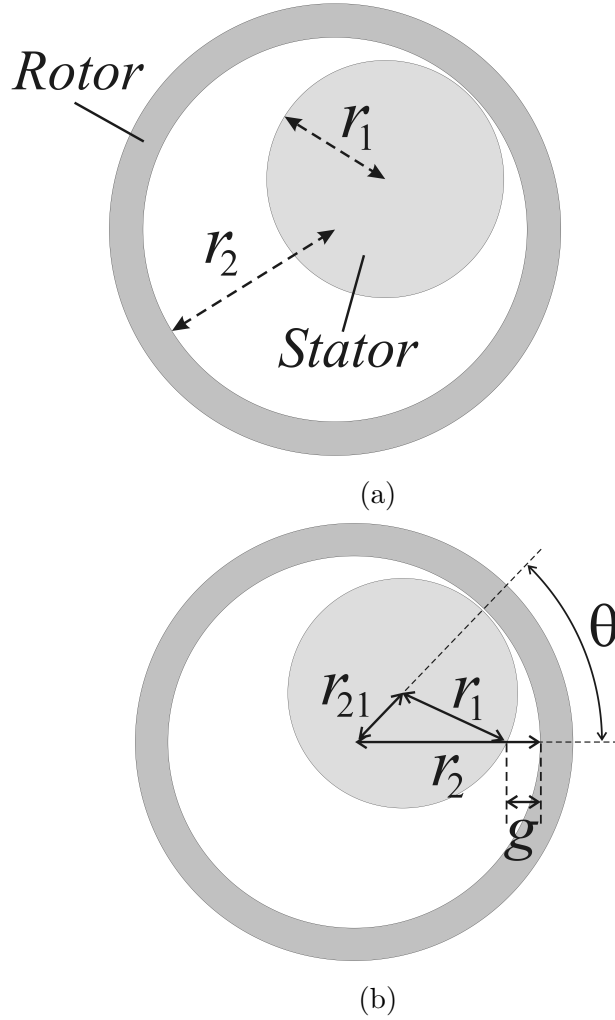
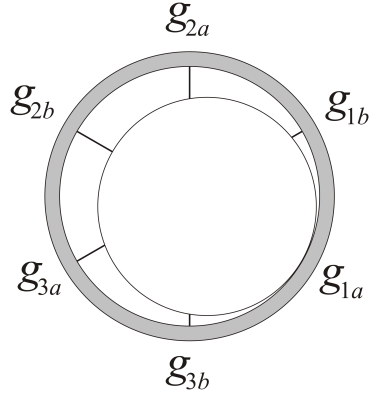


Figure 3.5. Geometric approach used for airgap derivation.

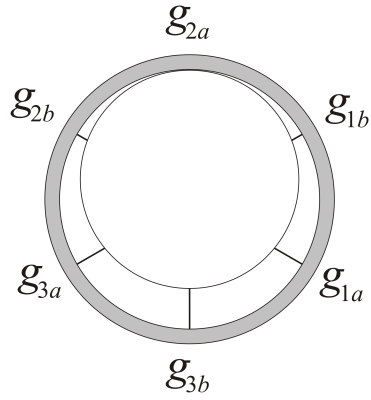
Fig. 3.6 for two different rotor positions. Fig. 6(a) shows a position where $g_{1a} = 0$, while Fig. 3.6(b) shows a position where $g_{2a} = 0$. In both cases presented in Fig. 3.6, all the other gaps are different from zero. The gaps at the interest points can be derived as following:

$$g_{1a}(\theta) = r_{21}[1 - \cos(\theta - \pi/6)] \quad (3.3)$$

$$g_{1b}(\theta) = r_{21}[1 - \cos(\theta + \pi/6)] \quad (3.4)$$



(a)



(b)

Figure 3.6. Points of interest for airgap derivation.

$$g_{2a}(\theta) = r_{21}[1 - \cos(\theta + 3\pi/6)] \quad (3.5)$$

$$g_{2b}(\theta) = r_{21}[1 - \cos(\theta + 5\pi/6)] \quad (3.6)$$

$$g_{3a}(\theta) = r_{21}[1 - \cos(\theta + 7\pi/6)] \quad (3.7)$$

$$g_{3b}(\theta) = r_{21}[1 - \cos(\theta + 9\pi/6)] \quad (3.8)$$

3.2.3 Magnetic Circuit

The magnetic flux travels in a path that is normal to both the stator and the rotor, and with this geometric configuration, it is expected to fringe slightly. To simplify the modeling, only a path normal to the stator was considered, which is reasonable if the radius of the rotor is close to the radius of the stator ($r_1 \approx r_2$).

Fig. 3.7(a) shows the equivalent circuit of the magnetic device shown in Fig. 3.1, where \mathfrak{R}_s and \mathfrak{R}_r are the reluctances of the stator and rotor, respectively; \mathfrak{R}_y is the reluctance of the gap y (with $y = 1a, 1b, 2a, 2b, 3a, 3b$); and \mathfrak{F}_y is the magneto-motive-force created at tooth y . The reluctances are given by:

$$\mathfrak{R}_r = l_r / (\mu_r A_r) \quad (3.9)$$

$$\mathfrak{R}_s = l_s / (\mu_s A_s) \quad (3.10)$$

$$\mathfrak{R}_{1a} = g_{1a}(\theta) / (\mu_0 A_s) \quad (3.11)$$

$$\mathfrak{R}_{1b} = g_{1b}(\theta) / (\mu_0 A_s) \quad (3.12)$$

$$\mathfrak{R}_{2a} = g_{2a}(\theta) / (\mu_0 A_s) \quad (3.13)$$

$$\mathfrak{R}_{2b} = g_{2b}(\theta) / (\mu_0 A_s) \quad (3.14)$$

$$\mathfrak{R}_{3a} = g_{3a}(\theta) / (\mu_0 A_s) \quad (3.15)$$

$$\mathfrak{R}_{3b} = g_{3b}(\theta) / (\mu_0 A_s) \quad (3.16)$$

where μ_r is the permeability of the rotor, μ_s is the permeability of the stator, l_r is the length of the flux path in the rotor as shown in Fig. 3.2(a), A_r is the surface area of the rotor (seen by the flux lines), l_s is the length of the flux path in the stator, μ_0 is the permeability of air. Fig. 3.7(b) shows the equivalent circuit of Fig. 7(a) with virtual fluxes $\phi_{11}, \phi_{22}, \phi_{33}, \phi_{31}, \phi_{21}$, and ϕ_{32} used for the mesh analysis, with:

$$\begin{bmatrix} \phi_{1a} \\ \phi_{1b} \\ \phi_{2a} \\ \phi_{2b} \\ \phi_{3a} \\ \phi_{3b} \end{bmatrix} = \begin{bmatrix} 1 & 0 & 0 & -1 & 0 & 0 \\ 1 & 0 & 0 & 0 & -1 & 0 \\ 0 & 1 & 0 & 0 & -1 & 0 \\ 0 & 1 & 0 & 0 & 0 & -1 \\ 0 & 0 & 1 & 0 & 0 & -1 \\ 0 & 0 & 1 & -1 & 0 & 0 \end{bmatrix} \begin{bmatrix} \phi_{11} \\ \phi_{22} \\ \phi_{33} \\ \phi_{31} \\ \phi_{21} \\ \phi_{32} \end{bmatrix} \quad (3.17)$$

The relationship between magneto-motive-forces and fluxes can be derived as following:

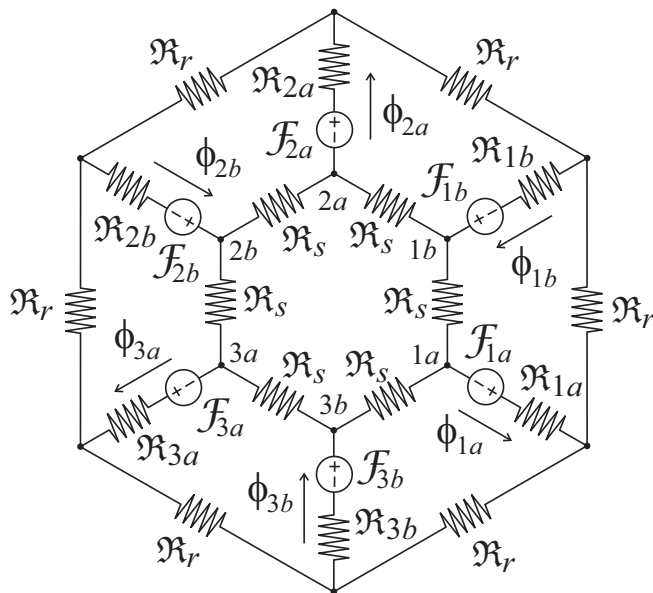
$$\begin{bmatrix} \mathcal{F}_{11} \\ \mathcal{F}_{12} \\ \mathcal{F}_{22} \\ \mathcal{F}_{23} \\ \mathcal{F}_{33} \\ \mathcal{F}_{31} \end{bmatrix} = \begin{bmatrix} \mathfrak{R}_{11ab} & 0 & 0 & -\mathfrak{R}_{1a} & -\mathfrak{R}_{1b} & 0 \\ \mathfrak{R}_{1b} & \mathfrak{R}_{2a} & 0 & 0 & \mathfrak{R}_{12ab} & 0 \\ 0 & \mathfrak{R}_{22ab} & 0 & 0 & -\mathfrak{R}_{2a} & -\mathfrak{R}_{2b} \\ 0 & \mathfrak{R}_{2b} & \mathfrak{R}_{3a} & 0 & 0 & \mathfrak{R}_{23ba} \\ 0 & 0 & \mathfrak{R}_{33ab} & -\mathfrak{R}_{3b} & 0 & -\mathfrak{R}_{3a} \\ \mathfrak{R}_{1a} & 0 & \mathfrak{R}_{3b} & \mathfrak{R}_{31ba} & 0 & 0 \end{bmatrix} \begin{bmatrix} \phi_{11} \\ \phi_{22} \\ \phi_{33} \\ \phi_{31} \\ \phi_{21} \\ \phi_{32} \end{bmatrix}$$

where: $\mathfrak{R}_{11ab} = \mathfrak{R}_{1a} + \mathfrak{R}_r + \mathfrak{R}_{1b} + \mathfrak{R}_s$; $\mathfrak{R}_{12ba} = -(\mathfrak{R}_{1b} + \mathfrak{R}_r + \mathfrak{R}_{2a} + \mathfrak{R}_s)$; $\mathfrak{R}_{22ab} = (\mathfrak{R}_{2a} + \mathfrak{R}_r + \mathfrak{R}_{2b} + \mathfrak{R}_s)$; $\mathfrak{R}_{23ba} = -(\mathfrak{R}_{2b} + \mathfrak{R}_r + \mathfrak{R}_{3a} + \mathfrak{R}_s)$; $\mathfrak{R}_{33ab} = (\mathfrak{R}_{3a} + \mathfrak{R}_r + \mathfrak{R}_{3b} + \mathfrak{R}_s)$ $\mathfrak{R}_{31ba} = -(\mathfrak{R}_{3b} + \mathfrak{R}_r + \mathfrak{R}_{1a} + \mathfrak{R}_s)$; $\mathcal{F}_{11} = \mathcal{F}_{1a} + \mathcal{F}_{1b} = 2Ni_1$; $\mathcal{F}_{12} = \mathcal{F}_{1b} + \mathcal{F}_{2a} = N(i_1 + i_2)$; $\mathcal{F}_{22} = \mathcal{F}_{2a} + \mathcal{F}_{2b} = 2Ni_2$; $\mathcal{F}_{23} = \mathcal{F}_{2b} + \mathcal{F}_{3a} = N(i_2 + i_3)$; $\mathcal{F}_{33} = \mathcal{F}_{3a} + \mathcal{F}_{3b} = 2Ni_3$; $\mathcal{F}_{31} = \mathcal{F}_{3b} + \mathcal{F}_{1a} = N(i_3 + i_1)$;

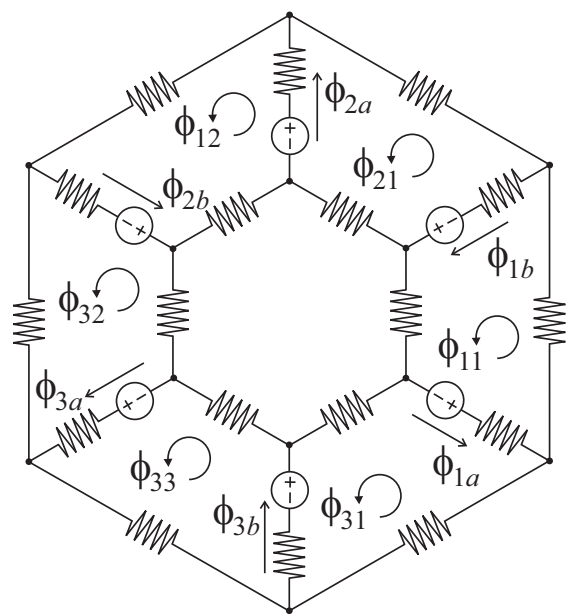
with N being the number of turns in each tooth.

3.2.4 Inductances, Energy, and Torque

For simplification purposes both self and mutual inductances can be derived assuming that the reluctances across magnetic cores are negligible with respect to the reluctances



(a)



(b)

Figure 3.7. (a) Equivalent circuit of the magnetic device. (b) Equivalent circuit used for mesh analysis.

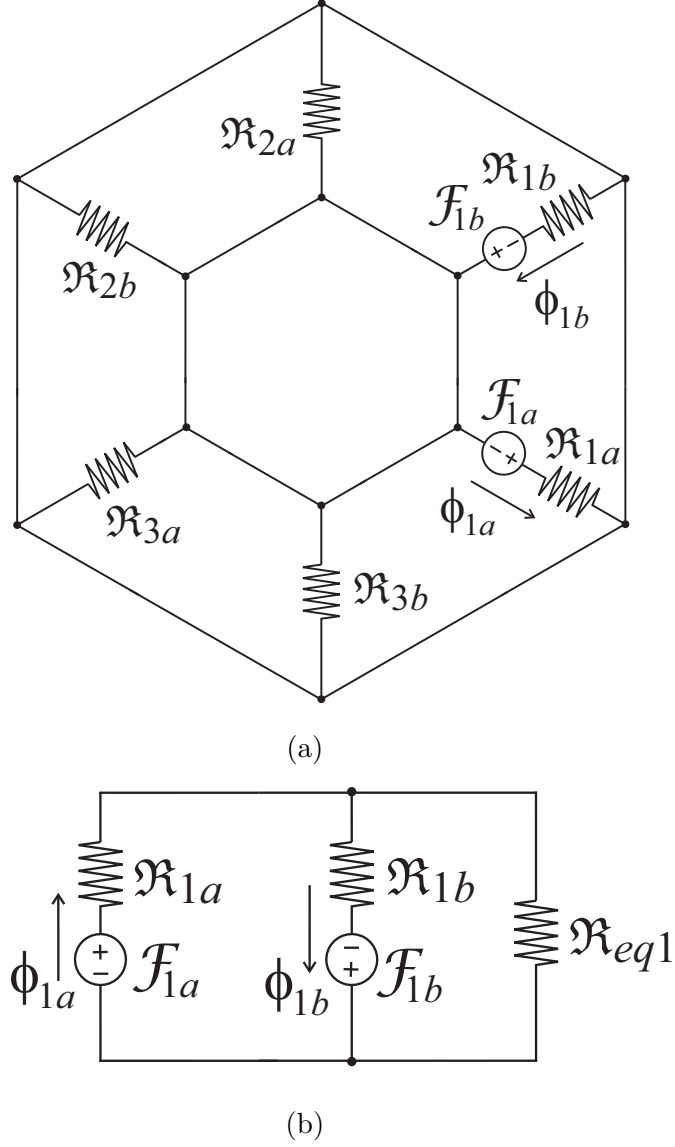


Figure 3.8. Equivalent circuits used to calculate self-inductance.

of the gaps. Therefore, Fig. 3.8(a) can be employed to calculate the self-inductance of the winding at the tooth 1a. Fig. 3.8(b) is a simplification of Fig. 3.8(a) with $\mathfrak{R}_{eq1} = \mathfrak{R}_{2a} // \mathfrak{R}_{2b} // \mathfrak{R}_{3a} // \mathfrak{R}_{3b}$. By definition L_{1a1a} is given by:

$$L_{1a1a} = \frac{N \Phi_{1a}}{i_1} = \frac{N^2}{\mathfrak{R}_{1a} + \mathfrak{R}_{1b} // (\mathfrak{R}_{eq1})} \quad (3.18)$$

The flux linkage at tooth $1a$ due to a current flowing at tooth $1b$ constitutes a mutual flux, which happens to be the same as the self-inductance, i.e., $L_{1a1b} = L_{1a1a}$. All the others mutual inductances related to tooth $1a$ ($L_{1a1b}, L_{1a2a}, L_{1a2b}, L_{1a3a}$, and L_{1a3b}) can be calculated similarly. For instance, the mutual inductance L_{1a2a} is calculated with the equivalent circuit shown in Fig. 3.9 with $\mathfrak{R}_{eq2} = \mathfrak{R}_{1b} // \mathfrak{R}_{3a} // \mathfrak{R}_{3b}$. In this case L_{1a2a} is the linkage flux at the tooth in $1a$ due to current i_2 .

The linkage fluxes are given by:

$$\lambda_{1a} = (L_{1a1a} + L_{1a1b})i_1 + (L_{1a2a} + L_{1a2b})i_2 + (L_{1a3a} + L_{1a3b})i_3$$

$$\lambda_{1b} = (L_{1b1a} + L_{1b1b})i_1 + (L_{1b2a} + L_{1b2b})i_2 + (L_{1b3a} + L_{1b3b})i_3$$

$$\lambda_{2a} = (L_{2a1a} + L_{2a1b})i_1 + (L_{2a2a} + L_{2a2b})i_2 + (L_{2a3a} + L_{2a3b})i_3$$

$$\lambda_{2b} = (L_{2b1a} + L_{2b1b})i_1 + (L_{2b2a} + L_{2b2b})i_2 + (L_{2b3a} + L_{2b3b})i_3$$

$$\lambda_{3a} = (L_{3a1a} + L_{3a1b})i_1 + (L_{3a2a} + L_{3a2b})i_2 + (L_{3a3a} + L_{3a3b})i_3$$

$$\lambda_{3b} = (L_{3b1a} + L_{3b1b})i_1 + (L_{3b2a} + L_{3b2b})i_2 + (L_{3b3a} + L_{3b3b})i_3$$

Once the inductances are defined, the voltage across each circuit is defined as:

$$v_1 = r_1 i_1 + \frac{d\lambda_{1a}}{dt} + \frac{d\lambda_{1b}}{dt} \quad (3.19)$$

$$v_2 = r_2 i_2 + \frac{d\lambda_{2a}}{dt} + \frac{d\lambda_{2b}}{dt} \quad (3.20)$$

$$v_3 = r_3 i_3 + \frac{d\lambda_{3a}}{dt} + \frac{d\lambda_{3b}}{dt} \quad (3.21)$$

where r_1 , r_2 , and r_3 are the coil resistances of poles 1, 2, and 3, respectively. Since the machine voltages are furnished by the drive system, the currents can be obtained from (3.19)-(3.21). Once the currents, fluxes, and inductance are defined, the derivative of energy can be employed to define torque.

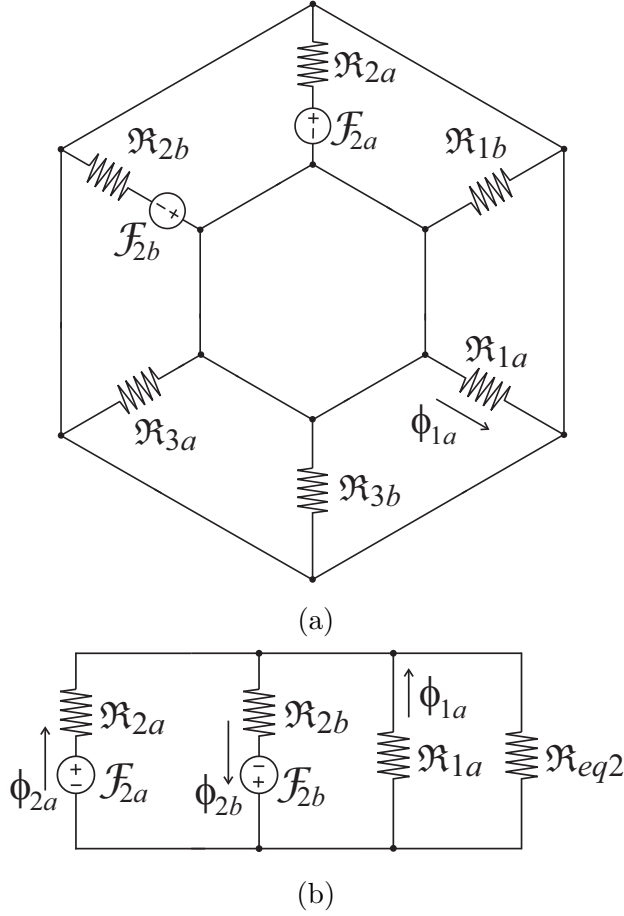


Figure 3.9. Equivalent circuits used to calculate mutual-inductance.

If there are two types of voltages applied to the machine, i.e., with and without overlap as shown in Fig. 3.10, the mutual inductance can be neglected when there is no overlap [see Fig. 3.10(a)]. For further simplification, let's assume that the reluctance away from the touching point is considerably high compared to the ones close to the contact point. Therefore, the self-inductances can be simplified as following:

$$L_{1a1a} = L_{1b1b} = \frac{N^2}{\mathfrak{R}_{1a} + \mathfrak{R}_{1b}} = \frac{N^2 \mu_0 A_s}{r_{21} [2 - \sqrt{3} \cos(\theta)]} \quad (3.22)$$

$$L_{2a2a} = L_{2b2b} = \frac{N^2}{\mathfrak{R}_{2a} + \mathfrak{R}_{2b}} = \frac{N^2 \mu_0 A_s}{r_{21} [2 - \sqrt{3} \cos(\theta - 2\pi/3)]} \quad (3.23)$$

$$L_{3a3a} = L_{3b3b} = \frac{N^2}{\mathfrak{R}_{3a} + \mathfrak{R}_{3b}} = \frac{N^2 \mu_0 A_s}{r_{21} [2 - \sqrt{3} \cos(\theta + 2\pi/3)]} \quad (3.24)$$

In this case, the total energy and electromagnetic torque are given respectively by the following equations:

$$W_c = (L_{1a1a} + L_{1b1b})i_1^2 + (L_{2a2a} + L_{2b2b})i_2^2 + (L_{3a3a} + L_{3b3b})i_3^2$$

$$T_e = \frac{dw_c}{d\theta} = \Delta T_1 i_1^2 + \Delta T_2 i_2^2 + \Delta T_3 i_3^2 \quad (3.25)$$

where

$$\Delta T_1 = -\frac{2\sqrt{3}r_{21}\sin\theta N^2 \mu_0 A_s}{(2r_{21} - r_{21}\sqrt{3}\cos(\theta))^2}$$

$$\Delta T_2 = -\frac{2\sqrt{3}r_{21}\sin(\theta - \frac{2\pi}{3}) N^2 \mu_0 A_s}{(2r_{21} - r_{21}\sqrt{3}\cos(\theta - \frac{2\pi}{3}))^2}$$

$$\Delta T_3 = -\frac{2\sqrt{3}r_{21}\sin(\theta + \frac{2\pi}{3}) N^2 \mu_0 A_s}{(2r_{21} - r_{21}\sqrt{3}\cos(\theta + \frac{2\pi}{3}))^2}$$

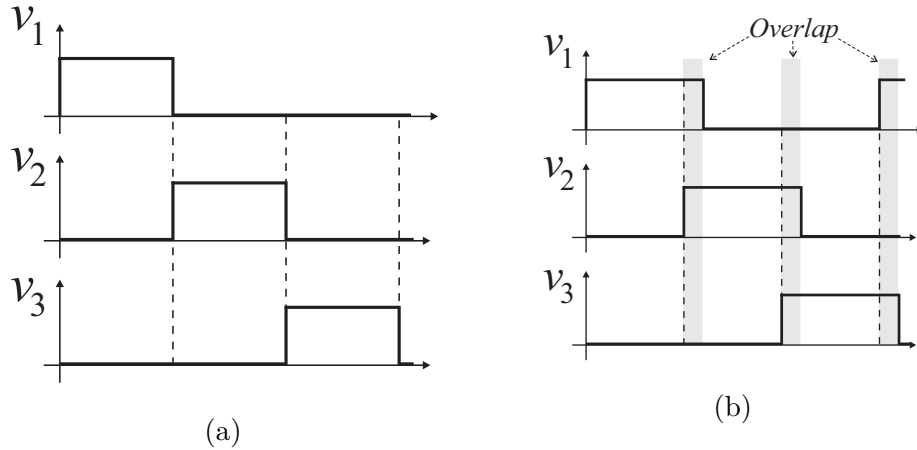


Figure 3.10. Voltage applied to the machine poles: (a) no overlap among poles, and (b) overlap among poles.

3.2.5 Mechanical Analysis

Position and Speed

The physical dimensions of the stator and rotor (i.e., r_1 and r_2) will play an important role on how the mechanical speed (ω_m) is related to the electrical angular frequency (ω_e) defined by the inverter. To define how much the rotor spins in degrees when the stator excitation completes an entire cycle, consider that position 1 shown in Fig. 3.11(a) is the initial position of the rotor. After one complete electrical cycle, the rotor will be at position 2 shown in Fig. 3.11(b). From the stator point-of-view the rotor traveled an angle equal to δ .

In order to calculate this angle (δ), shown in Fig. 3.11(b), points c and o are defined as rotor center and stator center, respectively.

In Fig. 12(a) the angle α can be defined as:

$$\alpha = 2\pi r_{21}/r_2 \quad (3.26)$$

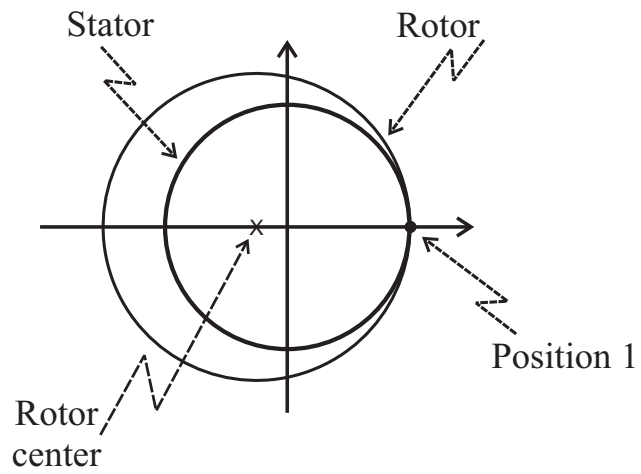
To find angle δ , on the other hand, it is necessary to find the unknown X , which is the length ob . Therefore, the angle δ can be defined as:

$$\delta = \cos^{-1}\left[\frac{r_2 \cos\left(\frac{2\pi r_{21}}{r_2}\right) - r_{21}}{r_1}\right] \quad (3.27)$$

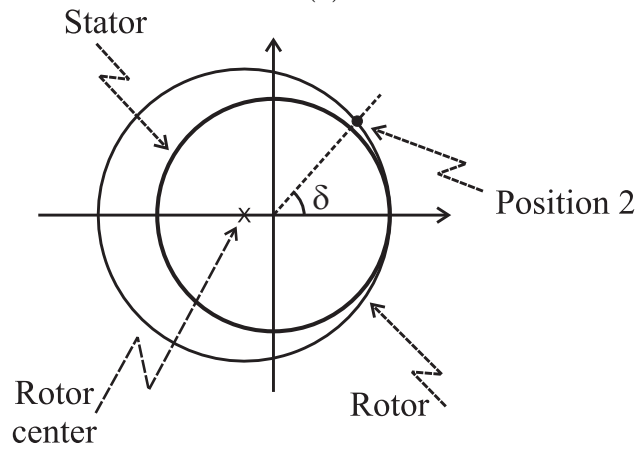
If the electrical frequency is defined as $f_e = 1/\tau_e$, the electrical speed is defined by $\omega_e = 2\pi f_e$. Note that it will take the same period of time for the rotor to travel δ radians, as it takes for one electrical cycle (τ_e), so the mechanical speed can be derived from:

$$\omega_m = \delta f_e \quad (3.28)$$

$$\omega_m = \frac{\delta}{2\pi} \omega_e \quad (3.29)$$



(a)



(b)

Figure 3.11. (a) Initial position of the rotor. (b) Position of the rotor after δ electrical degrees from stator point of view.

$$\omega_m = \cos^{-1} \left[\frac{r_2 \cos \left(\frac{2\pi r_{21}}{r_2} \right) - r_{21}}{r_1} \right] \frac{\omega_e}{2\pi} \quad (3.30)$$

The mechanical speed can be changed by either modifying the physical dimensions of the stator and rotor or by increasing the electrical frequency (f_e). From (3.30), it is clear that ω_m increases if the radius of the rotor increases for a given stator radius.

Static Force Vector Analysis

Fig. 3.12 shows the static forces acting on stator and rotor when the contact point is some degrees apart from the excitation. When that stator pole is excited, the rotor will be attracted to that point with the electromagnetic force F_1 , which has two components, the tangential component F_{1a} and the normal component F_{1b} . Notice that F_{1b} is a rotor force acting on the stator, so the stator will react with equal and opposite force. Since F_{1a} is acting in the rotor, it applies the same force (force of friction) on the stator at the point of contact. Assuming that there is no slip, the stator applies an equal and opposite force on the rotor, which is the tangential force on the rotor as shown in Fig. 3.12. This tangential force causes the rotational torque on the rotor.

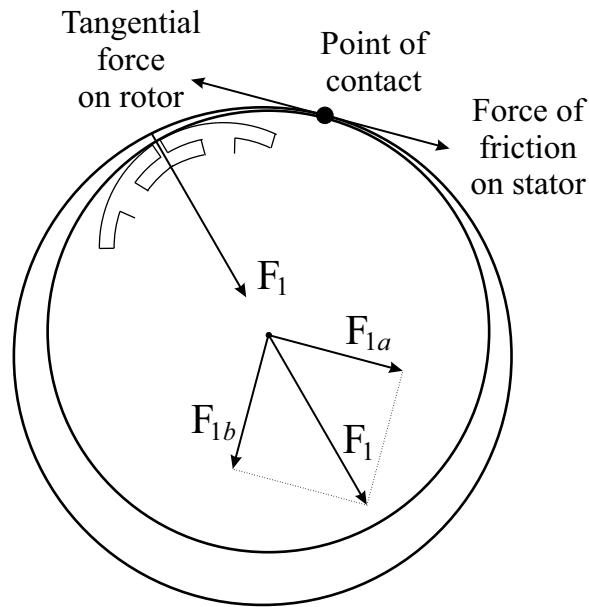


Figure 3.12. Static force vector analysis.

Tribology Phenomena

As it has been mentioned in section II, in this family of machines, the rotor will touch the stator at different contact points according to the excitation of the stator poles. The fact that the rotor is touching the stator, opens the door into having surfaces in contact while the machine is in operation (the asperities of both surfaces will be touching as shown in Fig. 3.13) Surfaces in contact will cause friction and wear to happen. Friction, lubrication, and wear are fundamentals of tribology phenomena[99]. When assessing a system's tribology need, one should consider if the contact between surfaces are continuous or intermittent.

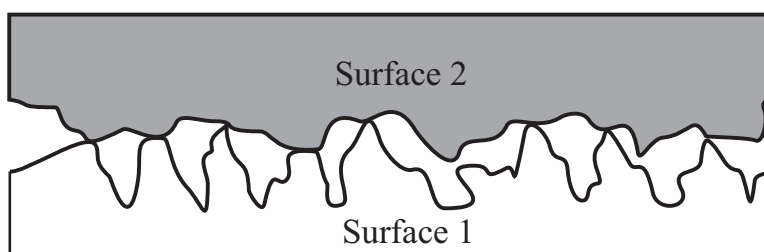


Figure 3.13. Asperities of two surfaces in contact.

Lubricant is normally used to reduce wear and has direct effect on the coefficient of friction. The thickness of the lubricant will be assessed using λ ratio, which is the ratio of fluid film thickness to the composite surface roughness as shown in (3.31).

$$\text{Composite surface roughness} = (r_{q1}^2 + r_{q2}^2)^{1/2} \quad (3.31)$$

in which r_{q1} and r_{q2} are root-mean-square roughness of surface 1 and surface 2, respectively[99].

According to [100] -[101],lubricants can be categorized according to the λ ratio as shown in Table. 3.1.

Table 3.1. Lubrication types with respect to lambda ratio

Hydrodynamic Lubrication (HD)	$5 < \lambda < 100$
Elastohydrodynamic Lubrication (EHL or EHD)	$3 < \lambda < 10$
Partial or mixed Lubrication	$1 < \lambda < 5$
Boundary Lubrication	$\lambda < 1$

In order to choose the proper lubricant, the type of the motion between two surfaces should be identified. If the motion is sliding then the hydrodynamic lubricant should be used and if the motion is rolling the elastohydrodynamic lubricant should be used [100]. In the case of airgap-less machine, the motion is considered as rolling so the elastohydrodynamic lubricant will be used to reduce wearing and consequently the lifetime of the machine.

For assessing the amount of wear, the wear coefficient factor (k) can be used. k depicts the volume of material removed per unit load. The wear coefficient can be calculated using (3.32) in which V , H , W , and d are the relative wear volume, the indentation hardness of the wearing material, normal load, and the sliding distance, respectively [102].

$$k = \frac{V.H}{W.d} \quad (3.32)$$

Wear Rate Proportional Factor

The life of an interface is inversely proportional to the wear rate proportional factor ($p_H V_s$) [103], in which p_H is the Hertzian contact stress calculated as shown in (3.33) and V_s is the sliding velocity.

$$p_H = \sqrt{\frac{F_i E^*}{2\pi H R^*}} \quad (3.33)$$

In (3.33), F_i is the contact force, E^* is the reduced modulus of elasticity, H is the thickness of the machine, and R^* is the composite radius of the curvature, respectively. Notice that, p_H is proportional to the reduced modulus of elasticity. Hence, a material with a smaller E^* is desirable for obtaining a smaller wear rate factor.

As an example, two different magnetic materials (Cobalt and Metglas) can be compared in terms of lifespan, using their modulus of elasticity: $E_{CO}^* = 209 \text{ Gpa}$ and $E_{Metglas}^* = 100 \text{ Gpa}$.

As shown above, the modulus of elasticity for Cobalt is almost two times higher than that of Metglas. While keeping the same operating condition, the wear rate factor of Cobalt will be 41% times higher than Metglas.

3.3 Four Bipole Machine and Generalization

Although the minimum number of bipoles to implement the concept of an airgap-less machine is three, the maximum number is a function of manufacturing capability. Indeed, the torque ripple reduces with an increase in the number of poles. Fig. 3.14 presents a 3D sketch of the proposed machine with four bipoles. Notice that although the number of poles increased, the operation principle is the same and so is the modeling approach.

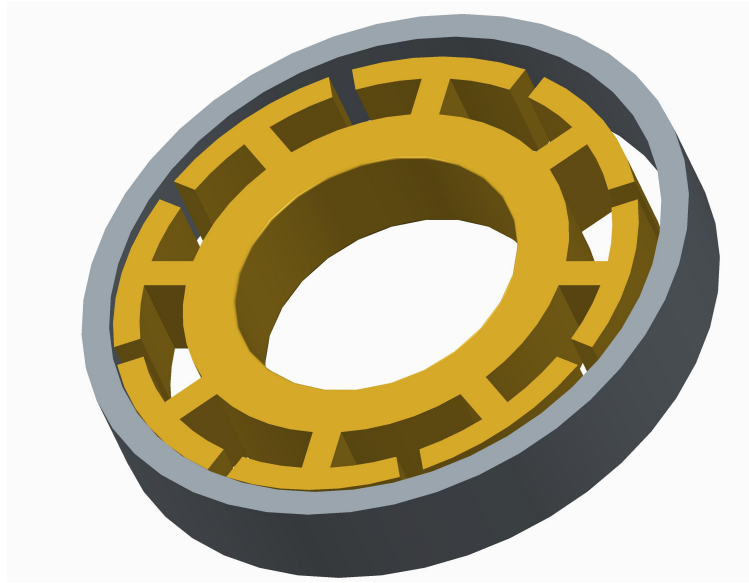
The total energy and electromagnetic torque for the four bipole machine are presented below:

$$\begin{aligned}
 W_c &= (L_{1a1a} + L_{1b1b})i_1^2 + (L_{2a2a} + L_{2b2b})i_2^2 \\
 &\quad + (L_{3a3a} + L_{3b3b})i_3^2 + (L_{4a4a} + L_{4b4b})i_4^2 \\
 T_e &= \frac{dw_c}{d\theta} = \Delta T_1 i_1^2 + \Delta T_2 i_2^2 + \Delta T_3 i_3^2 + \Delta T_4 i_4^2
 \end{aligned} \tag{3.34}$$

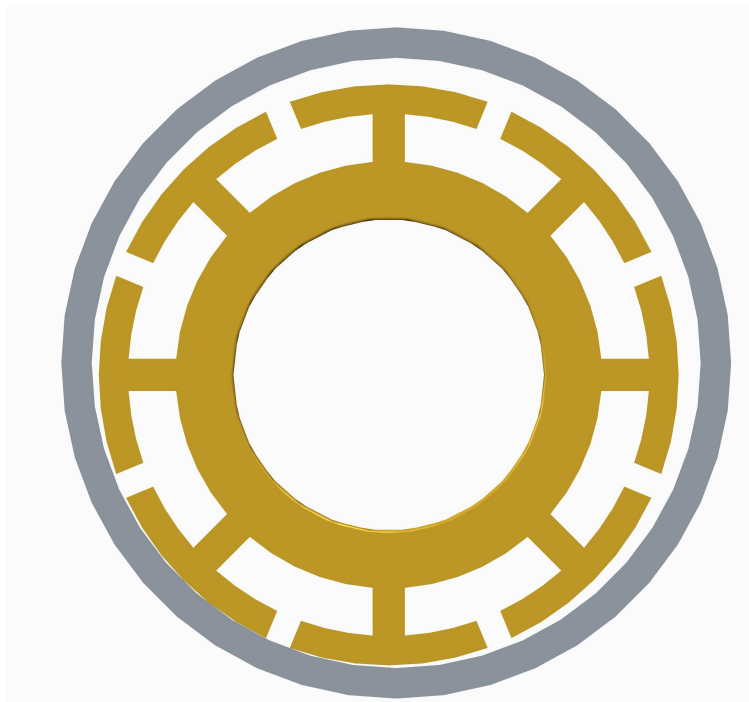
where:

$$\begin{aligned}
 \Delta T_1 &= -\frac{3.92r_{21}\sin\theta N^2\mu_0 A_s}{(2r_{21} - 1.96r_{21}\cos\theta)^2} \\
 \Delta T_2 &= -\frac{3.92r_{21}\sin\left(\theta + \frac{\pi}{2}\right) N^2\mu_0 A_s}{\left(2r_{21} - 1.96r_{21}\cos\left(\theta + \frac{\pi}{2}\right)\right)^2} \\
 \Delta T_3 &= -\frac{3.92r_{21}\sin(\theta + \pi) N^2\mu_0 A_s}{(2r_{21} - 1.96r_{21}\cos(\theta + \pi))^2} \\
 \Delta T_4 &= -\frac{3.92r_{21}\sin\left(\theta + \frac{3\pi}{2}\right) N^2\mu_0 A_s}{\left(2r_{21} - 1.96r_{21}\cos\left(\theta + \frac{3\pi}{2}\right)\right)^2}
 \end{aligned}$$

Despite the complexity of the drive system and machining the machine, a higher number of poles is beneficial to reduce the torque ripple.



(a)



(b)

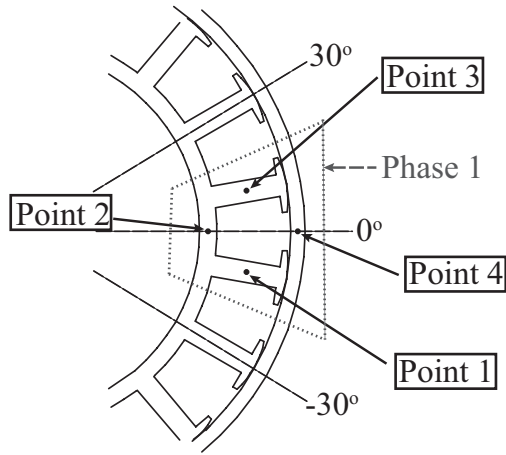
Figure 3.14. 3D views of the proposed 4 bipole machine. (a) stator-rotor in perspective, and (b) stator-rotor top-view.

3.4 Finite-Element Analysis

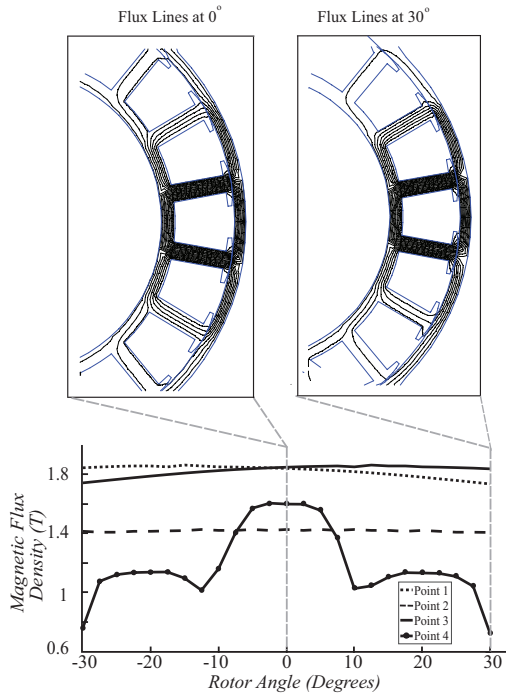
In order to find the magnetic saturation levels across the ferromagnetic material, a finite element analysis is performed using the Finite Elements Method Magnetics (FEMM[®]) software.

Fig. 3.15(a) shows four key points where the stator and rotor materials could saturate when phase one is active. The first three points are static points on the stator, whereas the fourth point moves along with the touching point of the rotor. The machine model is simulated in the FEMM[®] software by varying the touching point of the rotor from -30° to 30° at a constant current of 2.5 A through phase one. The magnetic flux density at the four key points is plotted against the rotor angle in Fig. 3.15(b).

It is evident from the graph that the magnetic flux density at points 1 and 3 are higher than the other points for all the rotor angles. This indicates that if the machine is going to saturate then the saturation will begin at Points 1 and 3. For a current of 2.5 A, the maximum flux density reached in the stator material is around 1.85 T (at Points 1 and 3). The saturation point for the stator material is 2 T. Magnetic flux lines for rotor angles 0 and 30 are highlighted in Fig. 3.15(b).



(a)



(b)

Figure 3.15. (a) Four key points for saturation analysis. (b) Flux density versus rotor angle for the key points.

3.5 Simulation and Experimental Results

MATLAB[®] and C++ codes have been used to simulate the proposed machines with three, four, and nine bipoles. The parameters used in this code are shown in Table 4.1. Figs. 3.16(a)-3.16(c) show simulation results for a machine with three bipoles. The same set of results are presented in Figs. 3.17(a)-3.17(c) and Figs. 3.18(a)-3.18(c) for machines with four and nine bipoles, respectively. The results were collected with the electrical frequency equal to 10 Hz. As expected, the torque ripple reduces by increasing the number of magnetic bipoles.

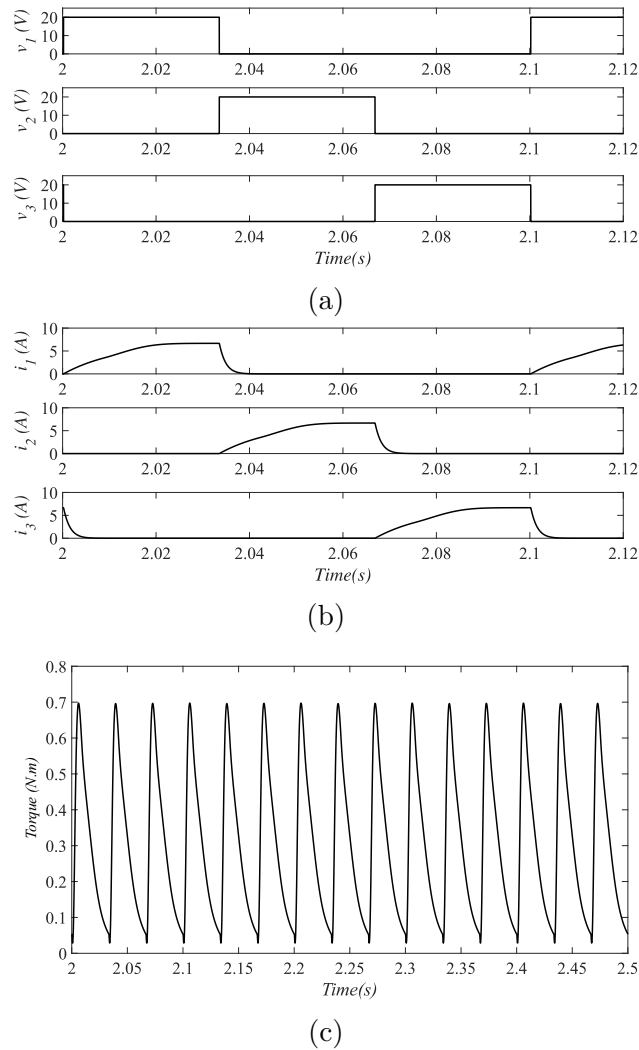


Figure 3.16. (a) Simulation results (3 bipole machine): (a) voltage, (b) current, (c) torque.

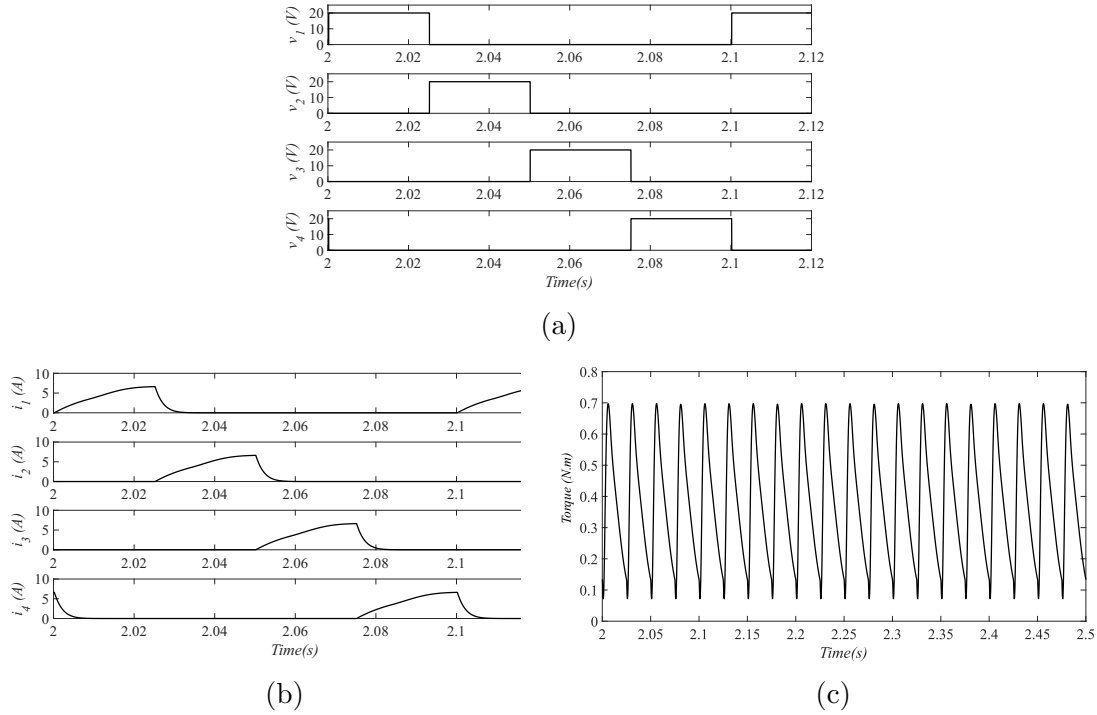


Figure 3.17. Simulation results (4 bipole machine): (a) voltage, (b) current, (c) torque.

A proof-of-concept laboratory prototype with nine magnetic bipoles (eighteen teeth) was built to validate the theoretical assumptions, see Fig. 4.10. The rotor in this prototype is made of low carbon steel 1018 which is shown in Fig. 4.10(a) and the stator is made of steel M19 shown in Fig. 4.10(b). Notice that in Fig. 4.10(b), the stator is not yet wrapped with windings.

The entire experimental setup for this prototype including the drive system is presented in Fig. 3.20. In this experimental setup, the inverter used to generate the machine voltages is IRAMX20UP60A. This inverter is a 3-leg inverter and since the proposed machine needs nine voltages, three of these inverters have been used.

A DC voltage of 20 V has been supplied to the system through a power supply shown in Fig. 3.20(a). Fig. 3.20(b) shows the setup including the scale that has been used to measure the tangential force. This force has been multiplied by the radius of the rotor in order to obtain the torque.

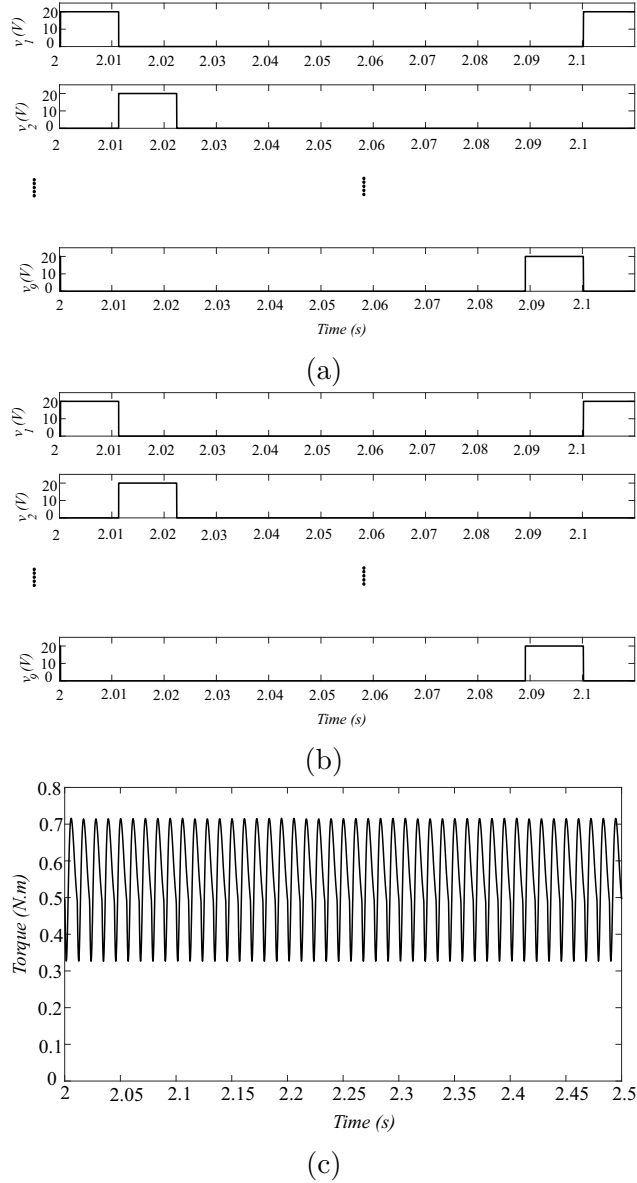
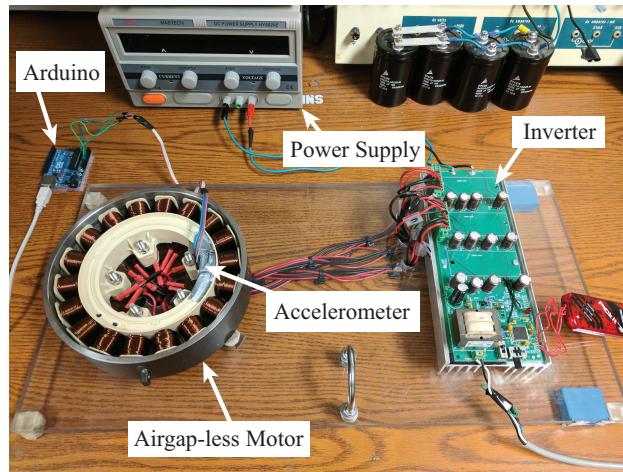


Figure 3.18. Simulation results (9 bipole machine): (a) voltage, (b) current, and (c) torque.

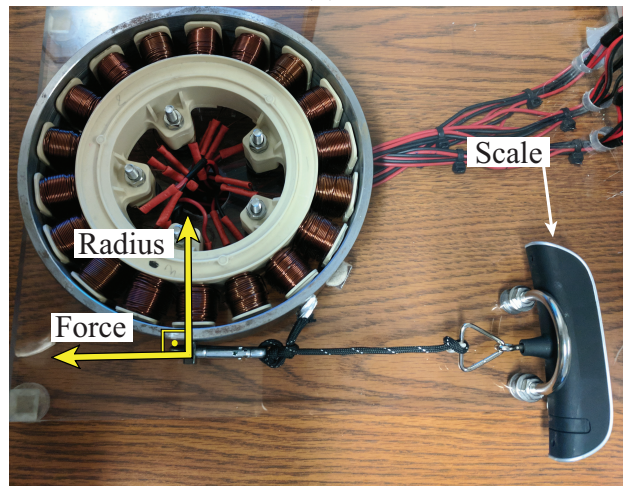
Fig. 3.21(a) shows the input DC voltage (top waveform) and the input DC current (bottom waveform) of the inverter. Control over direction and frequency of the machine was also tested experimentally. Fig. 3.21(b) shows the results obtained for direction control where the channel 1 of the scope shows the direction signal (0 meaning clockwise and 1 counter clockwise). The other signals show: voltage across phase 1, current through phase 1, and the current through phase 2, respectively. By observing the two currents, after the



Figure 3.19. Nine bipole machine: (a) rotor and (b) stator.

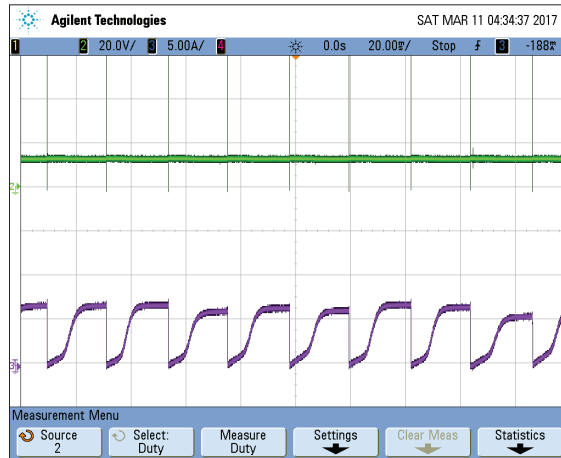


(a)

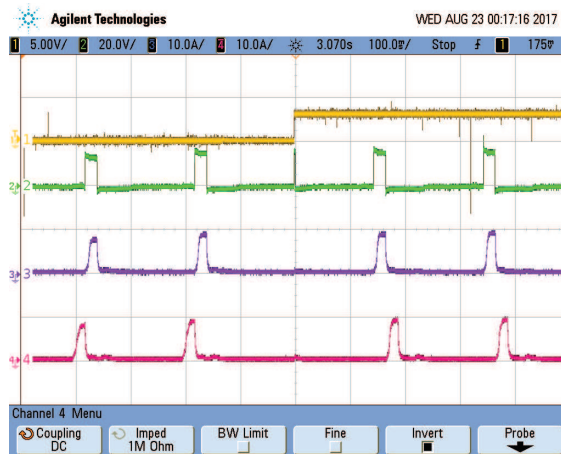


(b)

Figure 3.20. (a) experimental setup, (b) torque measurement setup.



(a)



(b)



(c)

Figure 3.21. Signals showing change of: (a) input voltage (top waveform) and DC link current (bottom waveform), (b) direction, and (c) frequency.

Table 3.2. Parameters used in the simulation

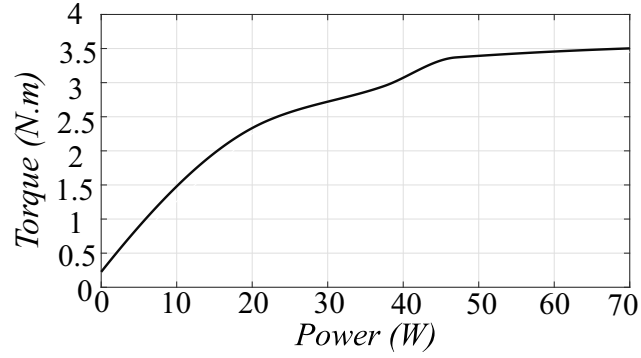
Parameter	Description	Value
B_m	Coefficient of friction	0.1
J_m	Moment of inertia	0.01 ($Kg.m^2$)
V_{dc}	DC link voltage	20 (V)
μ_0	Permeability of air	$4\pi \times 10^{-7}(H/m)$
μ_s	Relative Permeability of the stator	2000
μ_r	Relative Permeability of the rotor	700
l_s	Length of the flux path in the stator	0.1 (m)
l_r	Length of the flux path in the rotor	0.07 (m)
A_s	Cross sectional area of the stator	$140 \times 10^{-6}(m^2)$
A_r	Cross sectional area of the rotor	$25 \times 10^{-5}(m^2)$
N	Number of turns in each tooth	160
r	Series resistance in each winding	3 (Ω)
R_s	Stator radius	0.0953 (m)
R_r	Rotor radius	0.096 (m)
f_e	Electrical frequency	2 (Hz)

direction signal has changed, it is evident that the sequence of current signals have changed causing the machine to rotate in the other direction. A frequency ramp from 2 Hz to 10 Hz was implemented as shown in Fig. 3.21(c). This ramp starts when the top signal changes from 1 to 0 and ends when it returns to 1. The bottom two scope signals show the gating signal and the phase current, respectively.

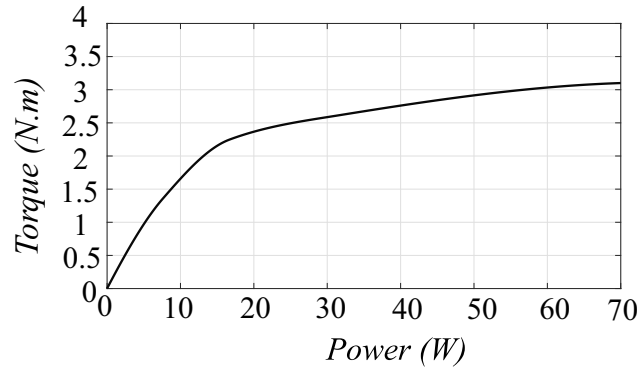
The proposed machine has been operated using two different electrical frequencies, 5 and 10 Hz as shown in Fig. 3.22(a) and 3.22(b) respectively. These figures show how the measured zero-speed torque relates to input electrical power.

When the speed is increased, the torque will decrease for the given power. For instance, the torque for the power of 35 W is around 3 $N \cdot m$, as shown in Fig. 3.22(a) with frequency of 5 Hz . The same amount of power provides 2.6 $N \cdot m$ in Fig. 3.22(b) when the frequency is 10 Hz .

Fig. 3.23 shows the experimental results collected for vibrations of the Airgap-less machine (top), and an induction machine (bottom). It is worth mentioning that the reference for the induction machine is IWY WPT-202 with the following specifications: 220/260 W , 50/60 Hz , and 2760/3300 rpm . An Arduino, communicating with Matlab, was connected to an ADXL335 accelerometer sensor from Adafruit. The sensor was placed at the base of both



(a)



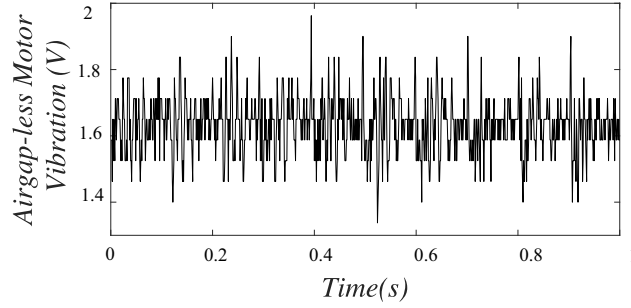
(b)

Figure 3.22. Torque vs. power for different operating frequencies: (a) 5 Hz and (b) 10 Hz.

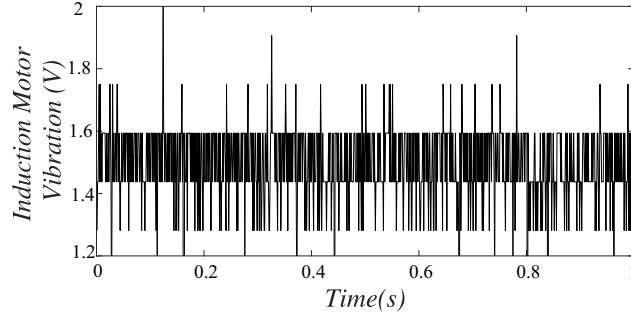
machines during the tests for a fair comparison. It is evident that the Airgap-less machine has higher peaks of vibration, as expected.

Fig. 3.24 shows the vibration signal for Airgap-less machine in frequency domain (FFT). This vibration test has been done while the machine was operating at the electrical frequency of 10 Hz. The fundamental component of this signal at 10 Hz and some harmonics are evident in Fig. 3.24. The FFT of the induction machine is not presented as it did not show any clear frequency component except the DC component, which was coming from the accelerometer.

As it has been shown in section IV-A the mechanical speed of the machine can be calculated as shown in (3.28). Fig. 3.25 shows the mechanical speed for 3 different excitation (electrical) frequencies (5, 7, and 10 Hz). Fig. 3.25 (top) and Fig.3.25 (bottom) show the simulation and experimental results, respectively.



(a)



(b)

Figure 3.23. Vibration signals for: (a) airgap-less machine and (b) induction machine.

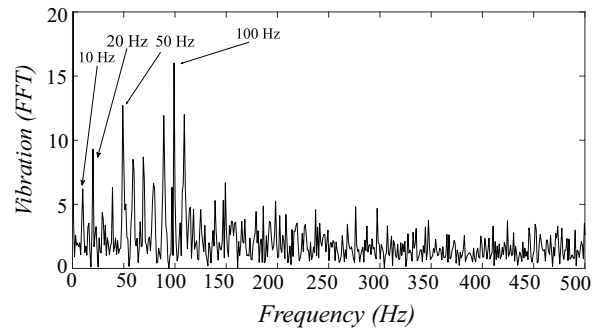


Figure 3.24. Fast Fourier Transform of airgap-less machine operating at 10 Hz.

3.6 Comparison and Conclusion

A new family of electric machines characterized by zero gap at the touching point have been proposed in this paper. Such machines are designed to generate higher level of torque as compared to other electric machines. The level of torque in the proposed machine allows

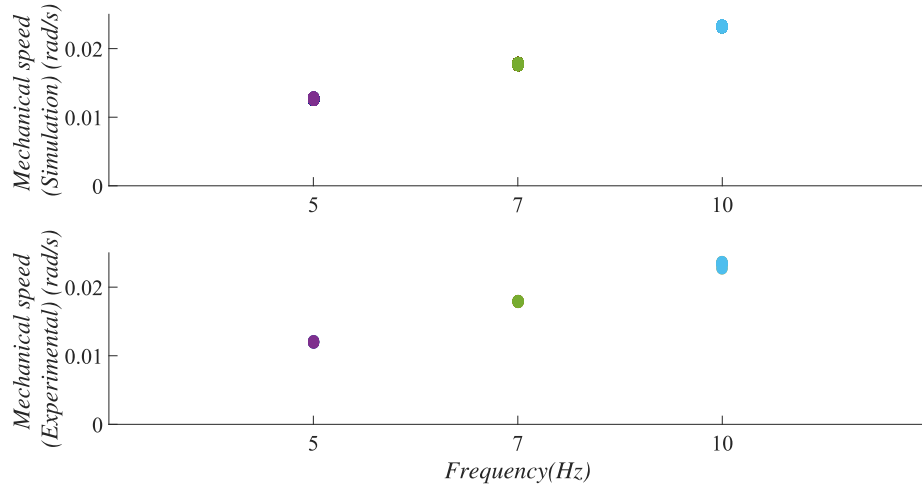


Figure 3.25. Mechanical speed versus electrical frequency: (top) simulation, and (bottom) experimental results.

it to be comparable to hydraulic machines in low speed high torque applications such as cranes and winches.

Fig. 5.1(a) shows the comparison between torque/mass of three different machines: (1) internal permanent magnet machine with $R = 80 \text{ mm}$, $L = 30 \text{ mm}$, $g = 0.6 \text{ mm}$, output torque $T_e = 36.5 \text{ N.m}$ (Mass $M = 12 \text{ kg}$), and speed range $\omega = 0 - 2200 \text{ rpm}$. [104], (2) inner rotor modulated PMSM with $R = 215 \text{ mm}$, $L = 36 \text{ mm}$, $g = 2 \text{ mm}$, output torque $T_e = 100 \text{ N.m}$ (Mass $M = 57.8 \text{ kg}$), and speed $\omega = 600 \text{ rpm}$ [105], and (3) airgap-less machine. As shown in this figure, the torque density of the airgap-less machine (the proposed machine) is approximately 5.6 N.m/kg . Notice that this torque has been obtained experimentally from the proposed machine with nine bipoles but without any optimization in terms of magnetic material and lamination. Even though there is room for improvement, the proof-of-concept prototype presented almost twice the torque density capability than the other electric machines proposed in the technical literature. The structures of the machines mentioned in Fig. 5.1(a) are as shown in Fig. 5.1(b).

Below are several electric machines have been compared in terms of their torque density and their torque producing ability.

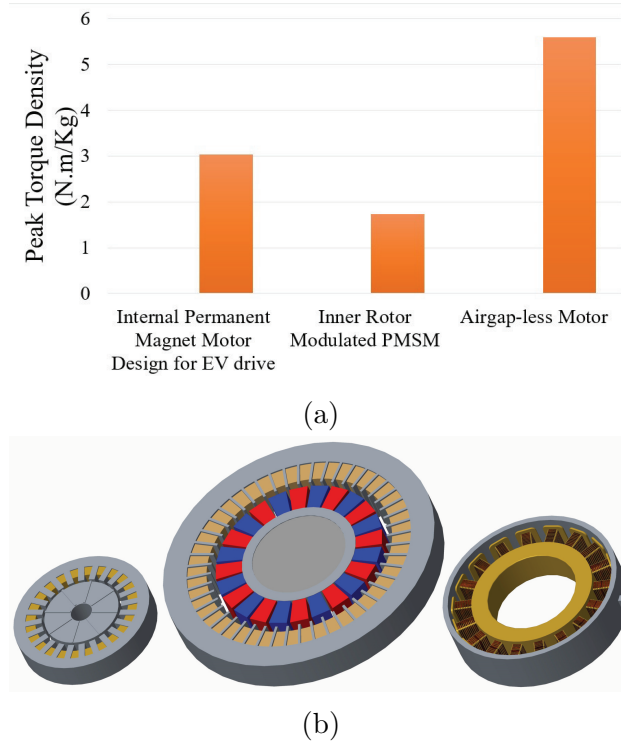


Figure 3.26. (a) Torque density comparison. (b) Structure of the compared machines.

Although achieving high torque is important in designing electric machines, nowadays torque density has become one of the most important topics among the electric machine designers. Since the space issue plays an important role in designing the machine, designers often try to minimize the space and maximize the torque which will result into a high torque density (torque per machine volume Nm/L).

Fig. 3.27 presents torque densities for seven high torque electric machines available in the literature. Among these machines, the airgap-less electric machine (proposed by the authors) is also presented. Except airgap-less electric machine, all other machines in this figure consist of permanent magnets, which will result into high torque and at the same time will add to the cost of the overall machine. Clearly, in this figure airgap-less electric machine does not win in terms of torque density but as mentioned there is no permanent magnet in the airgap-less electric machine.

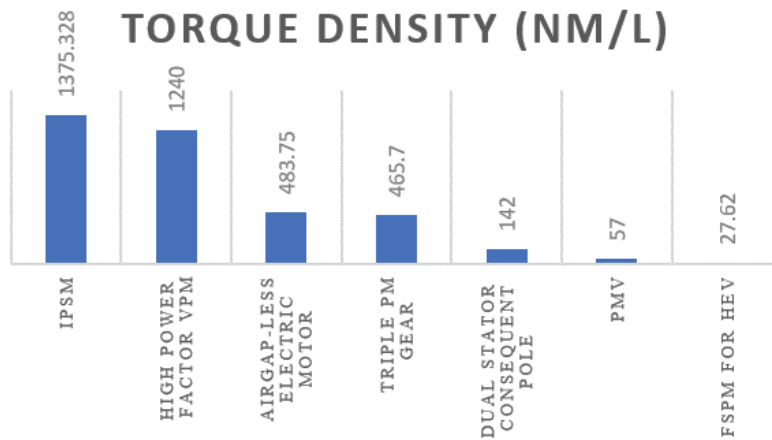


Figure 3.27. Torque Density Comparison Chart for Electric machines with PM

Fig. 3.28 in turn compares five high torque electric machines without permanent magnets with the airgap-less electric machine.

In the next chapter of this dissertation, the simulation of airgap-less electric machine has been done using Runge-Kutta 4th order algorithm instead of Euler's algorithm. The reason for this study is to obtain the most optimized results for this machine.

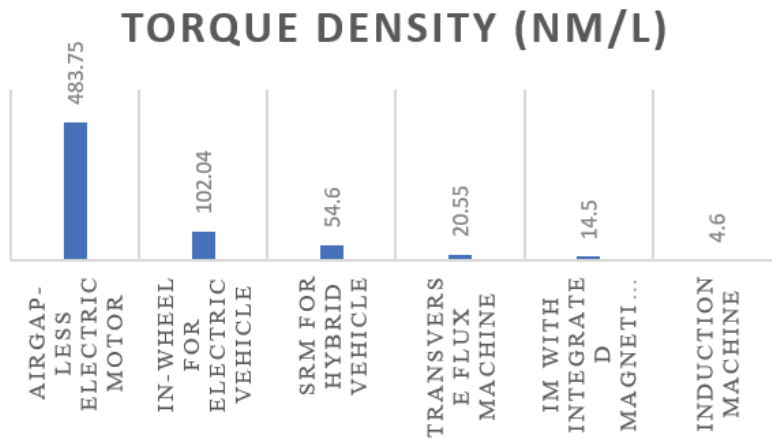


Figure 3.28. Torque Density Comparison Chart for Electric machines without PM

4. MODELING AND SIMULATION OF AN AIRGAP-LESS ELECTRIC MACHINE IN C++ USING RUNGE KUTTA INTEGRATION METHOD

In this chapter, the state space representation has been employed for the analytical modeling of the airgap-less electric machine. As mentioned in previous chapters, airgap-less electric machine [83], [106], [107] is comparable to hydraulic machines according to its high torque density and high efficiency. Therefore, it is crucial to employ optimized algorithms in developing its analytical modeling and simulation. This paper presents the analytical modeling and simulation of airgap-less electric machine using C++ programming language along side with 4th Runge-Kutta (RK) algorithm as integration method.

This chapter is organized with the following sections: Section I presents the concept and modeling of an airgap-less machine including airgap modelling and magnetic circuit using RK integration method which is followed by Section II where inductance, energy, and torque modeling using RK integration method has been discussed. Using RK integration method, Section III presents the mechanical analysis of the machine, which is followed by section V, in which simulation and experimental results have been presented.

4.1 Inductance, Energy, and Torque Modeling using Runge-Kutta Integration Method

In this study, the simulation of the airgap-less electric machine has been done considering no overlap in exciting voltages; hence the mutual inductances have been neglected in the calculation of co-energy and torque. The self-inductance at each pole will be calculated as the sum of inductance at both teeth of that pole. For example the inductance at pole 1 (L_1) is equal to $L_{1a} + L_{1b}$. By definition, the self-inductance at each tooth is given by (4.1).

$$L_y = \frac{N \Phi_y}{i_n} = \frac{N^2}{\mathfrak{R}_{eq}} \quad (4.1)$$

in which $y = 1a, 1b, 2a, 2b, \dots, 9a, 9b$, $n = 1, 2, 3, \dots, 9$, and \mathfrak{R}_{eq} is the equivalent reluctance of the circuit shown in Fig. 3.8.

After finding the inductances, the voltages across each pole can be calculated as shown in (4.2):

$$v_n = r_n i_n + L_n \frac{di_n}{dt} \quad (4.2)$$

in which r_n is the series resistance in each inductor. Therefore the current through each phase can be calculated from (4.2) using an integration method. The RK algorithm has been used in this chapter as an integration method toward solving the differential equations. The functions defining the current using RK algorithm are as shown in Fig. 4.1. Each of these functions will return the derivative of the phase current with respect to time. As it is shown in (4.2), the derivative of the current will be as shown in (4.3).

$$\frac{di_n}{dt} = \frac{v_n}{L_n} - \frac{r_n}{L_n} i_n \quad (4.3)$$

```

double f(double i1, double V1, double t, double L1)
{
return (1 / L1)* V1 - (r / L1)* i1;
}
double f1(double i2, double V2, double t, double L2)
{
return (1 / L2)* V2 - (r / L2)* i2;
}
double f2(double i3, double V3, double t, double L3)
{
return (1 / L3)* V3 - (r / L3)* i3;
}
double f3(double i4, double V4, double t, double L4)
{
return (1 / L4)* V4 - (r / L4)* i4;
}
double f4(double i5, double V5, double t, double L5)
{
return (1 / L5)* V5 - (r / L5)* i5;
}
double f5(double i6, double V6, double t, double L6)
{
return (1 / L6)* V6 - (r / L6)* i6;
}
double f6(double i7, double V7, double t, double L7)
{
return (1 / L7)* V7 - (r / L7)* i7;
}
double f7(double i8, double V8, double t, double L8)
{
return (1 / L8)* V8 - (r / L8)* i8;
}
double f8(double i9, double V9, double t, double L9)
{
return (1 / L9)* V9 - (r / L9)* i9;
}

```

Figure 4.1. Differential equations for calculating the currents in each phase.

While using the RK algorithm 4^{th} order, there will be 4 coefficients for each function to be calculated. Fig. 4.2 shows an example of calculating these coefficients for the current in phase 1. In this example $K11, K12, K13,$ and $K14$ are the slopes of the RK algorithm.

After calculating the current and self-inductance of each phase, the co-energy for that phase will be calculated as shown in (4.4).

$$w_{cn} = \frac{1}{2} L_n i_n^2 \quad (4.4)$$

```

k11[j] = f(i1[j], V1[j], t[j], L1[j]);
k12[j] = f(i1[j] + (h / 2), V1[j], t[j] + (h / 2)*k11[j], L1[j]);
k13[j] = f(i1[j] + (h / 2), V1[j], t[j] + (h / 2)*k12[j], L1[j]);
k14[j] = f(i1[j] + h, V1[j], t[j] + (h)*k13[j], L1[j]);
rk1[j] = k11[j] + 2 * k12[j] + 2 * k13[j] + k14[j];
RK1[j] = rk1[j] / 6;
i1[j + 1] = i1[j] + RK1[j] * h;

```

Figure 4.2. Calculation of RK coefficients for the current in phase 1.

The total co-energy will be the sum of co-energies at each phase as shown in (4.5)

$$w_c = \sum_{n=1}^9 w_{cn} \quad (4.5)$$

The electromagnetic torque then will be calculated by taking the derivative of co-energy with respect to the angle θ as shown in (4.6)

$$T_e = \frac{\partial W_c}{\partial \theta} \quad (4.6)$$

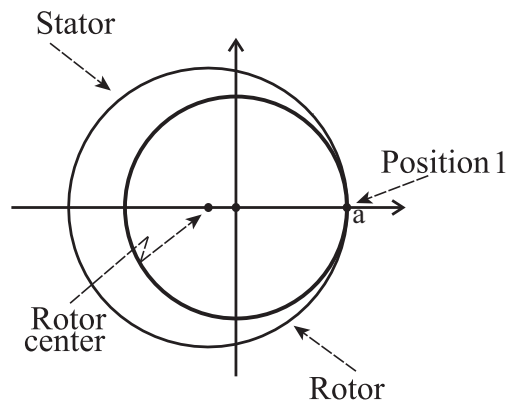
4.2 Mechanical Analysis

The physical dimensions of the stator and rotor (i.e., r_1 and r_2) will play an important role on how the mechanical speed (ω_m) is related to the electrical angular frequency (ω_e) defined by the inverter. To define how much the rotor rotates in degrees when the stator is being excited, consider position '1' where the stator and rotor are initially in contact (point 'a') as shown in Fig. 4.3(a). After θ_e electrical degrees from the stator's point of view, the rotor will touch position 'p' and point 'a' will travel for θ_m degrees as shown in Fig. 4.3 (b).

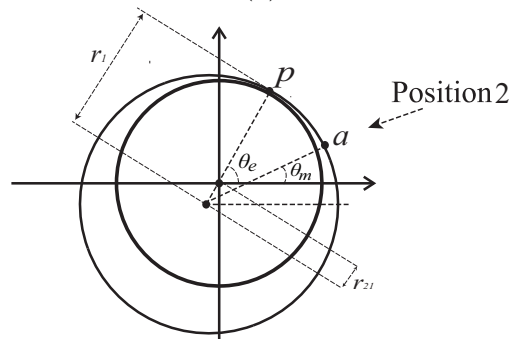
The mechanical speed (ω_m) has been calculated using equation (4.7). This equation has been employed in C++ using Runge-Kutta integration method as shown in Fig. 4.4.

$$\frac{d\omega_m}{dt} = \frac{(T_{elec} - T_{Load} - B_m\omega_m)}{J_m} \quad (4.7)$$

in which T_{elec} , T_{Load} , B_m , and J_m are electromagnetic torque, load torque, coefficient of friction, and moment of inertia respectively.



(a)



(b)

Figure 4.3. (a) Initial position of the rotor. (b) Position of the rotor after θ_e electrical degrees from stator point of view.

```

double f9(double wm, double t, double Telec)
{
return wm = (Telec - Tload - Bm *wm) / Jm;
}
k91[j] = f9(wm[j], t[j], Telec[j]);
k92[j] = f9(wm[j] + (h / 2), t[j] + (h / 2)*k91[j], Telec[j]);
k93[j] = f9(wm[j] + (h / 2), t[j] + (h / 2)*k92[j], Telec[j]);
k94[j] = f9(wm[j] + h, t[j] + (h)*k93[j], Telec[j]);
rk9[j] = k91[j] + 2 * k92[j] + 2 * k93[j] + k94[j];
RK9[j] = rk9[j] / 6;
wm[j + 1] = wm[j] + RK9[j] * h;

```

Figure 4.4. Calculation mechanical speed using RK integration method.

The mechanical speed of the machine can also be calculated using the mechanical displacement of the rotor (θ_m). Using the geometric approach shown in Fig. 4.3(b), the mechanical displacement of the rotor and the electrical angle can be related as shown in (4.8)

$$\theta_m = \frac{r_{21}}{r_1} \theta_e \quad (4.8)$$

According to (4.8), the relationship between electrical and mechanical angular speed can be shown as:

$$\omega_m = \frac{r_{21}}{r_1} \omega_e \quad (4.9)$$

The mechanical speed can be changed by either modifying the physical dimensions of the stator and rotor or by increasing the electrical frequency (f_e).

Using the mechanical speed shown in (4.9), the angle θ_m can be calculated as shown in (4.10) which has been implemented in C++ using RK shown in Fig. 4.5.

$$\omega_m = \frac{d\theta_m}{dt} \quad (4.10)$$

4.3 Simulation and Experimental Results

MATLAB[®] and C++ codes have been used to model and simulate the nine phase airgapless machine using the Runge-Kutta integration method. The parameters used in this code

```

double f10(double th, double t, double wm)
{
return th = wm;
}
k101[j] = f10(th[j], t[j], wm[j]);
k102[j] = f10(th[j] + (h / 2), t[j] + (h / 2)*k101[j], wm[j]);
k103[j] = f10(th[j] + (h / 2), t[j] + (h / 2)*k102[j], wm[j]);
k104[j] = f10(th[j] + h, t[j] + (h)*k103[j], wm[j]);
rk10[j] = k101[j] + 2 * k102[j] + 2 * k103[j] + k104[j];
RK10[j] = rk10[j] / 6;
th[j + 1] = th[j] + RK10[j] * h;

```

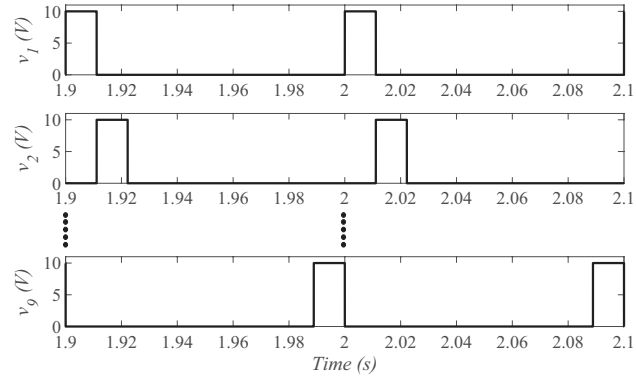
Figure 4.5. Calculation of the position of the rotor using RK integration method.

are shown in Table 4.1. As it has been shown in sections III and IV the Runge-Kutta integration method has been used in this code due to its high precision degree [108].

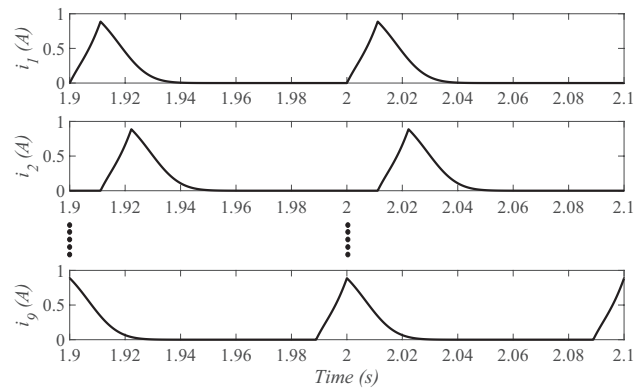
Table 4.1. Parameters used in the simulation

Parameter	Description	Value
B_m	Coefficient of friction	0.1295
J_m	Moment of inertia	0.1 ($Kg.m^2$)
V_{dc}	DC link voltage	10 (V)
μ_0	Permeability of air	$4\pi \times 10^{-7} (H/m)$
μ_s	Relative Permeability of the stator	2000
μ_r	Relative Permeability of the rotor	700
l_s	Length of the flux path in the stator	0.1 (m)
l_r	Length of the flux path in the rotor	0.07 (m)
A_s	Cross sectional area of the stator	$140 \times 10^{-6} (m^2)$
A_r	Cross sectional area of the rotor	$25 \times 10^{-5} (m^2)$
N	Number of turns in each tooth	160
r	Series resistance in each winding	3 (Ω)
R_s	Stator radius	0.0953 (m)
R_r	Rotor radius	0.096 (m)
f_e	Electrical frequency	10 (Hz)

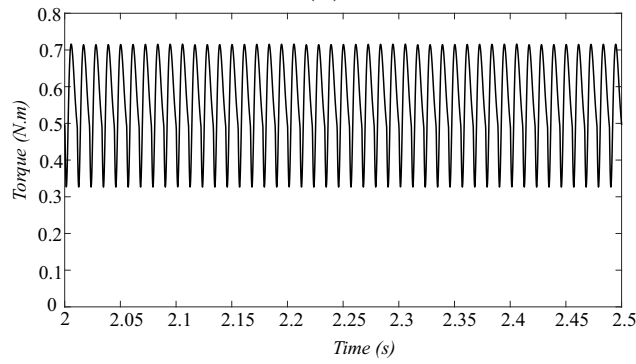
Figs. 4.6(a)-4.6(c) show simulation results for a machine with nine bipoles. The results were collected with the electrical frequency equal to 10 Hz. This figure shows nine phase voltages applied to the machine, nine phase currents and the electromagnetic torque, respectively.



(a)

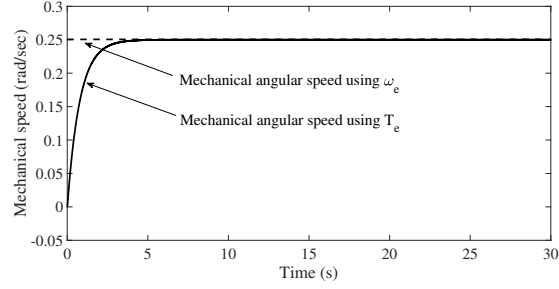


(b)

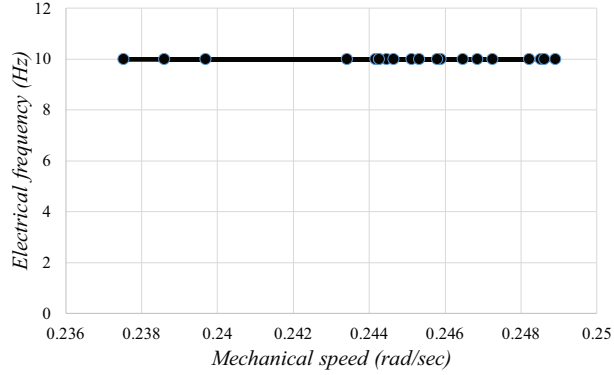


(c)

Figure 4.6. Simulation results (9 bipole machine): (a) voltage, (b) current, (c) torque.



(a)



(b)

Figure 4.7. Simulation results (9 bipole machine): (a) mechanical speed using T_e and (b) mechanical speed using ω_e .

Fig. 4.7(a) shows the mechanical speed obtained from the electromagnetic torque (4.7) and the mechanical speed obtained directly from the electrical angular frequency (4.9). As it is evident in this figure, in the steady state operation the mechanical speed obtained from the electromagnetic torque will match the expected mechanical speed. Fig. 4.7(b) in turns shows the mechanical speed obtained experimentally at the electrical frequency of 10 Hz. As it is evident in Figs. 4.7(a) and (b) the simulation and experimental results are both around 0.25 rad/sec with $f_e = 10$ Hz.

According to (4.9), the mechanical frequency (f_m) and the electrical frequency (f_e) have the relationship shown in (4.11).

$$f_m = \frac{r_{21}}{r_1} f_e \quad (4.11)$$

The mechanical frequency has been calculated for 10 different electrical frequencies using (4.11) and the results have been validated using the experimental setup. Fig. 4.8 shows the comparison between mechanical frequency obtained theoretically and experimentally for different electrical frequencies.

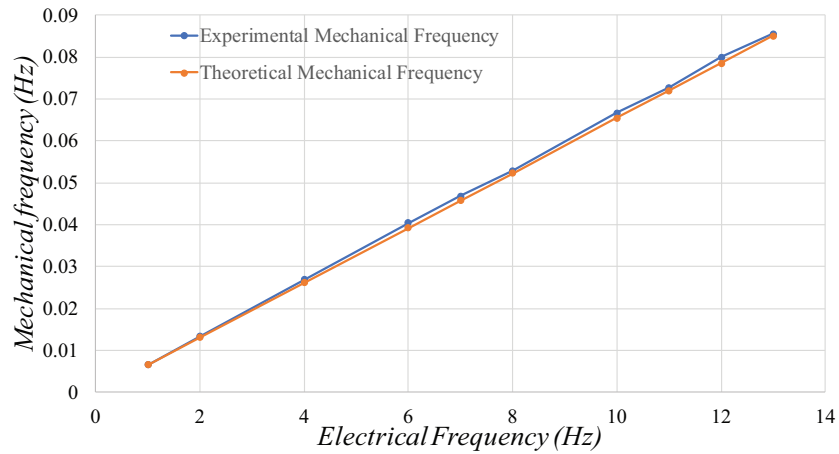


Figure 4.8. Comparison between theoretical and experimental mechanical frequency.

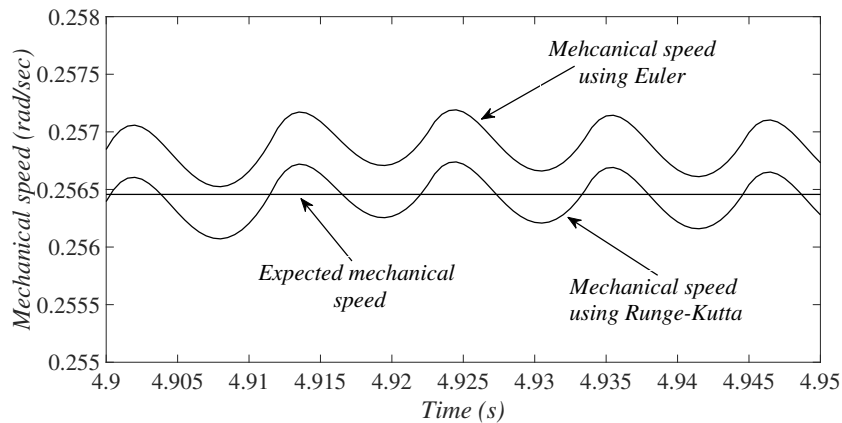
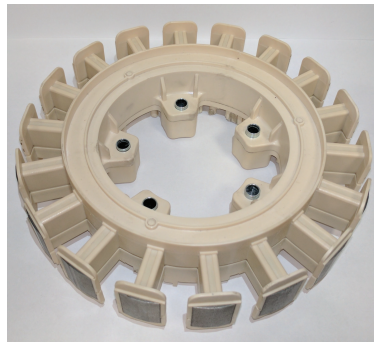


Figure 4.9. Comparison between mechanical speeds obtained using Euler and Runge-kutta integration method.

It is worth mentioning that the simulation for this machine has been done using Euler integration method as well as Runge-kutta methods. The main reason for choosing Runge-kutta integration method instead of Euler was that the Euler method has more error in comparison with Runge-kutta. Fig. 4.9 shows the comparison between mechanical speed



(a)



(b)

Figure 4.10. Nine bipole machine: (a) rotor and (b) stator.

obtained from Runge-kutta and Euler integration method respectively. As it is evident in this figure the mechanical speed obtained using Runge-kutta method matched the expected mechanical speed with less error compare to Euler method. A proof-of-concept laboratory prototype with nine magnetic bipoles (eighteen teeth) was built to validate the theoretical assumptions, see Fig. 4.10. The rotor in this prototype is made of low carbon steel 1018 which is shown in Fig. 4.10(a) and the stator is made of steel M19 shown in Fig. 4.10(b). Notice that in Fig. 4.10(b), the stator is not yet wrapped with windings.

In this section, the RK integration method has been used to simulate the nine-phase airgap-less machine. The reason for choosing RK method over the other integration methods was its high precision. For comparison purpose, the simulation of this nine-phase machine has been done using Euler integration method. The results clearly show that the Euler integration method matched the expected results (experimental results) with higher error in comparison with RK method. Fig. 4.9 demonstrate this comparison for the mechanical speed of the machine.

5. SUMMARY AND FUTURE WORKS

In this dissertation, a family of electric machines characterized by zero gap at the touching point have been proposed. Such machines are designed to generate higher level of torque as compared to other electric machines. The level of torque in the proposed machine (Airgap-less machine) allows it to be comparable to hydraulic motors in low speed high torque applications such as cranes and winches.

Fig. 5.1(a) shows the comparison between torque/mass of three different machines: (1) internal permanent magnet machines with $R = 80 \text{ mm}$, $L = 30 \text{ mm}$, $g = 0.6 \text{ mm}$, output torque $T_e = 36.5 \text{ N.m}$ (Mass $M = 12 \text{ kg}$), and speed range $\omega = 0 - 2200 \text{ rpm}$. [104], (2) inner rotor modulated PMSM with $R = 215 \text{ mm}$, $L = 36 \text{ mm}$, $g = 2 \text{ mm}$, output torque $T_e = 100 \text{ N.m}$ (Mass $M = 57.8 \text{ kg}$), and speed $\omega = 600 \text{ rpm}$ [105], and (3) airgap-less machine. As shown in this figure, the torque density of the airgap-less motor (the proposed motor) is approximately 5.6 N.m/kg . Since the main goal was to compare the simulation results with experimental results, there have been no optimization in terms of magnetic material and lamination in the simulation. This way it was guaranteed that the simulation is done in the same condition as the experimental setup to have a fair comparison. Notice that even though there is room for improvement, this machine presented almost twice the torque density capability than the other electric machines proposed in the technical literature. The structures of the motors mentioned in Fig. 5.1(a) are as shown in Fig. 5.1(b).

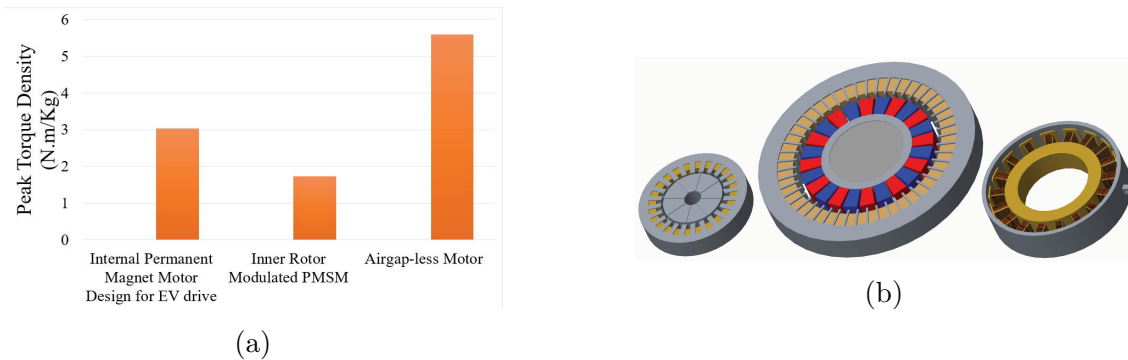


Figure 5.1. (a) torque density comparison. (b) structure of the compared motors (in scale).

This dissertation has the potential to expand in several areas such as: 1- Optimization of the airgap-less electric machine in terms of magnetic material and lamination, 2- Designing a PID controller for this machine to guarantee the lowest torque ripple possible, and 3- Analyze this motor with overlapped voltages. After achieving the above goals, and obtained the most optimized airgap-less electric machine, the following steps will be done as an extension to this research: 1- As mentioned in the introduction of this dissertation and shown in Fig. 2.5(b) a mechanical gear can be used to convert the combined translational and rotational movement of this machine into rotational only movement. 2- The airgap-less electric machines will then be compared to the J-Series hydraulic machine and among themselves (airgap-less electric motor with different number of poles as well as internal and external rotor). It is expected that the proposed machine drive systems with higher number of stator poles will be able to generate a better torque resolution. 3- Measuring the torque capability of each machine with a torque sensor (dynamometer) that is capable of measuring the torque and the rotational speed simultaneously. 4- When the torque and speed of this machine are measured, the braking capability advantage of this motor will be demonstrated. The hydraulic motors need to activate their braking system after turning the power off, while the proposed one will be able to stop their operation faster since it is driven directly by a controlled power supply. It is worth mentioning that the hydraulic motors have an extra locking system that is activated when the power supply is off, which delays the stopping process. 5- For finding the efficiency of the proposed machines, both voltage and current from the dc-link of the drive system will be measured and compared to the output mechanical load for calculation of the efficiency. The same methodology will be employed for the hydraulic machine, i.e., both input electric power and output mechanical power will be used for efficiency calculation. It is expected that the proposed machines will have higher efficiency due to their reduced number of energy conversion stages. Instead of using electric machine, pump, hydraulic connections, braking system, and the hydraulic machine itself, the proposed devices are constituted of only the electric machine and its drive system. The drive system is a power electronics based device and can be designed to have an efficiency close to 98%.

REFERENCES

- [1] V. Manescu (Paltanea, G. Paltanea, G. Horia, G. Scutaru, and I. Peter, “High efficiency electrical motors state of the art and challenges,” *Revue Roumaine des Sciences Techniques - Serie Électrotechnique et Énergétique*, vol. 62, pp. 14–18, Jan. 2017.
- [2] A. Istanes, “Impacts of a changing climate on infrastructure: Buildings, support systems, and industrial facilities,” in *2006 IEEE EIC Climate Change Conference*, 2006, pp. 1–4. DOI: [10.1109/EICCCC.2006.277269](https://doi.org/10.1109/EICCCC.2006.277269).
- [3] M. Torbicki, “The longtime safety and resilience prediction of the baltic oil terminal critical infrastructure impacted by weather changes,” in *2019 International Conference on Information and Digital Technologies (IDT)*, 2019, pp. 497–503. DOI: [10.1109/DT.2019.8813456](https://doi.org/10.1109/DT.2019.8813456).
- [4] K. Kołowrocki, E. Kuligowska, J. Soszyńska-Budny, and M. Torbicki, “An approach to safety prediction of critical infrastructure impacted by climate-weather change process,” in *2017 International Conference on Information and Digital Technologies (IDT)*, 2017, pp. 183–186. DOI: [10.1109/DT.2017.8024294](https://doi.org/10.1109/DT.2017.8024294).
- [5] K. Kołowrocki, J. Soszyńska-Budny, and M. Torbicki, “Critical infrastructure impacted by operation and climate change safety and resilience indicators,” in *2018 IEEE International Conference on Industrial Engineering and Engineering Management (IEEM)*, 2018, pp. 991–995. DOI: [10.1109/IEEM.2018.8607830](https://doi.org/10.1109/IEEM.2018.8607830).
- [6] M. Bogalecka and K. Kotowrocki, “Prediction of critical infrastructure accident losses of chemical releases impacted by climate-weather change,” in *2018 IEEE International Conference on Industrial Engineering and Engineering Management (IEEM)*, 2018, pp. 788–792. DOI: [10.1109/IEEM.2018.8607462](https://doi.org/10.1109/IEEM.2018.8607462).
- [7] P. Faggian and G. Decimi, “An updated investigation about climate-change hazards that might impact electric infrastructures,” in *2019 AEIT International Annual Conference (AEIT)*, 2019, pp. 1–5. DOI: [10.23919/AEIT.2019.8893297](https://doi.org/10.23919/AEIT.2019.8893297).
- [8] M. Torbicki, “Longtime prediction of climate-weather change influence on critical infrastructure safety and resilience,” in *2018 IEEE International Conference on Industrial Engineering and Engineering Management (IEEM)*, 2018, pp. 996–1000. DOI: [10.1109/IEEM.2018.8607308](https://doi.org/10.1109/IEEM.2018.8607308).
- [9] A. De Almeida, F. Ferreira, J. Fong, and P. Fonseca, “Eup lot 11 motors ecodesign assessment of energy using products final report for the european commission brussels belgium,” *ISR-Univ. Coim-bra*, 2008.
- [10] “Carbon dioxide concentration | nasa global climate change,” *NASA*, Apr. 2019.
- [11] P. WaIde and C. U. Brunner, “Energy-efficiency policy opportunities for electric motor-driven systems,” *OECD Publishing*, 2011.
- [12] M. K. Yoon, C. S. Jeon, and S. K. Kauh, “Efficiency increase of an induction motor by improving cooling performance,” *IEEE Transactions on Energy Conversion*, vol. 17, no. 1, pp. 1–6, Mar. 2002.

- [13] L. Szabó, “A survey on the efficiency improve of electrical machines,” in *2019 26th International Workshop on Electric Drives: Improvement in Efficiency of Electric Drives (IWED)*, Jan. 2019, pp. 1–6.
- [14] T. Dong, C. Zhu, F. Zhou, H. Zhang, F. Lu, and X. Zhang, “Innovated approach of predictive thermal management for high-speed propulsion electric machines in more electric aircraft,” *IEEE Transactions on Transportation Electrification*, vol. 6, no. 4, pp. 1551–1561, 2020. DOI: [10.1109/TTE.2020.3017764](https://doi.org/10.1109/TTE.2020.3017764).
- [15] Z. Zhang, W. Geng, Y. Liu, and C. Wang, “Feasibility of a new ironless-stator axial flux permanent magnet machine for aircraft electric propulsion application,” *CEST Transactions on Electrical Machines and Systems*, vol. 3, no. 1, pp. 30–38, 2019. DOI: [10.30941/CESTEMS.2019.00005](https://doi.org/10.30941/CESTEMS.2019.00005).
- [16] Y. Luo, X. Luo, L. Zhu, S. Jiang, and M. Zhao, “Efficiency improvement in electric propeller by maximum efficiency point tracker,” in *2019 22nd International Conference on Electrical Machines and Systems (ICEMS)*, 2019, pp. 1–4. DOI: [10.1109/ICEMS.2019.8922326](https://doi.org/10.1109/ICEMS.2019.8922326).
- [17] K. Sakai, K. Matsuda, and N. Yuzawa, “Permanent magnet motors capable of pole-changing without changing the connection of the windings for high efficiency,” in *2015 IEEE International Electric Machines Drives Conference (IEMDC)*, 2015, pp. 468–474. DOI: [10.1109/IEMDC.2015.7409100](https://doi.org/10.1109/IEMDC.2015.7409100).
- [18] X. Liu, D. Wu, Z. Q. Zhu, A. Pride, R. P. Deodhar, and T. Sasaki, “Efficiency improvement of switched flux pm memory machine over interior pm machine for ev/hev applications,” *IEEE Transactions on Magnetics*, vol. 50, no. 11, pp. 1–4, 2014. DOI: [10.1109/TMAG.2014.2323556](https://doi.org/10.1109/TMAG.2014.2323556).
- [19] W. Q. Chu, Z. Q. Zhu, J. Zhang, X. Liu, D. A. Stone, and M. P. Foster, “Investigation on operational envelopes and efficiency maps of electrically excited machines for electrical vehicle applications,” *IEEE Transactions on Magnetics*, vol. 51, no. 4, pp. 1–10, 2015. DOI: [10.1109/TMAG.2014.2359008](https://doi.org/10.1109/TMAG.2014.2359008).
- [20] A. Rassolkin, H. Heidari, A. Kallaste, T. Vaimann, J. P. Acedo, and E. Romero-Cadaval, “Efficiency map comparison of induction and synchronous reluctance motors,” in *2019 26th International Workshop on Electric Drives: Improvement in Efficiency of Electric Drives (IWED)*, 2019, pp. 1–4. DOI: [10.1109/IWED.2019.8664334](https://doi.org/10.1109/IWED.2019.8664334).
- [21] D. Binesti and J. P. Ducreux, “Core losses and efficiency of electrical motors using new magnetic materials,” *IEEE Transactions on Magnetics*, vol. 32, no. 5, pp. 4887–4889, Sep. 1996.
- [22] J. D. Widmer, R. Martin, and M. Kimiabeigi, “Electric vehicle traction motors without rare earth magnets,” *Sustainable Materials and Technologies*, vol. 3, pp. 7–13, Apr. 2015. DOI: [10.1016/j.susmat.2015.02.001](https://doi.org/10.1016/j.susmat.2015.02.001).
- [23] Y. Takano, A. Chiba, S. Ogasawara, M. Takeno, N. Hoshi, T. Imakawa, and M. Take moto, “Torque density and efficiency improvements of a switched reluctance motor without rare earth material for hybrid vehicles,” in *2010 IEEE Energy Conversion Congress and Exposition*, Sep. 2010, pp. 2653–2659.

- [24] K. Binnemans, P. T. Jones, B. Blanpain, T. [Gerven], Y. Yang, A. Walton, and M. Buchert, “Recycling of rare earths: A critical review,” *Journal of Cleaner Production*, vol. 51, pp. 1–22, 2013, ISSN: 0959-6526.
- [25] F. Ronning and S. Bader, “Rare earth replacement magnets,” *Journal of Physics: Condensed Matter*, vol. 26, no. 6, p. 060 301, 2014.
- [26] X. Xiao, F. Müller, G. Bavendiek, N. Leuning, P. Zhang, J. Zou, and K. Hameyer, “Modeling of scalar dependencies of soft magnetic material magnetization for electrical machine finite-element simulation,” *IEEE Transactions on Magnetics*, vol. 56, no. 2, pp. 1–4, 2020. DOI: [10.1109/TMAG.2019.2950527](https://doi.org/10.1109/TMAG.2019.2950527).
- [27] M.-O. Nicolaica, “Vehicle dynamics effect on energy efficiency in hybrid electric vehicles,” in *2015 IEEE 17th International Conference on High Performance Computing and Communications, 2015 IEEE 7th International Symposium on Cyberspace Safety and Security, and 2015 IEEE 12th International Conference on Embedded Software and Systems*, 2015, pp. 1669–1672. DOI: [10.1109/HPCC-CSS-ICSS.2015.30](https://doi.org/10.1109/HPCC-CSS-ICSS.2015.30).
- [28] P. Zhang, C. Du, F. Yan, and J. Kang, “Energy efficiency of a ni-mh battery used in hybrid electric vehicles,” in *2011 International Conference on Electric Information and Control Engineering*, 2011, pp. 4996–4999. DOI: [10.1109/ICEICE.2011.5776892](https://doi.org/10.1109/ICEICE.2011.5776892).
- [29] A. John, K. S. Krishnan, and S. Ashok, “Sensitivity of design parameters on soc and fuel efficiency of hev,” in *2017 International Conference on Computation of Power, Energy Information and Commuincation (ICCPEIC)*, 2017, pp. 579–583. DOI: [10.1109/ICCPEIC.2017.8290430](https://doi.org/10.1109/ICCPEIC.2017.8290430).
- [30] P. Zhang, C. Du, F. Yan, and J. Kang, “Research on energy efficiency of the vehicle’s battery pack,” in *2011 International Conference on Electric Information and Control Engineering*, 2011, pp. 5245–5248. DOI: [10.1109/ICEICE.2011.5777027](https://doi.org/10.1109/ICEICE.2011.5777027).
- [31] Y. Liu, S. L. Ho, W. N. Fu, and X. Zhang, “Design optimization of a novel doubly fed dual-rotor flux-modulated machine for hybrid electric vehicles,” *IEEE Transactions on Magnetics*, vol. 51, no. 3, pp. 1–4, 2015. DOI: [10.1109/TMAG.2014.2361779](https://doi.org/10.1109/TMAG.2014.2361779).
- [32] D. Wei, H. He, and J. Li, “A computationally efficiency optimal design for a permanent magnet synchronous motor in hybrid electric vehicles,” in *2020 IEEE 9th International Power Electronics and Motion Control Conference (IPEMC2020-ECCE Asia)*, 2020, pp. 43–47. DOI: [10.1109/IPEMC-ECCEAsia48364.2020.9367752](https://doi.org/10.1109/IPEMC-ECCEAsia48364.2020.9367752).
- [33] C. Liu, K. T. Chau, W. Li, and C. Yu, “Efficiency optimization of a permanent-magnet hybrid brushless machine using dc field current control,” *IEEE Transactions on Magnetics*, vol. 45, no. 10, pp. 4652–4655, 2009. DOI: [10.1109/TMAG.2009.2021402](https://doi.org/10.1109/TMAG.2009.2021402).
- [34] Z. Shen, M. D. Ainslie, A. M. Campbell, and D. A. Cardwell, “Computation of the field in an axial gap, trapped-flux type superconducting electric machine,” *IEEE Transactions on Applied Superconductivity*, vol. 25, no. 3, pp. 1–5, 2015. DOI: [10.1109/TASC.2014.2366972](https://doi.org/10.1109/TASC.2014.2366972).

- [35] K. Sato, J. S. Shin, T. Koseki, and Y. Aoyama, “Basic experiments for high-torque, low-speed permanent magnet synchronous motor and a technique for reducing cogging torque,” in *The XIX International Conference on Electrical Machines - ICEM 2010*, Sep. 2010, pp. 1–6.
- [36] Z. Chen, D. Zou, M. Xu, Z. Li, and H. An, “Harmonic analysis of magnetic field in fractional-slot ipmsm with segment permanent magnets,” in *2018 21st International Conference on Electrical Machines and Systems (ICEMS)*, 2018, pp. 70–74. DOI: [10.23919/ICEMS.2018.8549242](https://doi.org/10.23919/ICEMS.2018.8549242).
- [37] A. Parsapour, M. Moallem, I. Boldea, and B. Fahimi, “High torque density double stator permanent magnet electric machine,” in *2019 IEEE International Electric Machines Drives Conference (IEMDC)*, 2019, pp. 664–670. DOI: [10.1109/IEMDC.2019.8785192](https://doi.org/10.1109/IEMDC.2019.8785192).
- [38] W. Ullah, F. Khan, E. Sulaiman, and M. Umair, “Torque characteristics of high torque density partitioned pm consequent pole flux switching machines with flux barriers,” *CES Transactions on Electrical Machines and Systems*, vol. 4, no. 2, pp. 130–141, 2020. DOI: [10.30941/CESTEMS.2020.00018](https://doi.org/10.30941/CESTEMS.2020.00018).
- [39] Y. Alamoudi, G. Atkinson, B. Mecrow, and M. Zhang, “A new high torque density permanent magnet machine design for electric vehicles,” in *IECON 2012 - 38th Annual Conference on IEEE Industrial Electronics Society*, 2012, pp. 2348–2353. DOI: [10.1109/IECON.2012.6388705](https://doi.org/10.1109/IECON.2012.6388705).
- [40] C. Li, G. Wang, G. Zhang, and D. Xu, “High frequency torque ripple suppression for high frequency signal injection based sensorless control of synrms,” in *2019 IEEE Applied Power Electronics Conference and Exposition (APEC)*, 2019, pp. 2544–2548. DOI: [10.1109/APEC.2019.8722101](https://doi.org/10.1109/APEC.2019.8722101).
- [41] P. Rafajdus, A. Peniak, D. Peter, P. Makyš, and L. Szabó, “Optimization of switched reluctance motor design procedure for electrical vehicles,” in *2014 International Conference on Optimization of Electrical and Electronic Equipment (OPTIM)*, May 2014, pp. 397–404.
- [42] A. S. Abdel-Khalik, A. M. Massoud, and S. Ahmed, “A senior project-based multi-phase motor drive system development,” *IEEE Transactions on Education*, vol. 59, no. 4, pp. 307–318, Nov. 2016.
- [43] B. S. R. Armstrong, “Multi-level control of hydraulic gerotor motors and pumps,” in *2006 American Control Conference*, Jun. 2006, 8 pp.-.
- [44] M. Z. Ahmad, E. Sulaiman, Z. A. Haron, and T. Kosaka, “Design improvement of a new outer-rotor hybrid excitation flux switching motor for in-wheel drive ev,” in *2013 IEEE 7th International Power Engineering and Optimization Conference (PEOCO)*, Jun. 2013, pp. 298–303.
- [45] Y. Wang, Z. Zhang, R. Liang, W. Yuan, and Y. Yan, “Torque density improvement of doubly salient electromagnetic machine with asymmetric current control,” *IEEE Transactions on Industrial Electronics*, vol. 63, no. 12, pp. 7434–7443, Dec. 2016.

- [46] R. O. C. Lyra and T. A. Lipo, "Torque density improvement in a six-phase induction motor with third harmonic current injection," *IEEE Transactions on Industry Applications*, vol. 38, no. 5, pp. 1351–1360, Sep. 2002.
- [47] J. Lee, "Structural design optimization of electric motors to improve torque performance," Ph.D. dissertation, University of Michigan, 2010.
- [48] A. Judge, "Air gap elimination in permanent magnet machines," Ph.D. dissertation, Worcester Polytechnic Institute, 2012.
- [49] D. Z. Abdelhamid and A. M. Knight, "Performance of a high torque density induction motor with an integrated magnetic gear," in *2016 XXII International Conference on Electrical Machines (ICEM)*, Sep. 2016, pp. 538–544.
- [50] S. Mezani, T. Hamiti, L. Belguerras, T. Lubin, M. Rashed, and C. Gerada, "Magnetically geared induction machines," *IEEE Transactions on Magnetics*, vol. 51, no. 11, pp. 1–4, Nov. 2015, ISSN: 0018-9464.
- [51] D. Z. Abdelhamid and A. M. Knight, "High torque density induction motor with integrated magnetic gear," in *2016 IEEE Energy Conversion Congress and Exposition (ECCE)*, Sep. 2016, pp. 1–7.
- [52] B. Bidouche, T. Lubin, and S. Mezani, "Design and analysis of a magnetically geared induction machine," in *2018 XIII International Conference on Electrical Machines (ICEM)*, Sep. 2018, pp. 629–634.
- [53] S. Peng, W. N. Fu, and S. L. Ho, "A novel high torque-density triple-permanent-magnet-excited magnetic gear," *IEEE Transactions on Magnetics*, vol. 50, no. 11, pp. 1–4, Nov. 2014, ISSN: 0018-9464.
- [54] T.-F. Chan, "Synchronous machines," Ph.D. dissertation, Hong Kong Polytechnic Institute, 2019.
- [55] A. Al-Timimy, P. Giangrande, M. Degano, M. Galea, and C. Gerada, "Comparative study of permanent magnet-synchronous and permanent magnet-flux switching machines for high torque to inertia applications," in *2017 IEEE Workshop on Electrical Machines Design, Control and Diagnosis (WEMDCD)*, Apr. 2017, pp. 45–51.
- [56] F. Kucuk and T. Nakamura, "Torque density and efficiency improvement of a switched reluctance motor via low-cost permanent magnets," in *2018 XIII International Conference on Electrical Machines (ICEM)*, Sep. 2018, pp. 2318–2322.
- [57] C. Peng, S. Song, R. Ma, and W. Liu, "A novel modular 4-level power converter-based direct instantaneous torque control strategy for switched reluctance machine," in *2018 13th IEEE Conference on Industrial Electronics and Applications (ICIEA)*, 2018, pp. 2079–2083. DOI: [10.1109/ICIEA.2018.8398052](https://doi.org/10.1109/ICIEA.2018.8398052).
- [58] W. Peng, J. Gyselinck, J.-W. Ahn, and D.-H. Lee, "Torque sharing function control of switched reluctance machines without phase current sensors," in *2018 21st International Conference on Electrical Machines and Systems (ICEMS)*, 2018, pp. 1940–1945. DOI: [10.23919/ICEMS.2018.8549037](https://doi.org/10.23919/ICEMS.2018.8549037).

- [59] G. Xu, G. Liu, M. Chen, X. Du, and M. Xu, “Cost-effective vernier permanent-magnet machine with high torque performance,” *IEEE Transactions on Magnetics*, vol. 53, no. 11, pp. 1–4, Nov. 2017.
- [60] S. Nakano, K. Kiyota, and A. Chiba, “Design consideration of high torque-density switched reluctance motor for hybrid electrical vehicle,” in *2016 19th International Conference on Electrical Machines and Systems (ICEMS)*, Nov. 2016.
- [61] J. Shi, F. Chai, X. Li, and S. Cheng, “Study of the number of slots/pole combinations for low speed high torque permanent magnet synchronous motors,” in *2011 International Conference on Electrical Machines and Systems*, Aug. 2011, pp. 1–3.
- [62] S. Umans, A. Fitzgerald, and C. Kingsley, *Electric Machinery: Seventh Edition*. McGrawHill Higher Education, 2013, ISBN: 9780077428501.
- [63] B. Singh and S. Singh, “State-of-art on permanent magnet brushless dc motor drives,” *Journal of power electronics*, vol. 9, pp. 1–17, Jan. 2009.
- [64] P. C. Krause, O. Wasynczuk, and S. D. Sudhoff, *Analysis of Electric Machinery and Drive Systems*. John Wiley and Sons, 2013.
- [65] Y. Zhang, J. X. Shen, and P. Li, “Optimal design of an interior permanent magnet synchronous motor for electrical vehicle applications,” in *2013 International Conference on Electrical Machines and Systems (ICEMS)*, Oct. 2013, pp. 982–985.
- [66] Y. Liu, W. N. Fu, X. Guo, Z. Li, and R. Fang, “A dual permanent magnet machine for high-torque low-speed applications,” in *2017 20th International Conference on Electrical Machines and Systems (ICEMS)*, Aug. 2017, pp. 1–4.
- [67] J. Liang, A. Parsapour, E. Cosoroaba, M. Wu, I. Boldea, and B. Fahimi, “A high torque density outer rotor claw pole stator permanent magnet synchronous motor,” in *2018 IEEE Transportation Electrification Conference and Expo (ITEC)*, Jun. 2018, pp. 389–393.
- [68] X. Zhu, L. Chen, L. Quan, Y. Sun, W. Hua, and Z. Wang, “A new magnetic-planetary-g geared permanent magnet brushless machine for hybrid electric vehicle,” *IEEE Transactions on Magnetics*, vol. 48, no. 11, pp. 4642–4645, 2012. DOI: [10.1109/TMAG.2012.2202276](https://doi.org/10.1109/TMAG.2012.2202276).
- [69] L. Lavrinovicha and J. Dirba, “Comparison of permanent magnet synchronous motor and synchronous reluctance motor based on their torque per unit volume,” in *2014 Electric Power Quality and Supply Reliability Conference (PQ)*, Jun. 2014, pp. 233–236.
- [70] M. Cheng, W. Hua, J. Zhang, and W. Zhao, “Overview of stator-permanent magnet brushless machines,” *IEEE Transactions on Industrial Electronics*, vol. 58, no. 11, pp. 5087–5101, Nov. 2011, ISSN: 0278-0046.
- [71] W. Hua, M. Cheng, Z. Q. Zhu, and D. Howe, “Analysis and optimization of back emf waveform of a flux-switching permanent magnet motor,” *IEEE Transactions on Energy Conversion*, vol. 23, no. 3, pp. 727–733, Sep. 2008, ISSN: 0885-8969.

- [72] W. Hua, G. Zhang, and M. Cheng, "Investigation and design of a high-power flux-switching permanent magnet machine for hybrid electric vehicles," *IEEE Transactions on Magnetics*, vol. 51, no. 3, pp. 1–5, Mar. 2015.
- [73] Y. Yao and C. Liu, "A efficient nine-phase pm flux-switching machine with high torque density and low torque ripple," in *2018 Asia-Pacific Magnetic Recording Conference (APMRC)*, Nov. 2018, pp. 1–2.
- [74] Z. Xiang, L. Quan, and X. Zhu, "A new partitioned-rotor flux-switching permanent magnet motor with high torque density and improved magnet utilization," *IEEE Transactions on Applied Superconductivity*, vol. 26, no. 4, pp. 1–5, Jun. 2016.
- [75] C. C. Awah, Z. Q. Zhu, Z. Wu, and D. Wu, "High torque density magnetically-gear switched flux permanent magnet machines," in *2015 Tenth International Conference on Ecological Vehicles and Renewable Energies (EVER)*, Mar. 2015, pp. 1–6.
- [76] B. Kim and T. A. Lipo, "Operation and design principles of a pm vernier motor," *IEEE Transactions on Industry Applications*, vol. 50, no. 6, pp. 3656–3663, Nov. 2014, ISSN: 0093-9994.
- [77] D. Li, R. Qu, J. Li, L. Xiao, L. Wu, and W. Xu, "Analysis of torque capability and quality in vernier permanent-magnet machines," *IEEE Transactions on Industry Applications*, vol. 52, no. 1, pp. 125–135, Jan. 2016, ISSN: 0093-9994.
- [78] B. Kim and T. A. Lipo, "Analysis of a pm vernier motor with spoke structure," *IEEE Transactions on Industry Applications*, vol. 52, no. 1, pp. 217–225, Jan. 2016, ISSN: 0093-9994.
- [79] D. Li, R. Qu, and T. A. Lipo, "High-power-factor vernier permanent-magnet machines," *IEEE Transactions on Industry Applications*, vol. 50, no. 6, pp. 3664–3674, Nov. 2014, ISSN: 0093-9994.
- [80] T. Zou, D. Li, R. Qu, D. Jiang, and J. Li, "Advanced high torque density pm vernier machine with multiple working harmonics," *IEEE Transactions on Industry Applications*, vol. 53, no. 6, pp. 5295–5304, Nov. 2017.
- [81] M. Franke, M. Brutscheck, and U. Schmucker, "Modeling and simulation of a rolling rotor switched reluctance motor," *2009 32nd International Spring Seminar on Electronics Technology*, pp. 1–6, 2009.
- [82] M. Alibeik, O. N. M. Nezamuddin, R. M. Bagwe, M. J. Rubin, and E. Cipriano dos Santos, "Airgapless electric motors with an external rotor," *IEEE Transactions on Industrial Electronics*, vol. 65, no. 9, pp. 6923–6935, Sep. 2018, ISSN: 0278-0046.
- [83] O. Nezamuddin, M. Alibeik, R. Bagwe, M. Rubin, and E. dos Santos, "Internal rotor airgap-less electric motors," in *2017 IEEE Energy Conversion Congress and Exposition (ECCE)*, Oct. 2017, pp. 5009–5016.
- [84] R. Akune, K. Akatsu, M. Fujihara, and T. Yamamoto, "Study of high torque density interior permanent magnet synchronous motor with flexible orientation nd2fe14b sintered magnet," in *2016 XXII International Conference on Electrical Machines (ICEM)*, Sep. 2016, pp. 578–584.

- [85] N. W. Wheeler, “Mechanical and geometric considerations for the airgapless motor,” Ph.D. dissertation, 2018.
- [86] A. S. Abdel-Khalik, A. M. Massoud, and S. Ahmed, “A senior project-based multi-phase motor drive system development,” *IEEE Transactions on Education*, vol. 59, no. 4, pp. 307–318, Nov. 2016, ISSN: 0018-9359.
- [87] Armstrong, “Multi-level control of hydraulic gerotor motors and pumps,” vol. 2006, Jul. 2006, 8 pp.
- [88] C.-S. Kim and C.-O. Lee, “Speed control of an overcentered variable-displacement hydraulic motor with a load-torque observer,” *Control Engineering Practice*, vol. 4, no. 11, pp. 1563–1570, 1996.
- [89] Y. Yang, L. Ma, and D. Huang, “Development and repetitive learning control of lower limb exoskeleton driven by electrohydraulic actuators,” *IEEE Transactions on Industrial Electronics*, vol. 64, no. 5, pp. 4169–4178, 2017. DOI: [10.1109/TIE.2016.2622665](https://doi.org/10.1109/TIE.2016.2622665).
- [90] S. S. R. Bonthu, S. Choi, A. Gorgani, and K. Jang, “Design of permanent magnet assisted synchronous reluctance motor with external rotor architecture,” in *2015 IEEE International Electric Machines Drives Conference (IEMDC)*, May 2015, pp. 220–226.
- [91] P. J. Holik, D. G. Dorrell, and M. Popescu, “Performance improvement of an external-rotor split-phase induction motor for low-cost drive applications using external rotor can,” *IEEE Transactions on Magnetics*, vol. 43, no. 6, pp. 2549–2551, Jun. 2007, ISSN: 0018-9464.
- [92] J. Lin, N. Schofield, and A. Emadi, “External-rotor 6 – 10 switched reluctance motor for an electric bicycle,” *IEEE Transactions on Transportation Electrification*, vol. 1, no. 4, pp. 348–356, Dec. 2015.
- [93] S. M. Castano, B. Bilgin, J. Lin, and A. Emadi, “Radial forces and vibration analysis in an external-rotor switched reluctance machine,” *IET Electric Power Applications*, vol. 11, no. 2, pp. 252–259, 2017, ISSN: 1751-8660.
- [94] H. Yang, H. Lin, Z. Q. Zhu, K. Guo, D. Wang, S. Fang, and Y. Huang, “Flux-concentrated external-rotor switched flux memory machines for direct-drive applications,” *IEEE Transactions on Applied Superconductivity*, vol. 26, no. 7, pp. 1–6, Oct. 2016, ISSN: 1051-8223.
- [95] R. Wrobel, P. H. Mellor, N. McNeill, and D. A. Staton, “Thermal performance of an open-slot modular-wound machine with external rotor,” *IEEE Transactions on Energy Conversion*, vol. 25, no. 2, pp. 403–411, Jun. 2010, ISSN: 0885-8969.
- [96] V. B. Honsinger, “Sizing equations for electrical machinery,” *IEEE Transactions on Energy Conversion*, vol. EC-2, no. 1, pp. 116–121, Mar. 1987, ISSN: 0885-8969.
- [97] W. Chu, Z. Zhu, and Y. Shen, “Analytical optimisation of external rotor permanent magnet machines,” *IET Electrical Systems in Transportation*, vol. 3, no. 2, pp. 41–49, Jun. 2013, ISSN: 2042-9738.

- [98] Y. Yang, L. Ma, and D. Huang, “Development and repetitive learning control of lower limb exoskeleton driven by electrohydraulic actuators,” *IEEE Transactions on Industrial Electronics*, vol. 64, no. 5, pp. 4169–4178, May 2017, ISSN: 0278-0046.
- [99] S. Shaffer, *Tribology 101: Introduction to the basics of tribology*, Webinar, 2013.
- [100] D. Lauer, *Tribology: The key to proper lubricant selection*, Noria.
- [101] B. J. Hamrock, *Fundamentals of Fluid Film Lubrication*. Marcel Dekker, INC, 1994.
- [102] M. M. Khonsari, *Applied Tribology: Bearing Design and Lubrication*, 3rd ed. Wiley, 2017.
- [103] S.-M. KWON, M. S. KIM, and J.-H. SHIN, “Analytical wear model of a gerotor pump without hydrodynamic effect,” *Journal of Advanced Mechanical Design, Systems, and Manufacturing*, vol. 2, no. 2, pp. 230–237, 2008.
- [104] K. I. Laskaris and A. G. Kladas, “Internal permanent magnet motor design for electric vehicle drive,” *IEEE Transactions on Industrial Electronics*, vol. 57, no. 1, pp. 138–145, Jan. 2010, ISSN: 0278-0046.
- [105] J. M. Crider and S. D. Sudhoff, “An inner rotor flux-modulated permanent magnet synchronous machine for low-speed high-torque applications,” *IEEE Transactions on Energy Conversion*, vol. 30, no. 3, pp. 1247–1254, Sep. 2015, ISSN: 0885-8969.
- [106] M. Alibeik, O. Nezamuddin, R. Bagwe, M. Rubin, and E. C. D. Santos, “Airgap-less electric motors with external rotor,” *IEEE Transactions on Industrial Electronics*, vol. PP, no. 99, pp. 1–1, 2018.
- [107] M. Alibeik, O. Nezamuddin, M. Rubin, N. Wheeler, S. Silvestri, and E. dos Santos, “Airgap-less electric motor: A solution for high-torque low-speed applications,” in *2017 IEEE International Electric Machines and Drives Conference (IEMDC)*, May 2017, pp. 1–8.
- [108] X. Ji and J. Zhou, “Solving high-order uncertain differential equations via runge-kutta method,” *IEEE Transactions on Fuzzy Systems*, vol. PP, no. 99, pp. 1–1, 2017.

VITA

Maryam Alibeik received the B.S. degree in Fall of 2011, the M.S. degree in Spring of 2014, both in Electrical and Computer Engineering from Purdue School of Engineering and Technology in Indianapolis. She started the PhD Program in Electrical and Computer Engineering in the Fall of 2014 in Purdue School of Engineering and Technology in Indianapolis. Her main focus during the PhD program was on power electronics and electric machines. Maryam has been working in the power electronics/Electric Machinery lab since July 2012 and has done an extensive research on different configurations of power converters, microgrids, and airgap-less electric machines. In addition, Maryam was involved in the development of the airgap-less electric motor along with its drive system. She was also involved in a project for commercializing a solar micro-inverter that was funded through NSF I-CORPS program. Maryam's research interests include but are not limited to power electronics, electric machinery, controls, and etc. Maryam is also an active member of IEEE society as well as Society of Women in Engineering.